NASA CONTRACTOR REPORT

NASA CR-2253

NASA CR-2253

MASS SPECTROMETRY AND INHOMOGENEOUS ION OPTICS

by Frederick A. White

Prepared by
RENSSELAER POLYTECHNIC INSTITUTE
Troy, N.Y. 12180
for Langley Research Center

NATIONAL AERONAUTICS AND SPACE ADMINISTRATION • WASHINGTON, D. C. • NOVEMBER 1973

1. Report No.
NASA CR-2253

2. Government Accession No.

3. Recipient's Catalog No.

4. Title and Subtitle
MASS SPECTROMETRY AND INHOMOGENEOUS ION OPTICS

5. Report Date
November 1973

6. Performing Organization Code

7. Author(s)
Frederick A. White

8. Performing Organization Report No.

9. Performing Organization Name and Address
Rensselaer Polytechnic Institute
Troy, New York 12180

10. Work Unit No.
970-32-20-09

11. Contract or Grant No.
NGL 33-018-053

12. Sponsoring Agency Name and Address
National Aeronautics and Space Administration
Washington, D.C. 20546

13. Type of Report and Period Covered
Contractor Report

14. Sponsoring Agency Code

15. Supplementary Notes
This is a final report.

16. Abstract

This report describes work done in several areas to advance the state of the art of magnetic mass spectrometers. The calculations and data necessary for the design of inhomogeneous field mass spectrometers, and the calculation of ion trajectories through such fields are presented. The development and testing of solid state ion detection devices providing the capability of counting single ions is discussed. New techniques in the preparation and operation of thermal-ionization ion sources are described. Data obtained on the concentrations of copper in rainfall and uranium in air samples using the improved thermal ionization techniques are presented. The design of a closed system static mass spectrometer for isotopic analyses is discussed. A summary of instrumental aspects of a four-stage mass spectrometer comprising two electrostatic and two 90° magnetic lenses with a 122-cm radius used to study the interaction of ions with solids is presented.

17. Key Words (Suggested by Author(s))
Mass spectrometry
Ion trajectories
Ion sources and detectors
Metallic pollution measurements

18. Distribution Statement
Unclassified - Unlimited

19. Security Classif. (of this report)
Unclassified

20. Security Classif. (of this page)
Unclassified

21. No. of Pages
131

22. Price*
Domestic, \$4.50
Foreign, \$7.00

*For sale by the National Technical Information Service, Springfield, Virginia 22151

CONTENTS

LIST OF ILLUSTRATIONS

I. ION OPTICS

A major effort has been undertaken in ion optics, with specific emphasis on theoretical calculations and the construction of an inhomogeneous field instrument. A 255° magnet of large dimensions was conceived in order to provide a laboratory instrument of great versatility.

As a mass spectrometer, this analyzer which is being developed should have the maximum sensitivity of any single stage analyzer. The applications of a single stage, high-transmission, double focusing, large radius analyzing system are virtually limitless.[1,2,3] Lunar, meteoric and geological samples as well as medical tracer specimens could also be analyzed for isotopic content or low level alpha activity, (see Table A). Analyses, similar to the one reported by Mewherter et al.,(4) could also be made for plutonium or any other man-made isotope which may occur in the environment. Because of the high transmission characteristic, the thermal ionization efficiencies of various source materials can be measured in addition to providing experimental data for determining work functions. Both negative and positive ionization efficiencies could be measured by reversing the analyzing magnetic field. In the study of crystal structure, surface phenomena, and ion transmission properties, the

ALPHA PARTICLE ACTIVITIES OF THE TRANSURANIC ELEMENTS

Isotope	Half-Life	Alpha Energy	% of Total Alpha Emission	DPM/μg*	Disintegrations* per μg per wk.
U-238	4.5×10^9y	4.195	77	5.7×10^{-1}	5.75×10^3
Pu-239	2.43×10^4y	5.147	72.5	9.9×10^4	10^9
Cm-244	17.6y	5.806	76.7	1.42×10^8	1.44×10^{12}
Cm-245	9.3×10^3y	5.362	80	2.83×10^5	2.86×10^9
Cm-246	5.5×10^3y	5.386	81	4.78×10^5	4.83×10^9
Cm-247	1.6×10^7y	~5.3	~100	2.01×10^2	2.03×10^6
Cm-248	4.7×10^5y	5.080	82	5.52×10^3	5.58×10^7
Bk-247	1.7×10^3y	5.52	58	1.33×10^6	1.34×10^{10}
Bk-249	314d	5.412	69	2.55×10^9	2.58×10^{13}
Cf-248	350d	6.27	100	3.34×10^9	3.38×10^{13}
Cf-249	360y	5.812	84	7.45×10^6	7.53×10^{10}
Cf-252	2.55y	6.119	84.3	9.65×10^8	9.75×10^{12}
Es-254	480d	6.437	93	2.22×10^9	2.24×10^{13}
Fm-254	3.24h	7.200	85	7.46×10^{12}	7.54×10^{16}

*= Specific activities times % of emission of the stated alpha line

Table A

magnet could provide a basic analyzing system. The large radius will allow a particle energy range of 10 percent while a 4 inch gap width permits installation of crystalline target material within the magnetic field. High energy α-particle backscattering experiments or improved ion-transmission systems such as the one described by Rasekhi[5] can be conducted with this device. Field emission ion sources or even an electric lens for improved resolution may be installed within the magnetic field. Since this device can accommodate high energy ions, sputtering sources with high potential acceleration anodes may be utilized. The large energy spread of such ions greatly affects the resolving power of an anlyzer. However, by accelerating the sputtered ions before analysis, their relative energy dispersion is reduced. Low intensity processes such as photo-ionization would be well suited for investigation by this high-transmission system. Or conversely the analyzer could provide an intense ion beam of various energies for the study of ion to photon conversion properties. The large radial and axial extent of the magnetic field may make it possible to develop a point to point ion-imaging system in order to investigate spatial surface emission characteristics of a sample.

The energy of α-particles, like any other charged-particle radiation, can be measured by the number of ion pairs created by it upon passing through a medium.[6] Some individual particle detectors are: ionization and cloud chambers, proportional, spark, and scintillation counters, nuclear emulsions, and semiconductor devices. Only the last three are easily adapted to charged-particle spectrometry. Nuclear emulsions developed for high energy experiments and spectrographic detectors are highly efficient and extremely sensitive. Such plates are useful for recording rare events due to their insensitivity to background. However, it is impossible to separate events in time and the resultant energy resolution is low ~5%. Scintillation counters are simple, reliable, and have fast response times as well as a large working area and insensitivity to intense beta and gamma background radiation. Again, these devices exhibit a low energy resolution ~5%. Surface barrier detectors are perhaps the most versatile radiation detectors commonly used. Nevertheless, their energy resolution and background level are inferior to magnetic spectrographs. Combining a high-transmission magnetic analyzer with a solid-state detection system would quite probably result in an optimum analyzing system, superior to either device operating independently. Range and ionization fluctuations inherent in the detector would be minimal. Such a system would be well suited to detect low level alpha-radiation emitted in the presence of competing strong reactions which produce high background radiation.

Luminosity and resolution are the primary requisites for selecting a magnetic optical system for the charged-particle investigations described previously. High luminosity is characterized by a large acceptance angle and the 255° ($\sqrt{2}\pi$) system has a greater acceptance angle (~0.3% of 4π steradians) than an equivalent 180° device. One characteristic of 180° inhomogeneous magnets is that their ion source and focal point are in the fringing fields of the system. With a 255° device, it is possible to locate both the source and detector within the main field of the magnet (Fig. 1). Several 180° instruments have been constructed for investigating α-particle radiation, but at present there are no 255° devices under construction in this country for use in the research activities previously mentioned.

Dzhelepov et al.,[7] have constructed a 255° device promarily for the investigation of α-particles. The estimated resolution is ~0.10% with a transmission factor approximately 0.3% of 4π steradians. This effective solid angle is at least an order of magnitude greater than other types of spectrometers. Photographic emulsions are used in the detection system even though solid state detectors would allow direct, real-

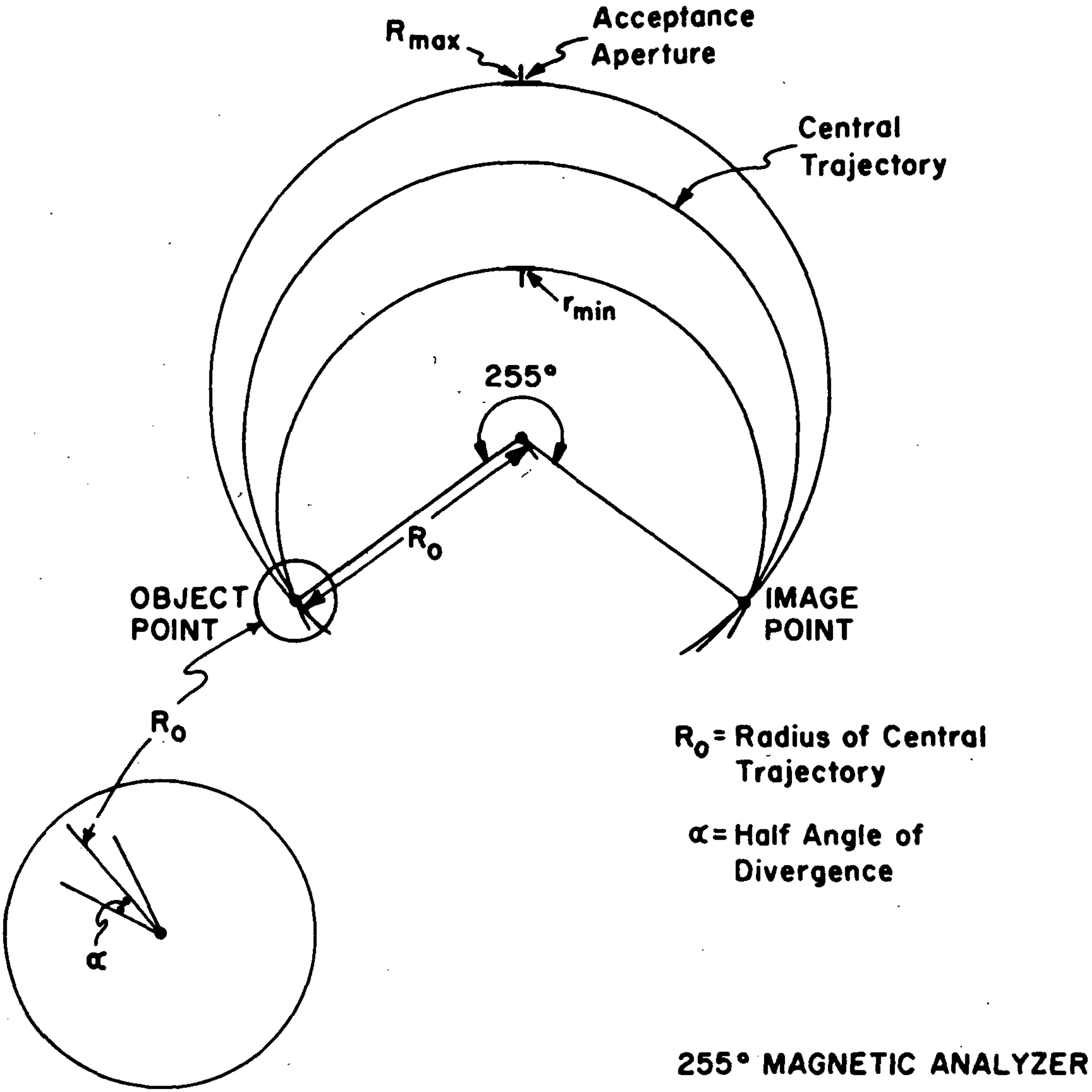
R max
Acceptance Aperture
Central Trajectory
r min
255°
R o
OBJECT POINT
IMAGE POINT
R o
α
R o = Radius of Central Trajectory
α = Half Angle of Divergence
255° MAGNETIC ANALYZER

Figure 1

time readout capability. Shaping of the pole pieces was accomplished by field expansion techniques and experimentally determined mechanical shims. Experiments conducted with this device indicate that it operates within the theoretically predicted resolution and transmission parameters.

Several 180° inhomogeneous field spectrometers such as those by Holtebekk[8] and by Judd[9] have been constructed for charged-particle investigations. Acceptance solid angles are quoted at about $1.2 \cdot 10^{-3}$ of 4π steradians with a resolving power of approximately 1000. Field expansion techniques were utilized in the magnetic field design and 3rd order coefficients were calculated in order to reduce aberrations. Preliminary measurements on the Judd instrument at Berkeley indicate a resolution of 0.1% with a solid angle of about $7 \cdot 10^{-4}$ of 4π steradians.

Specifications of Analyzing Magnet

The RPI Analyzing magnet has been constructed to the following parameters:

1.0 Mean radius of 27.8 inches

2.0 Maximum extent of pole pieces is 270°

3.0 Total beam deflection angle is 255° ($\sqrt{2}\pi$)

4.0 Field Index of inhomogeneity is 0.5

5.0 Gap width is 4.0 inches at the mean radius

6.0 Pole pieces extend from 16 to 44 inches

7.0 Maximum induction in the gap is 5500 gauss at a radius of 27.8 inches

8.0 Maximum magnetic induction in the pole pieces is 11,200 gauss

9.0 Object and image points are at the mean radius within the field

10.0 Design beam acceptance angle is $\pm 15^{\circ}$ in the horizontal plane and $\pm 2^{\circ}$ in the vertical plane

11.0 Total acceptance of 0.3% of 4π steradians

12.0 Resolving power of approximately 1000, with maximum beam acceptance

13.0 Magnet weight is 70 tons.

Excitation is provided by four exciting coils conforming to the following properties:

1.0 Two copper conductors 0.530" x 0.100" in parallel

2.0 Pyre ML film insulation on all conductors

3.0 Coils constructed on 88 inch diameter aluminum flanges

4.0 Water cooling around the edge of the coil with a total flow of 1.73 gal./min. through 0.25 inch tubes resulting in a 20 degree Fahrenheit temperature rise

5.0 Coil resistance (two wires in parallel) is 2.53 ohms

6.0 Weight of copper is 1900 lbs.; weight of aluminum flange is 138 lbs.

7.0 Coil current is 23.7 amperes at 60 volts.

8.0 Magnetic excitation is 13,050 ampere turns/coil

9.0 Power dissipation for each coil is 1,422 watts

Construction of the iron yoke is complete and is pictured in Fig. 2. The assembly consists of three legs and six yoke pieces as depicted. The coil assemblies are shown in Figure 3 and a constructed working model in Fig. 4. Figure 5 is a photograph of a pole piece in the final machining stage. Power, vacuum, and instrumentation is as yet incomplete.

Theoretical Considerations of Sector Magnetic Fields

The RPI analyzing magnet is a 255° device exhibiting azimuthal symmetry about the z axis and mirror symmetry across the magnetic midplane. Figure 6 depicts the general pole piece shape, utilizing an inhomogeneous field concept. The magnetic field $\vec{B}$ is a decreasing function of the path radius r. The forces exerted on a particle traversing this field with velocity v are indicated in the lower quadrant. The radial and axial forces tend to restore the particle to its initial values of r and z. This property is characteristic of inhomogeneous field systems and double focusing (radial as well as axial) is possible. The 255° analyzing lens has this property

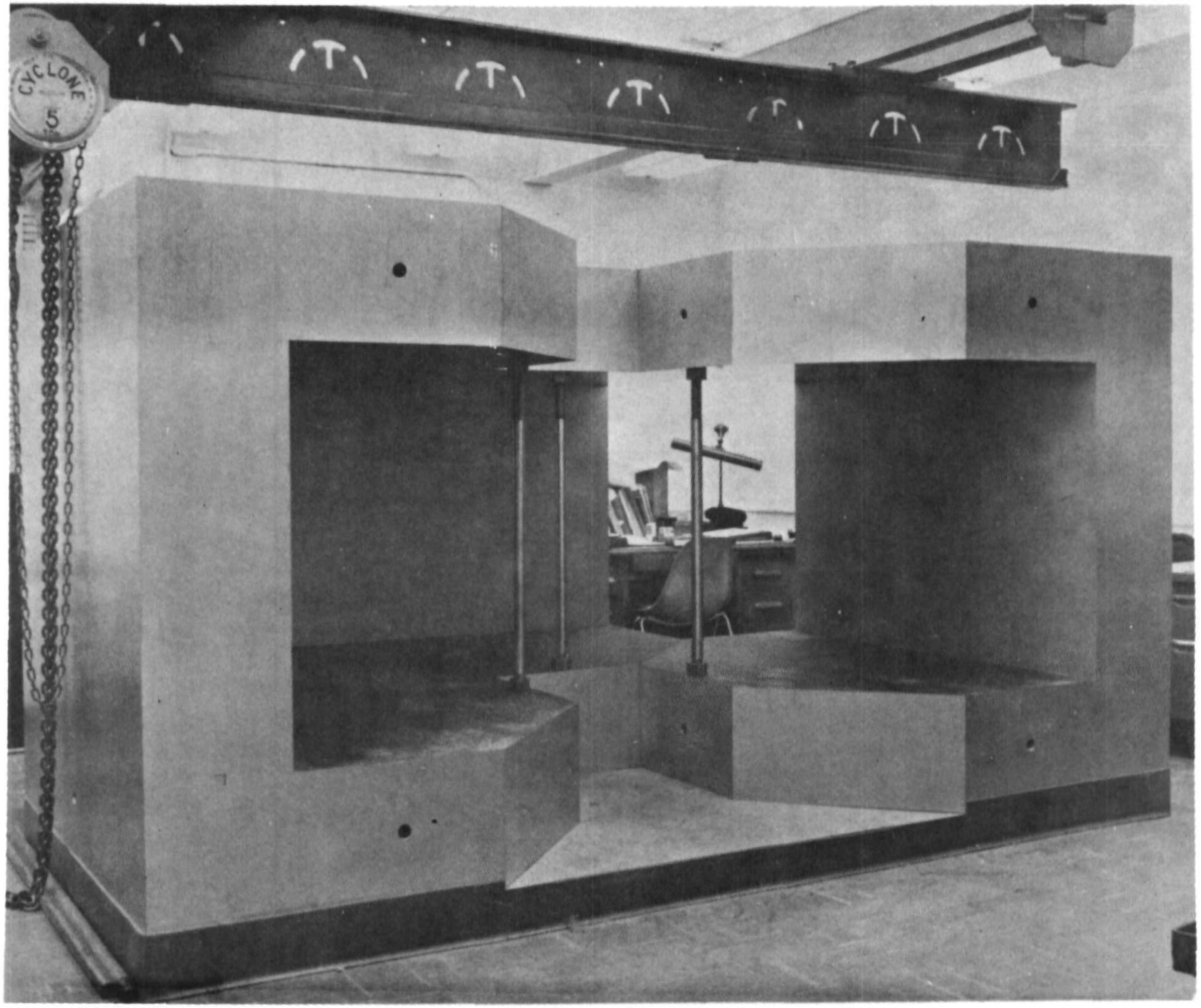

255° Inhomogeneous Analyzer Yoke

Figure 2

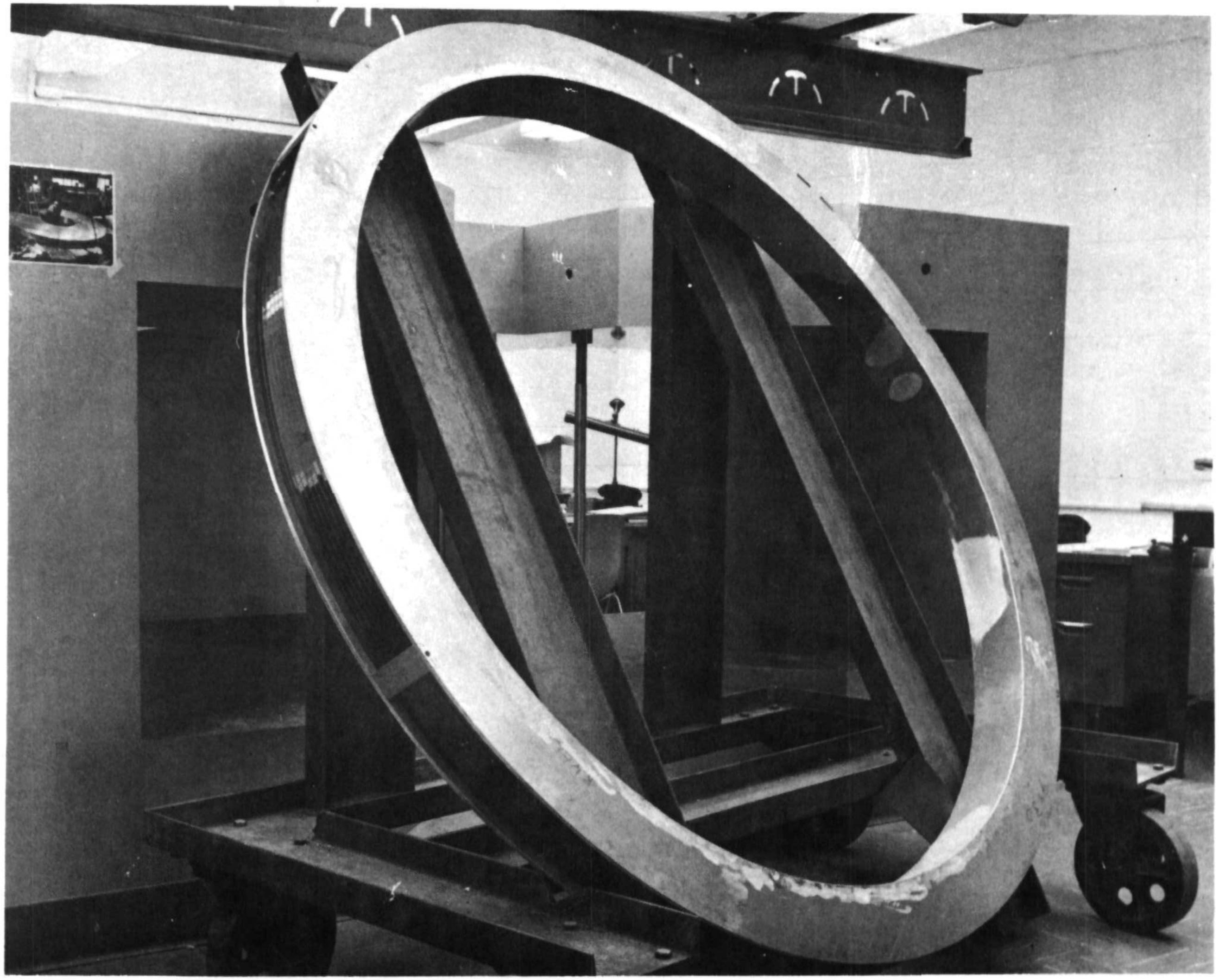

Exciting Coil

Figure 3

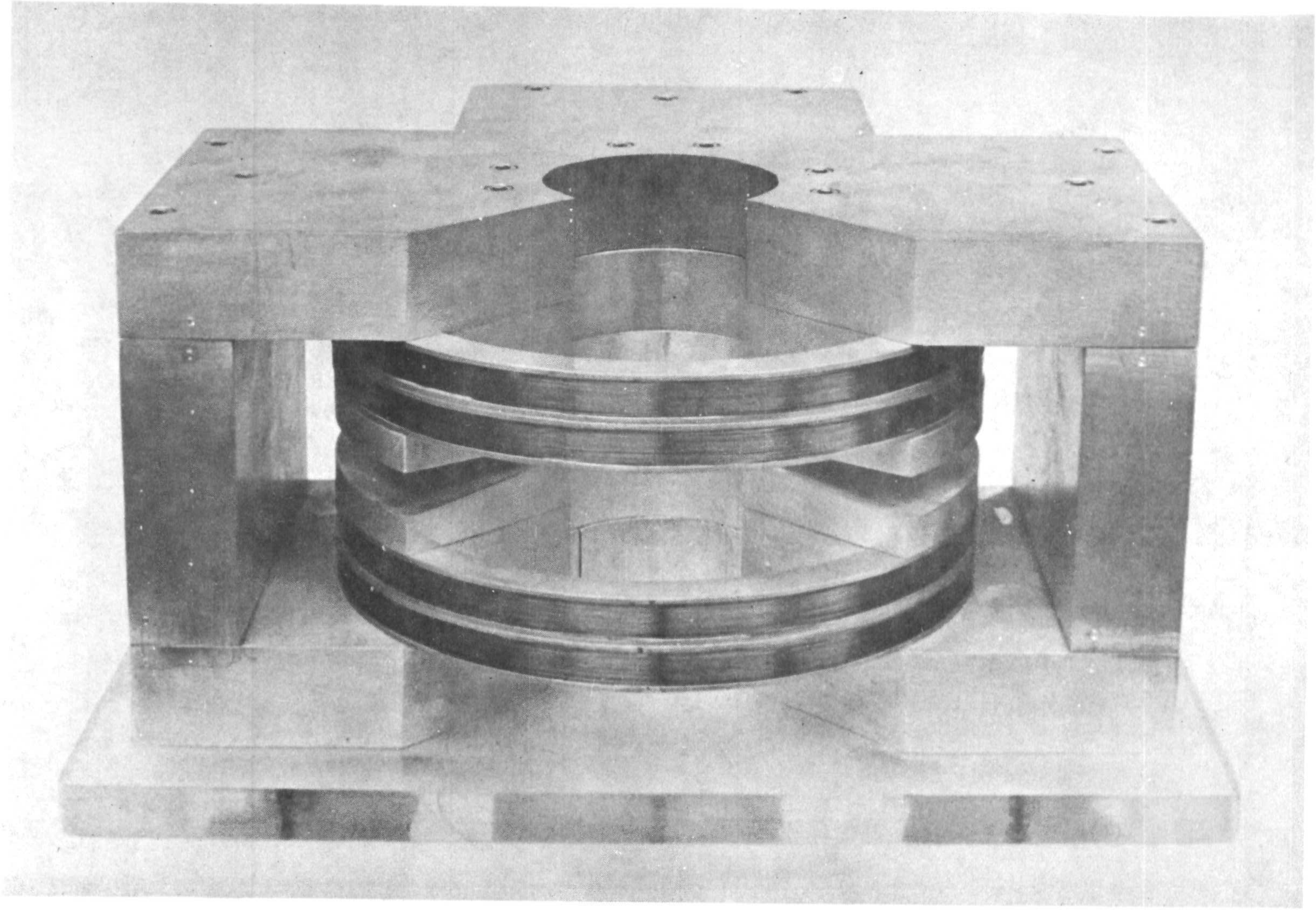

Figure 4 Model of 255° Inhomogeneous Magnetic Alpha Particle and Mass Spectrometer Assembly

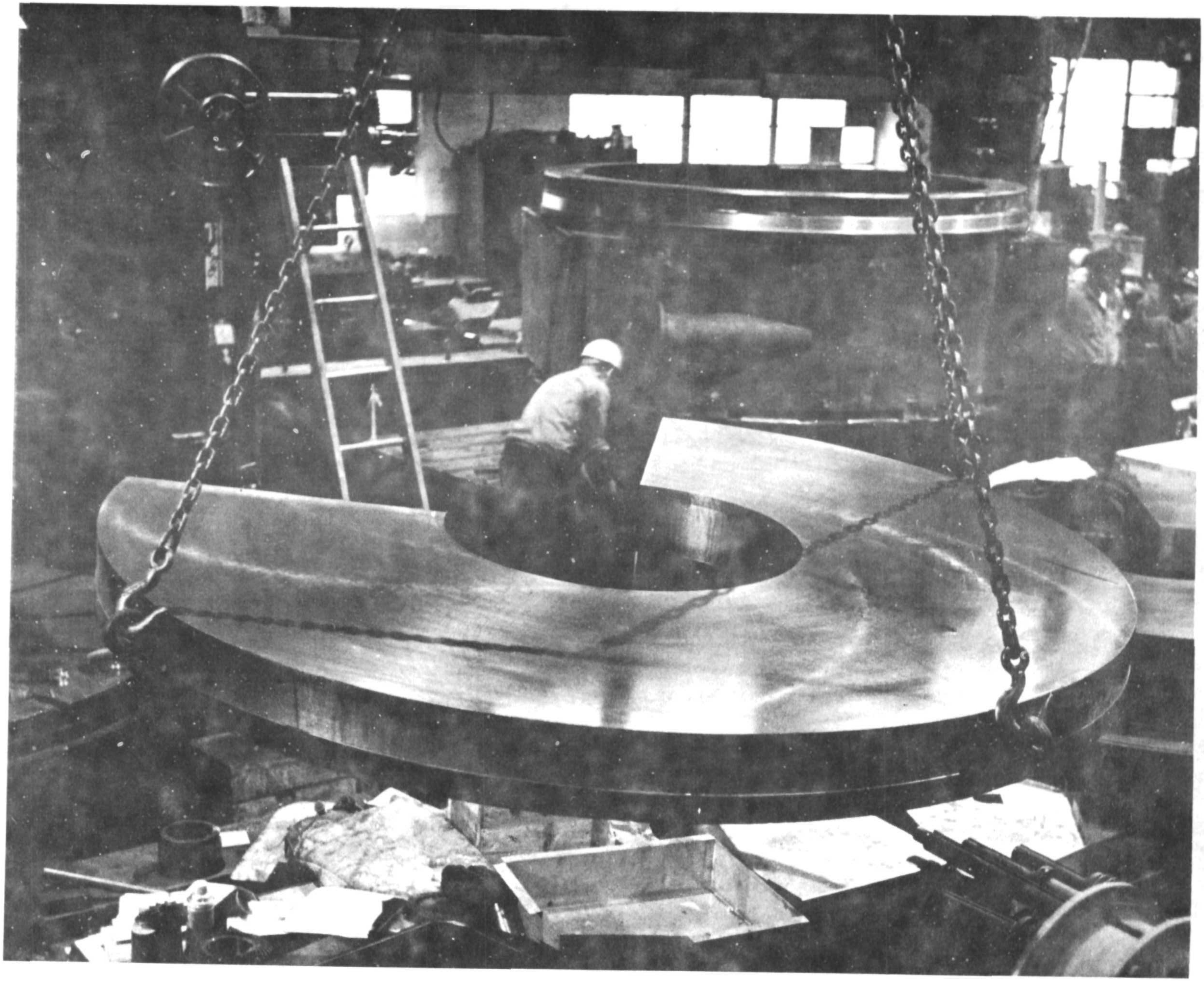

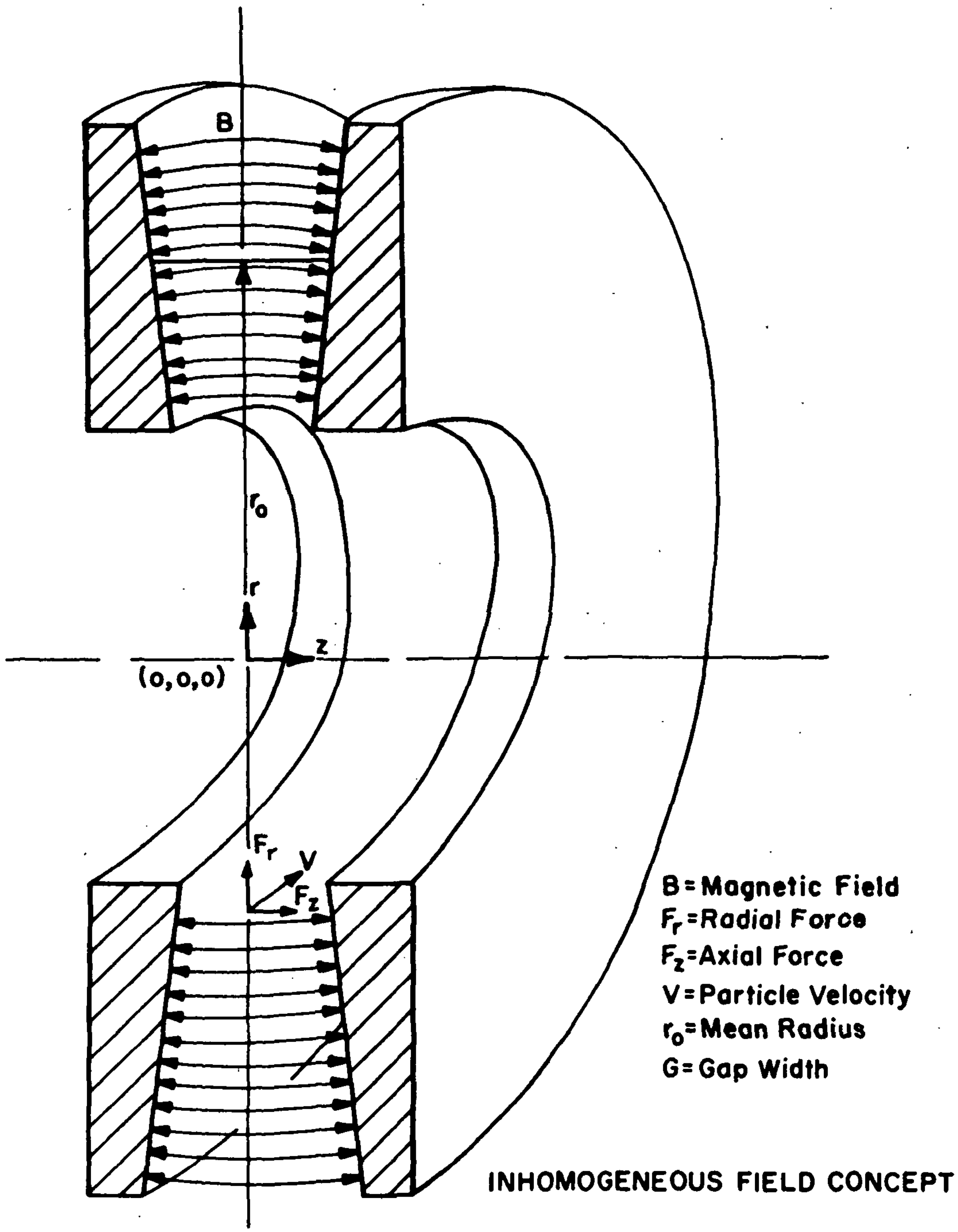
B
r_o
r
z
(o,o,o)
F_r
V
F_z
B=Magnetic Field
F_r=Radial Force
F_z=Axial Force
V=Particle Velocity
r_o=Mean Radius
G=Gap Width
INHOMOGENEOUS FIELD CONCEPT

Figure 6

and with reduced transmission, there is a point to point object-image correspondence. Figure 7 depicts the axial focusing properties of a 255° analyzer, while Fig. 1 indicates the radial properties. The focal properties of this system are completely determined by the midplane induction field expansion, which is a Neumann boundary condition. Unfortunately, it is not possible to choose these coefficients such that the optimum radial and axial focusing properties are achieved simultaneously.[10] Since the most important characteristic of an ion analyzer is resolution as opposed to minimum focal area, this system will be designed to minimize radial image divergence.

In a cylindrical coordinate system, the magnetic field at the analyzer midplane can be represented by the function:

$$[B_z]_{z=0} = B_o\left(\frac{r_o}{r}\right)^n$$

where

B_o = the magnetic induction at $r = r_o$, $z = 0$
r_o = the mean radius
n = the inhomogeneous field index

In general, the field index will have a value between 0.0 and 1.0 for optimum radial focusing. The magnetic field, $\vec{B}$, can be derived either from a vector field $\vec{A}$ or a Scalar magnetic potential Vm. For the development and solution of the general equations of motion, the

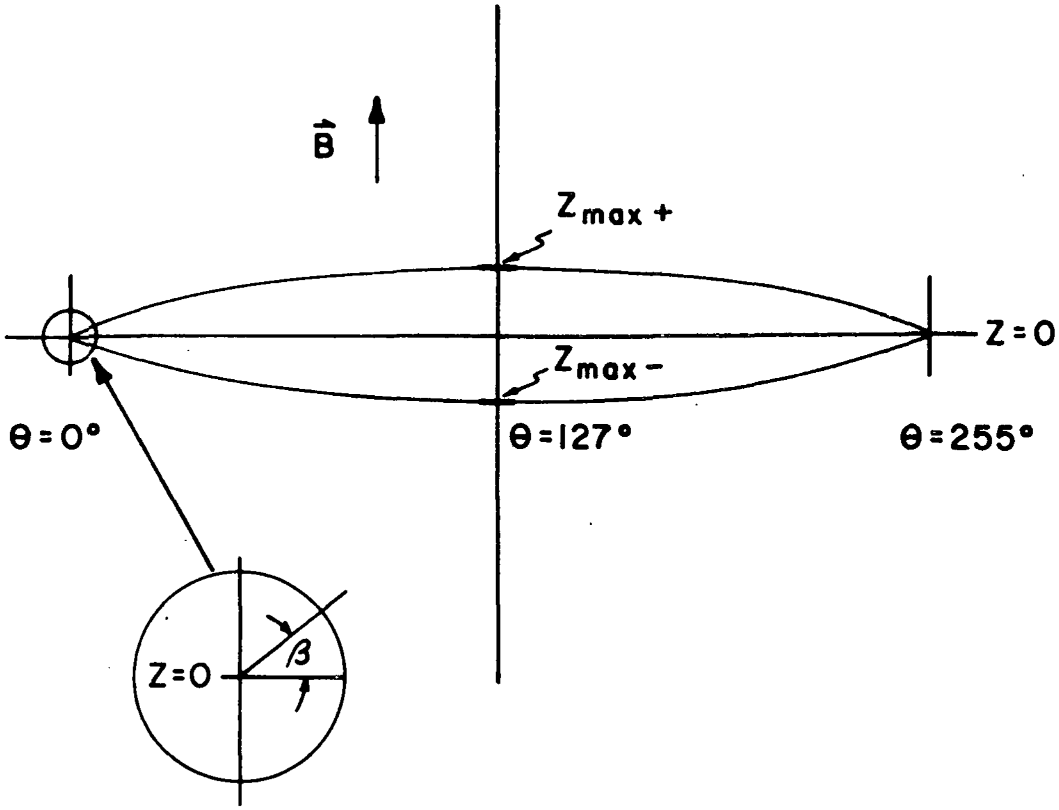

255° AXIAL FOCUSING

Figure 7

vector potential $\vec{A}$ is appropriate, however, the scalar potential Vm is necessary for determining isomagnetic potential contours. Both approaches are straight forward and only algebraic relationships between field expansion coefficients are required to transfer from the vector field derivation of $\vec{B}$ to the magnetic potential description of $\vec{B}$.

Derivation of the Midplane Magnetic Field from a Vector Potential and a Potential Function

The magnetic field induction across the midplane can be expanded in a Taylor series about r_o as follows:

$$[B_z]_{z=0} = B_o[1+b_1\rho+b_2\rho^2+b_3\rho^3+b_4\rho^4+b_5\rho^5+ \ldots]$$

where

$$\rho = \frac{r-r_o}{r_o}$$

b_1, b_2..... = the field shaping constants.

The first shaping constant is related to the basic field inhomogenity value by

$$b_1 = -n.$$

b_2, b_3, b_4 ..... are higher order aberration parameters which are varied to obtain the desired focal properties. These five coefficients uniquely determine the magnetic field in three dimensions, through fifth order.

$\vec{B}$ may be derived from a vector potential by

$$\vec{B} = \nabla \times \vec{A} .$$

For a cylindrical coordinate system,

$$B_z = \frac{1}{r_o}\frac{\partial A\theta}{\partial\rho} + \frac{1}{r_o}\frac{A\theta}{(1+\rho)}$$

and since the magnetic field is azimuthally invariant,

$$A_\theta = B_o r_o(\rho + a_2\rho^2 + a_3\rho^3 + a_4\rho^4 + a_5\rho^5 + a_6\rho^6 \ldots)$$

we have

$$\begin{aligned}[B_z]_{z=0} = B_o[&1+(1+2a_2)\rho + (-1+a_2+3a_3)\rho^2 \\ &+ (1-a_2+2_3+4a_4)\rho^3 + (-1+a_2-a_3+a_4+5a_5)\rho^4 \\ &+ (1-a_2+a_3-a_4+a_5+6a_6)\rho^5 + \ldots] \;.\end{aligned}$$

Comparing coefficients of equal powers of ρ yields

$$b_1 = 2a_2 + 1$$

$$b_2 = 3a_3 + a_2 - 1$$

$$b_3 = 4a_4 + a_3 - a_2 + 1$$

$$b_4 = 5a_5 + a_4 - a_3 + a_2 - 1$$

$$b_5 = 6a_6 + a_5 - a4 + a_3 - a_2 + 1 \;.$$

b_1 is determined by n, however, it will be necessary to select values for the field constants through fifth order terms in ρ to produce a sufficiently accurate field. In addition, B_z may be derived from a potential function by the defining equation:

$$-\nabla V_m = \vec{B}$$

or

$$B_z = \frac{1}{r_o}\frac{\partial Vm}{\partial\xi}$$

where $\xi = z/r_o$, a dimensionless parameter.

The magnetic potential expanded to fifth order terms in ρ and first order in ξ would have the form:

$$V_m = -B_o r_o[(f_{01}+f_{11}\rho+f_{21}\rho^2+f_{31}\rho^3+f_{41}\rho^4+f_{51}\rho^5+\ldots)\xi]$$

B_z at the midplane is then

$$B_z = B_o(f_{01}+f_{11}\rho+f_{21}\rho^2+f_{31}\rho^3+f_{41}\rho^4+f_{51}\rho^5)$$

and there is a direct relationship between the field parameters b_1, b_2..... and f_{11}, f_{21}..... or

$f_{01} = 1$
$f_{11} = b_1$
$f_{21} = b_2$
$f_{31} = b_3$
$f_{41} = b_4$
$f_{51} = b_5$

These scalar potential coefficients can be related directly to the vector potential coefficients if so desired.

Off-Midplane Field Calculations

In order to determine the ion trajectories outside the magnetic midplane, it is necessary to extend the magnetic potentials to higher order terms in ξ. The vector potential would have the form:

$$\begin{aligned}A_\theta = A_o[&(\rho+a_2\rho^2+a_3\rho^3+a_4\rho^4+a_5\rho^5+\ldots)\\ &+(a_{02}+a_{12}\rho+a_{22}\rho^2+a_{32}\rho^3+\ldots)\xi^2\\ &+(a_{04}+a_{14}\rho+a_{24}\rho^2+\ldots.)\xi^4]\end{aligned}$$

where $A_o = B_o r_o$

and the $\vec{B}$ field is determined by

$$B_r = -\frac{1}{r_o}\frac{\partial A\theta}{\partial \xi}$$

and

$$B_z = \frac{1}{r_o}\frac{\partial A\theta}{\partial \rho} + \frac{1}{r_o}\frac{A\theta}{(1+\rho)}$$

Similarly, for the scalar magnetic potential expansion to fifth order terms in ξ we have:

$$\begin{aligned} V_m = -B_o r_o[& (f_{01}+f_{11}\rho+f_{21}\rho^2+f_{31}\rho^3+f_{41}\rho^4+f_{51}\rho^5+\ldots)\xi \\ & +(f_{03}+f_{13}\rho+f_{23}\rho^2+f_{33}\rho^3+\ldots)\xi^3 \\ & +(f_{05}+f_{15}\rho+\ldots)\xi^5] \end{aligned}$$

then

$$\begin{aligned} B_z = B_o[& (f_{01}+f_{11}\rho+f_{21}\rho^2+f_{31}\rho^3+f_{41}\rho^4+f_{51}\rho^5+\ldots) \\ & +3(f_{03}+f_{13}\rho+f_{23}\rho^2+f_{33}\rho^3+\ldots)\xi^2 \\ & +5(f_{05}+f_{15}\rho+\ldots)\xi^4] \end{aligned}$$

and

$$\begin{aligned} B_r = B_o[& (f_{11}+2f_{21}\rho+3f_{31}\rho^2+4f_{41}\rho^3+5f_{51}\rho^4+\ldots)\xi \\ & +(f_{13}+2f_{23}\rho+3f_{33}\rho^2+\ldots)\xi^3 \\ & +(f_{15}+\ldots)\xi^5] . \end{aligned}$$

It can be seen that the above expressions satisfy Maxwell's equation for steady state fields,

$$\nabla \times \vec{B} = 0$$

and by requiring the field to satisfy a second condition

$$\nabla \cdot \vec{B} = 0 ,$$

the off-midplane field coefficients may be determined in terms of the midplane coefficients. This requirement is

$$B_r + (\rho+1)\left(\frac{\partial B_r}{\partial \rho} + \frac{\partial B_z}{\partial \xi}\right) = 0$$

and by equating like powers of ρ and ξ these coefficients are

$$f_{03} = -\frac{(f_{11}+2f_{21})}{6}$$

$$f_{13} = -\frac{(-f_{11}+2f_{21}+6f_{31})}{6}$$

$$f_{23} = -\frac{(f_{11}-2f_{21}+3f_{31}+12f_{41})}{6}$$

$$f_{33} = -\frac{(-f_{11}+2f_{21}+3f_{31}+4f_{41}+20f_{51})}{6}$$

$$f_{05} = -\frac{(-f_{11}+2f_{21}-12f_{31}-24f_{41})}{60}$$

$$f_{15} = -\frac{(2f_{11}-4f_{21}+15f_{31}-12f_{41}-60f_{31})}{60}$$

These off-midplane magnetic scalar potential field coefficients may be related directly to the vector potential coefficients by a similar calculation.

Optical Calculations

There exist many methods for determining the optical properties of a magnetic lens. Point to point ray tracing, exact or approximate mathematical solutions, and experimental measurements are frequently employed. However, the focusing criteria is best determined by direct application of fundamental theorems. For an optical lens, Fermat's principle of least time is applicable, but its mechanical analog, the principle of least action is more appropriate.

$$A = \int_{t_1}^{t_2} \sum_i p_i \dot{q}_i dt$$

is a minimum for any mechanical system where the Hamiltonian is conserved or for a particle in a central field,

$$H = \sum_i p_i \dot{q}_i - L = E \quad \text{(total energy)}$$

and

$$\frac{\delta H}{\delta p_i} = \dot{q}_i, \ \frac{\delta H}{\delta q_i} = \dot{p}_i, \ L = T\text{-}V$$

T = Kinetic energy = $\frac{1}{2}m(\dot{r}^2+r^2\dot{\theta}^2)$

A = Action, V = potential energy.

Since the Action integral is an extremum, any variation of the integration path must be zero, even at the end points or

$$\delta \int_{t_1}^{t_2} \sum_i p_i \dot{q}_i dt = 0 \ .$$

By eliminating the independent variable time, a relationship similar to the principle of minimum energy is expressed by

$$\int_{q_1}^{q_2} \sum_i p_i dq_i = K \ , \text{ a constant}$$

and is commonly associated with Maupertuis. Optically, this is equivalent to

$$\int_1^2 n \cdot ds = K \ , \text{ a constant}$$

where n is the index of refraction. It is easily shown that the Hamiltonian formalism and resulting equations of motion follow directly from the principle of least action. However, in order to simplify the analysis, Lagrangian formalism will be utilized in the following derivations.

The relativistic Lagrangian (L) for a moving charged particle with velocity $\vec{V}$ in a static electric and magnetic field is given by:

$$L = mc^2(1-\sqrt{1-v^2/c^2}) - eU + e/c\ \vec{V}\cdot\vec{A}.$$

where U = electric field = 0 for isolated magnetic systems

$\vec{A}$ = magnetic vector potential

m = particle mass

c = speed of light

e = charge of particle

For the particular case of the RPI magnetic analyzer, using $\vec{A}$ as previously defined, the momentum components are:

$$p_r = \frac{\delta L}{\delta r} = m\gamma\dot{r}$$

$$p_\theta = m\gamma r^2\dot{\theta} - m\gamma vr(\rho + a_2\rho + \ldots)$$

$$\gamma = (1-v^2/c^2)^{-\frac{1}{2}}$$

where by equating the centrifugal and magnetic forces,

$$B_o = \frac{m\ Ve}{er_o} \qquad \text{also } A_o = B_o r_o\ .$$

It is no longer necessary to retain the relativistic correction term γ since it is negligible and, in the least action formalism, it cancels out. However, it is essential for relating the particle momentum to the magnetic field strength.

In continuing the investigation of the optical properties of a magnetic lens, only the first vector potential expansion coefficient (a_2) will be retained. Also, the basic field inhomogenity (n) is related to a_2 by

$$-n = 2a_2+1 \ .$$

However, the selection of n can be made without regard to the higher order field expansion terms. The final ion trajectory calculations will include terms up to fifth order, as derived previously.

The kinetic energy, T, is given by

$$T = \tfrac{1}{2}mv_o^2 = \tfrac{1}{2}m(\dot{r}^2+r^2\dot{\theta}^2)$$

and

$$p_r{}^2 = m^2\dot{r}^2$$

thus

$$p_r \cong [m^2v_o^2 - \frac{p_\theta^2}{r^2} - \frac{2p_\theta mv_o(\rho+a_2\rho^2)}{r} - m^2v_o 2\rho^2]^{\frac{1}{2}}$$

The initial system conditions are:

$$\rho = 0, \ r = r_o$$

$$\theta = 0$$

$$\dot{r} = V_o \ \mathrm{Sin}\ \alpha$$

$$\dot{\theta} = \frac{V_o}{r_o} \ \mathrm{Cos}\ \alpha$$

where α is the initial radial angular divergence.

In terms of ρ

$$P_\theta = mr_o{}^2(\rho+1)^2\dot{\theta} + er_o(\rho+1)A_\theta$$

$$= mr_o v_o \operatorname{Cos}\alpha$$

$$= mr_o v_o(1-\frac{\alpha^2}{2}+\ldots)$$

The circular action is then

$$\int P_\theta d\theta = mr_o v_o(1-\frac{\alpha^2}{2})\Phi$$

where $\Phi = \sqrt{2}\,\pi$, for this system.

The radial action to first order is found by

$$P_r = \pm\, mv_o \left\{\alpha^2[1-\rho+(2+a_2)\rho^2]-2(1+a_2)\rho^2\right\}^{\frac{1}{2}}$$

$$\int_{r_o}^{r_{max}} P_r d_r = 2\, r_o \int_0^{\rho_{max}} P_r d\rho$$

where ρ max may be calculated from the condition

$\rho = \rho_{max}$

when $P_r = 0$.

Thus

$$P_\theta = mr_o v_o(1-\frac{\alpha^2}{2})$$

$$= mr_o v_o[(1+\rho_{max})-(1+\rho_{max})(\rho_{max}+a_2\rho_{max}^2)]$$

or

$$\alpha^2 = 2(1+a_2)\rho_{max}^2$$

and the action integral is

$$2r_o\int_0^{\rho_{max}} \pm\, mv_o \left\{\alpha^2[1-\rho+(2+a_2)\rho^2]-2(1+a_2)\rho^2\right\}^{\frac{1}{2}} d\rho$$

factoring out constant terms yields:

$$2r_o m v_o \sqrt{2(1+a_2)} \int_o^{\rho_{max}} \left\{\alpha^2 \frac{[1-\rho+(2+a_2)\rho^2]}{2(1+a_2)} - \rho^2\right\}^{\frac{1}{2}} d\rho$$

A change of variables of the form

$$\lambda^2 = f(\rho)^2+\rho^2 \qquad \text{where} \quad \rho = \lambda \sin \mu$$

and

$$f(\rho)^2 = \frac{\alpha^2[1-\rho+(2+a_2)\rho^2]}{2(1+a_2)}$$

also

$$\lambda^2 = \rho^2_{max}, \text{ ignoring terms higher than } \rho^2$$

thus

$$2 \int_o^{\rho_{max}} f(r)d\rho = 2 \int_o^{\pi/2} \frac{\lambda^2}{2} d\mu$$

in ρ space.

Therefore the radial action is given by

$$\text{Action } (r) = mr_o v_o \sqrt{2(1+a_2)} \int_o^{\pi/2} \left\{\rho^2_{max}\right\} d\mu$$

$$= mr_o v_o \sqrt{2(1+a_2)} \left\{\frac{\pi}{2} \rho^2_{max}\right\}$$

The azimuthal action in terms of ρ_{max} is

$$\text{Action } (\theta) = mr_o v_o [1-(1+a_2)\rho^2_{max}]\Phi \text{ .}$$

Total action must be independent of ρ_{max} or

$$a_2 = \frac{\pi^2}{2\Phi^2} - 1$$

for proper focusing. In terms of the field expansion coefficient,

$$b_1 = 2a_2+1 = \frac{\pi^2}{\Phi^2} - 1$$

and for the 255° analyzer

$$\Phi = \sqrt{2}\,\pi \qquad b_1 = -n = -\tfrac{1}{2}$$

Thus the basic field inhomogenity of 0.5 should be used and the higher order terms may be adjusted to maximize radial focusing. By extending this calculation to higher order terms, optimum theoretical values may be determined for other field expansion constants. However, the truncated theoretical field parameters do not, in general, provide the most ideal focusing conditions. The major intent of this study is to determine experimentally, with the aid of computed trajectories, optimum field expansion parameters through the fifth order.

Trajectory Calculations

The theoretical field expansion and equations of motion developed in the previous section can now be applied to the ion trajectory calculations with the aid of a high speed digital computer. Basically, the program calculates each ion orbit in a stepwise process from its point of origin through several hundred steps to its focal point at 255°. Since the $\vec{B}$ field is defined at every point and the force on the ion is given by Lorentz as

$$\vec{F} = q(\vec{V} \times \vec{B}),$$

it is only necessary to solve the resulting second order differential equations. The numerical methods developed by Nyström[11] were employed for the integration in three dimensions. Although the program was designed to specifically calculate alpha particles in a 255^{o} system, it can be modified to calculate ion trajectories for any sector type magnetic analyzer with focal and object point in the field (see Fig. 8).

In order to obtain the most desirable focusing properties, the input field parameters listed in Table B were varied as indicated. For calculational purposes, the field is assumed to extend from R = 0 to infinity, however, the calculated maximum and minimum radial position of the peripheral ion trajectories may be used to determine the required field extent for any specified focusing critera. It should be noted that several different combinations of field expansion coefficients will produce the focal properties of figures 9 through 18. In fact, the final values of the higher order terms were determined by trial and error variance methods. The basic field inhomogenity value of 0.5 was chosen so that the source and focus points would fall within the magnetic field, thus eliminating a detailed aximuthal fringing field analysis (see figure 8). However, the radial fringing field of this analyzer will be considered in order to extend the usable field area as much as possible.

The device's transmission characteristics is

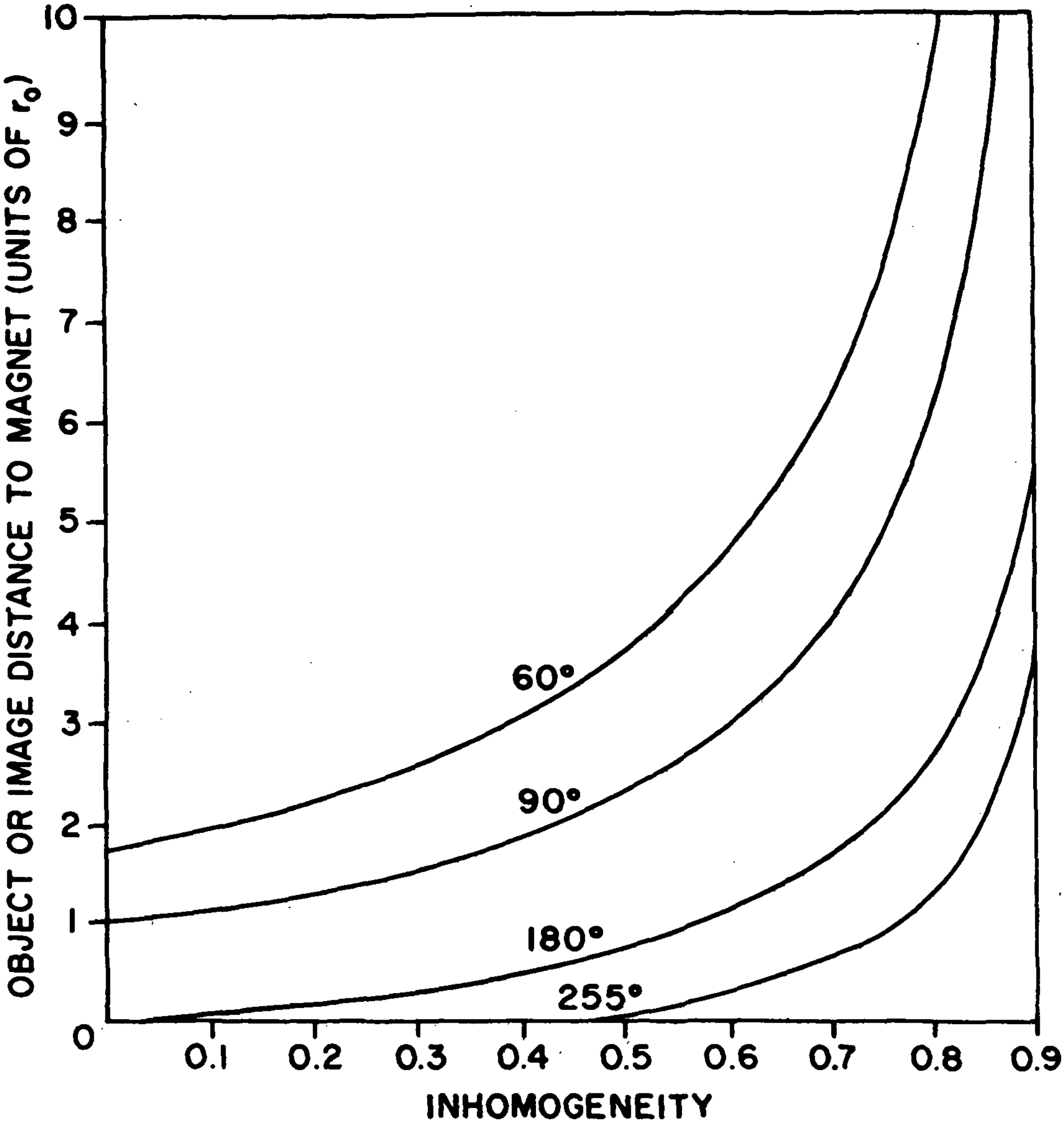

The focal position for 255°, 180°, 90°, and 60° sector magnets using symmetric object-image locations.

Figure 8

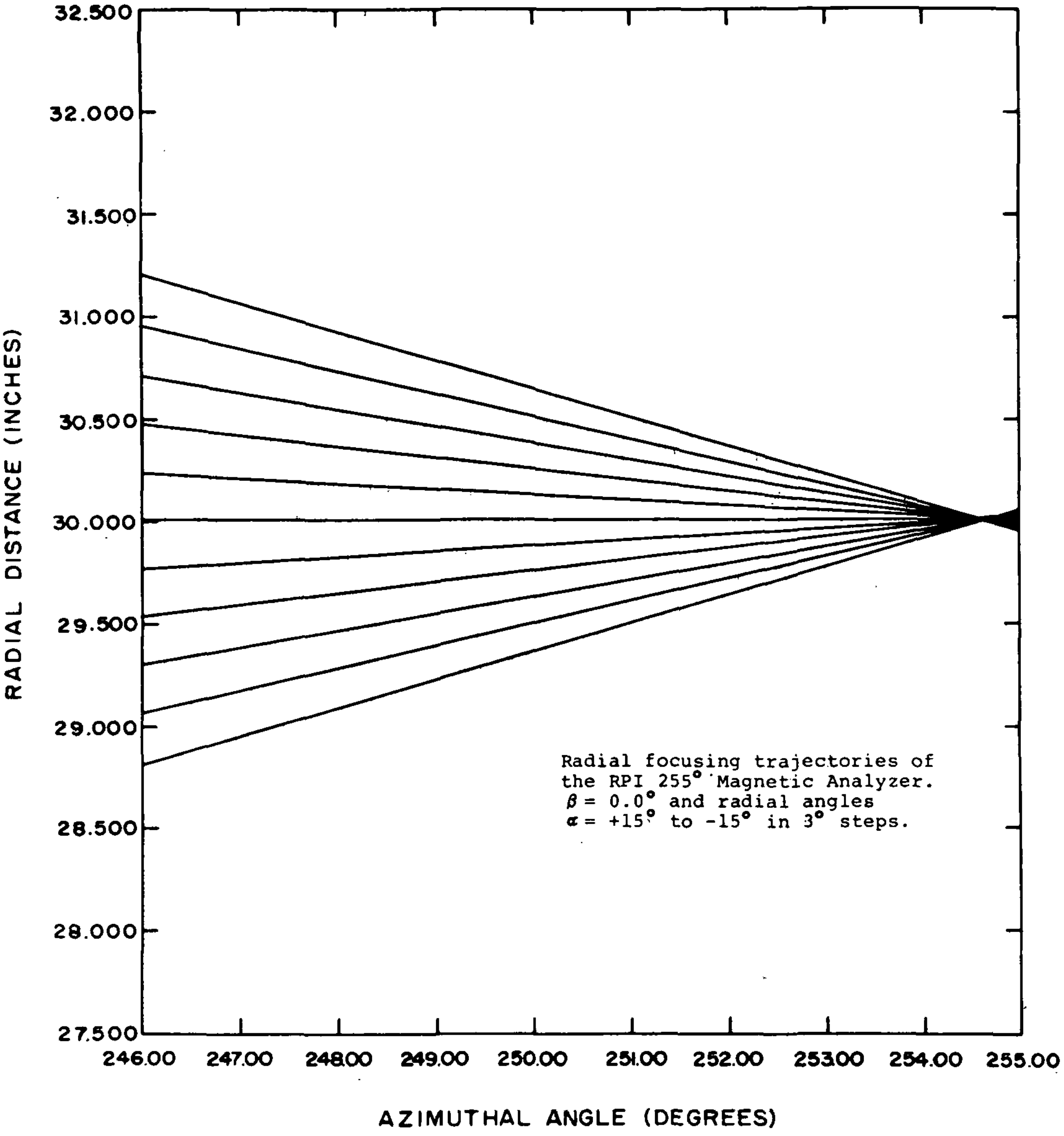
32.500
32.000
31.500
31.000
30.500
30.000
29.500
29.000
28.500
28.000
27.500
RADIAL DISTANCE (INCHES)
246.00
247.00
248.00
249.00
250.00
251.00
252.00
253.00
254.00
255.00
AZIMUTHAL ANGLE (DEGREES)
Radial focusing trajectories of
the RPI 255° Magnetic Analyzer.
β = 0.0° and radial angles
α = +15° to -15° in 3° steps.

Figure 9

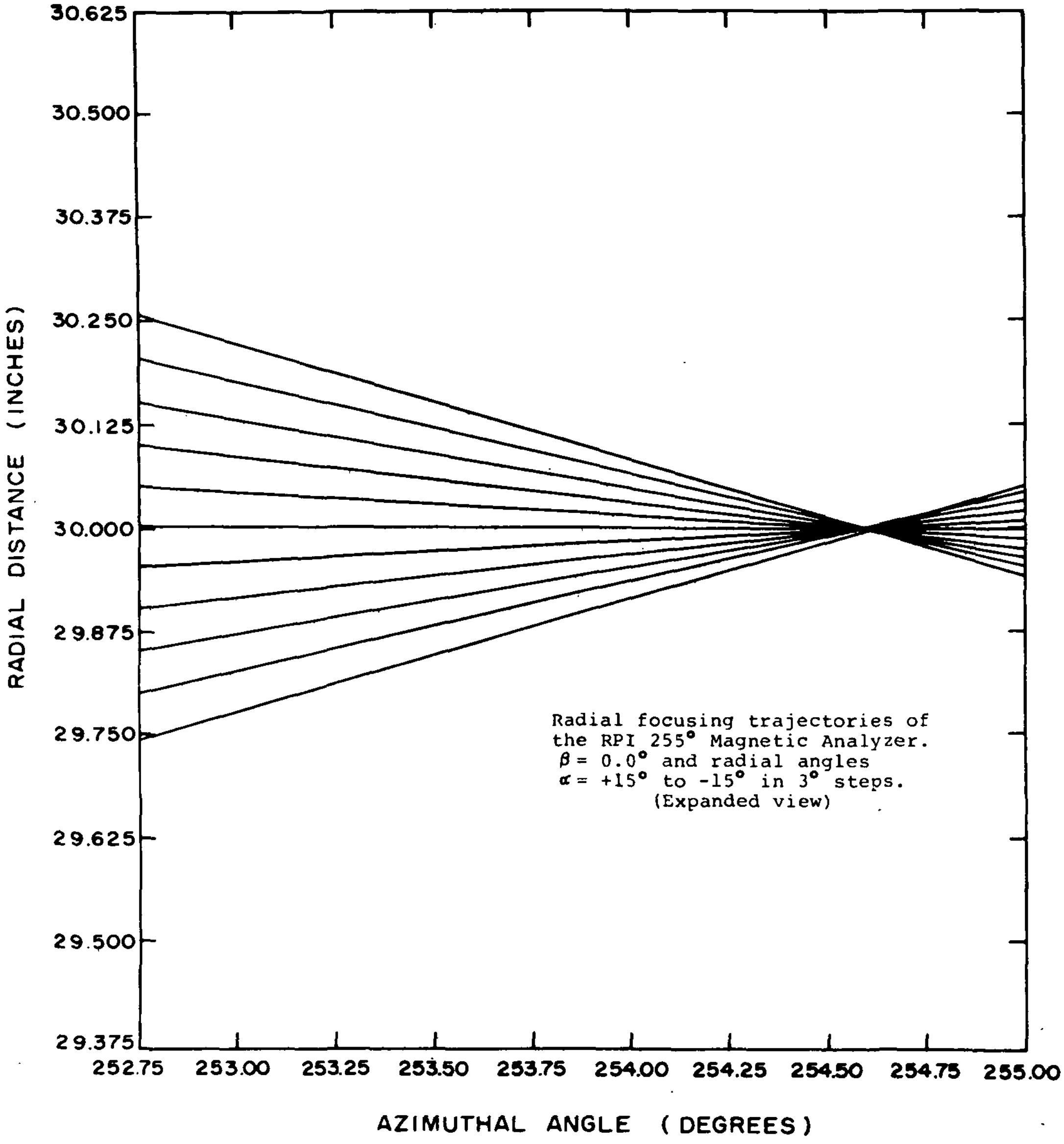

Radial focusing trajectories of the RPI 255° Magnetic Analyzer. $\beta = 0.0°$ and radial angles $\alpha = +15°$ to $-15°$ in 3° steps. (Expanded view)

Figure 10

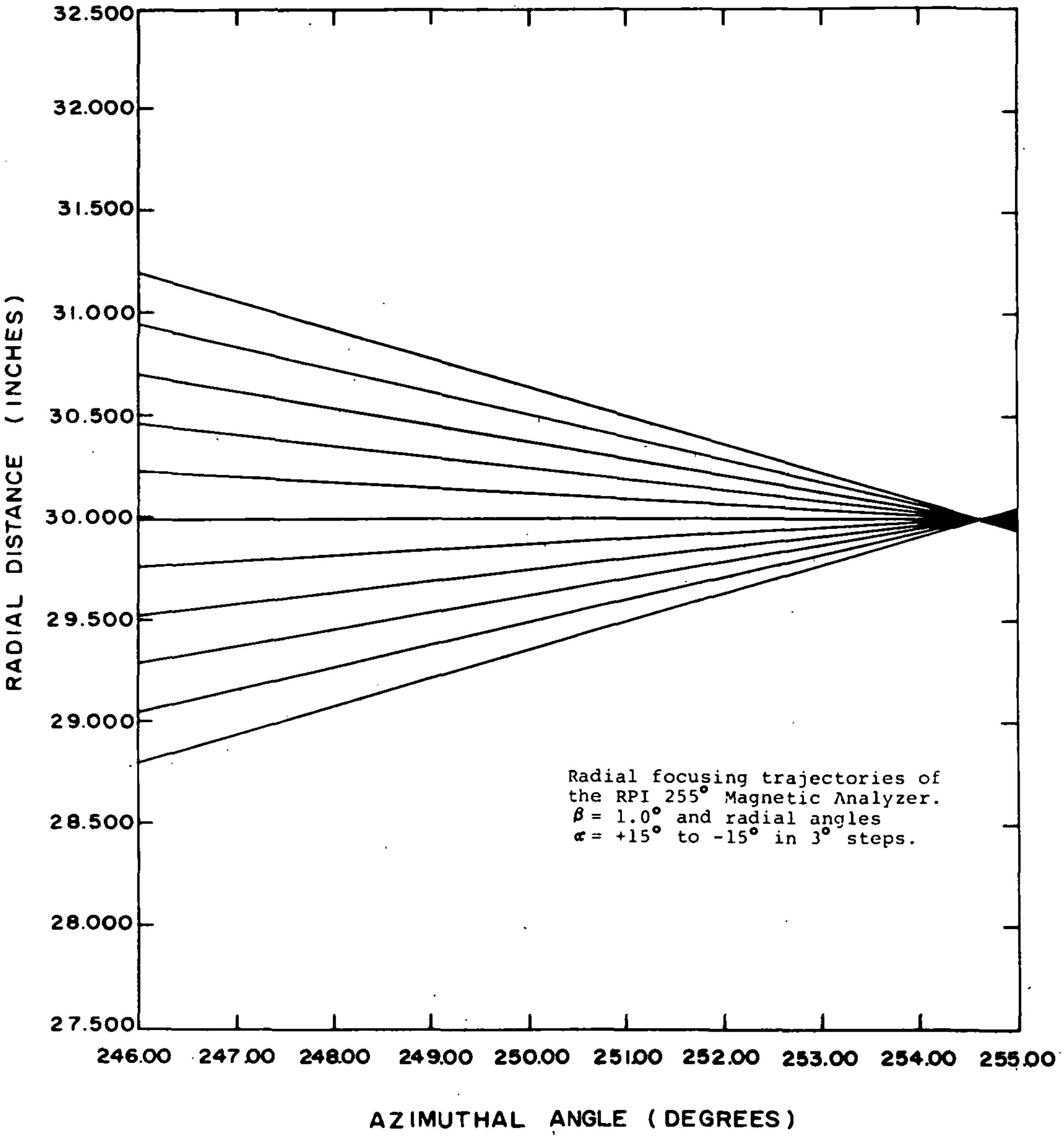
32.500
32.000
31.500
31.000
30.500
30.000
29.500
29.000
28.500
28.000
27.500
RADIAL DISTANCE (INCHES)
246.00
247.00
248.00
249.00
250.00
251.00
252.00
253.00
254.00
255.00
AZIMUTHAL ANGLE (DEGREES)
Radial focusing trajectories of the RPI 255° Magnetic Analyzer.
β = 1.0° and radial angles
α = +15° to -15° in 3° steps.

Figure 11

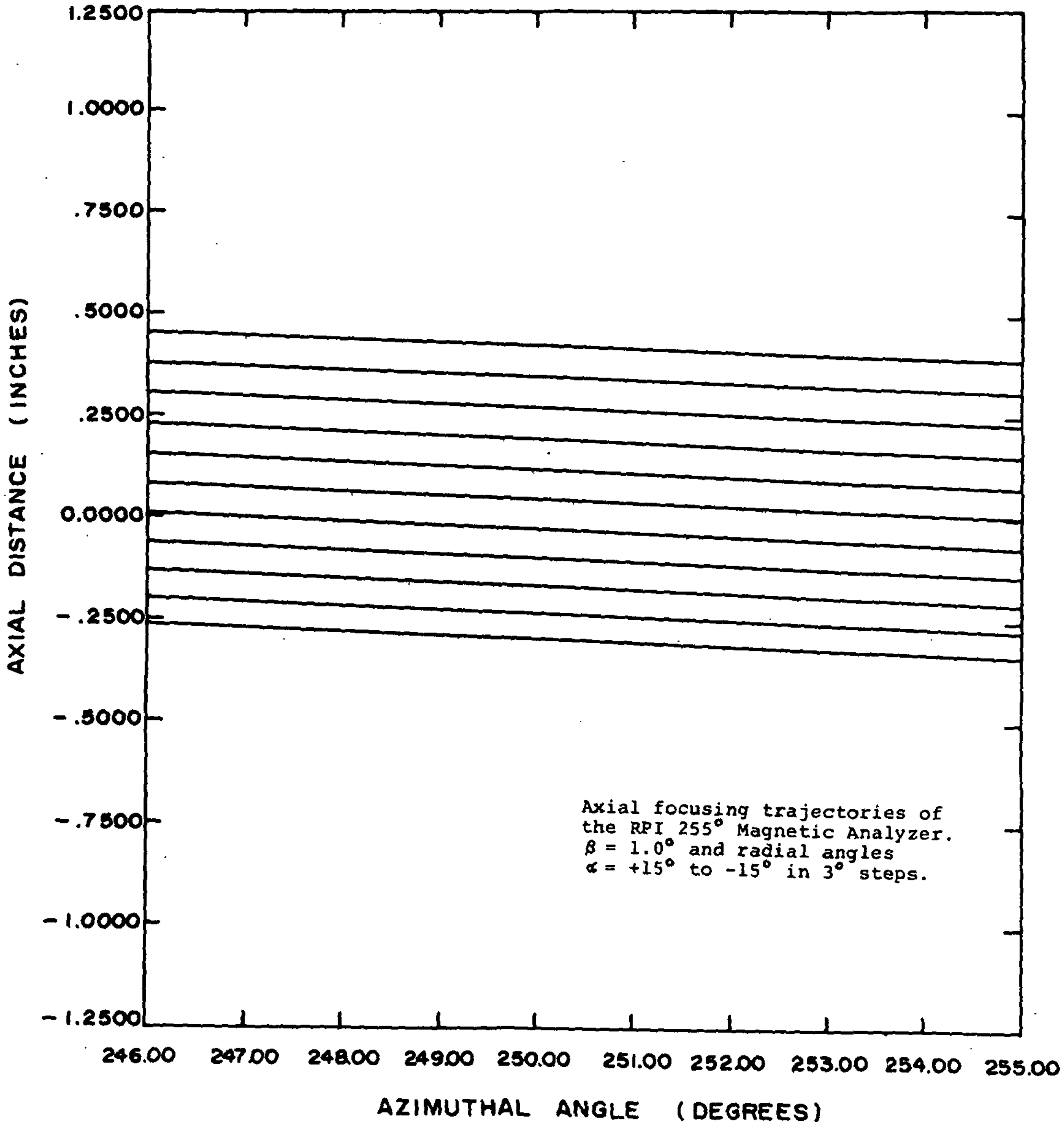

1.2500
1.0000
.7500
.5000
.2500
0.0000
-.2500
-.5000
-.7500
-1.0000
-1.2500
AXIAL DISTANCE (INCHES)
246.00
247.00
248.00
249.00
250.00
251.00
252.00
253.00
254.00
255.00
AZIMUTHAL ANGLE (DEGREES)
Axial focusing trajectories of the RPI 255° Magnetic Analyzer.
β = 1.0° and radial angles
α = +15° to -15° in 3° steps.

Figure 12

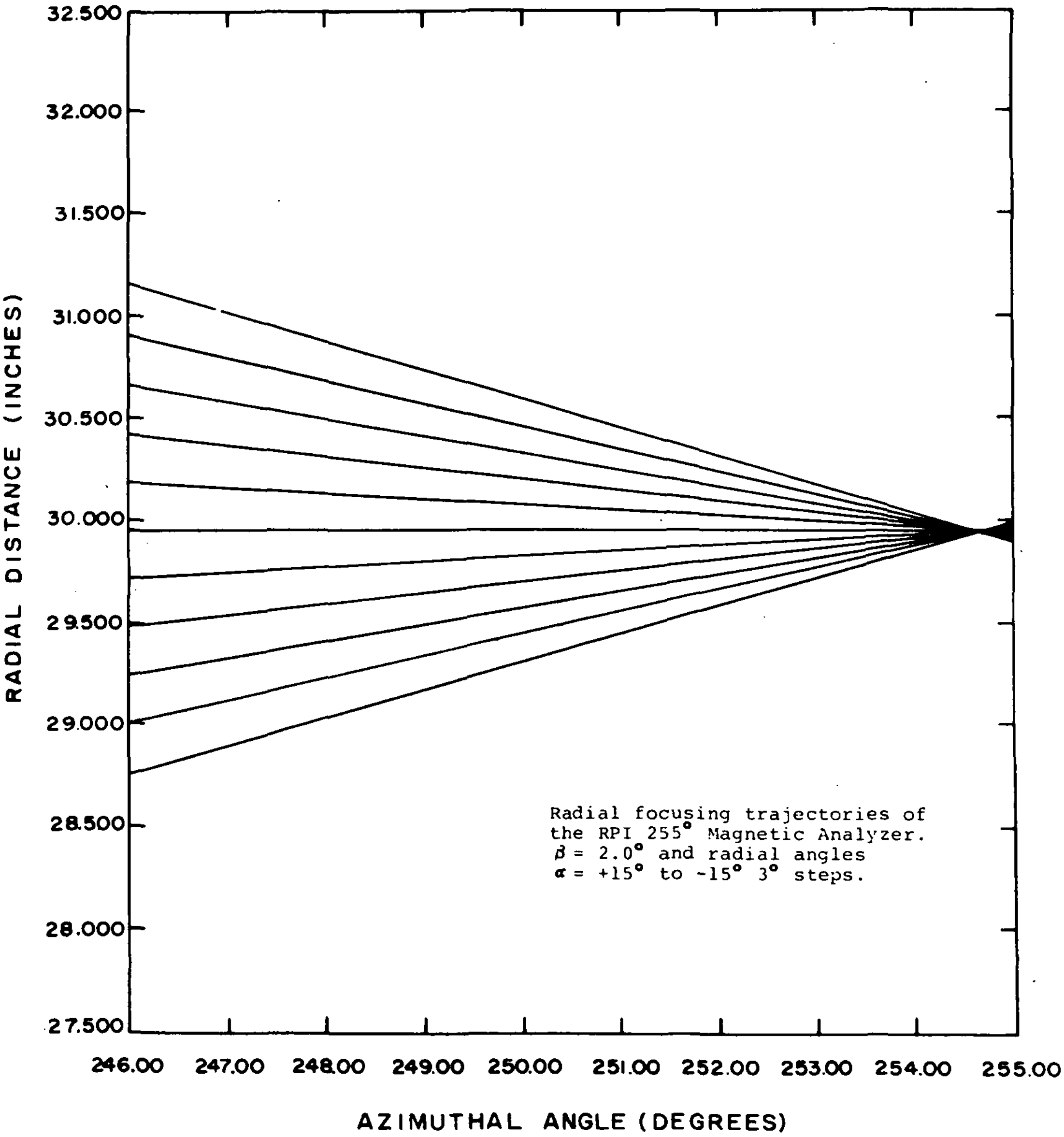
32.500
32.000
31.500
31.000
30.500
30.000
29.500
29.000
28.500
28.000
27.500
RADIAL DISTANCE (INCHES)
246.00
247.00
248.00
249.00
250.00
251.00
252.00
253.00
254.00
255.00
AZIMUTHAL ANGLE (DEGREES)
Radial focusing trajectories of
the RPI 255° Magnetic Analyzer.
β = 2.0° and radial angles
α = +15° to -15° 3° steps.

Figure 13

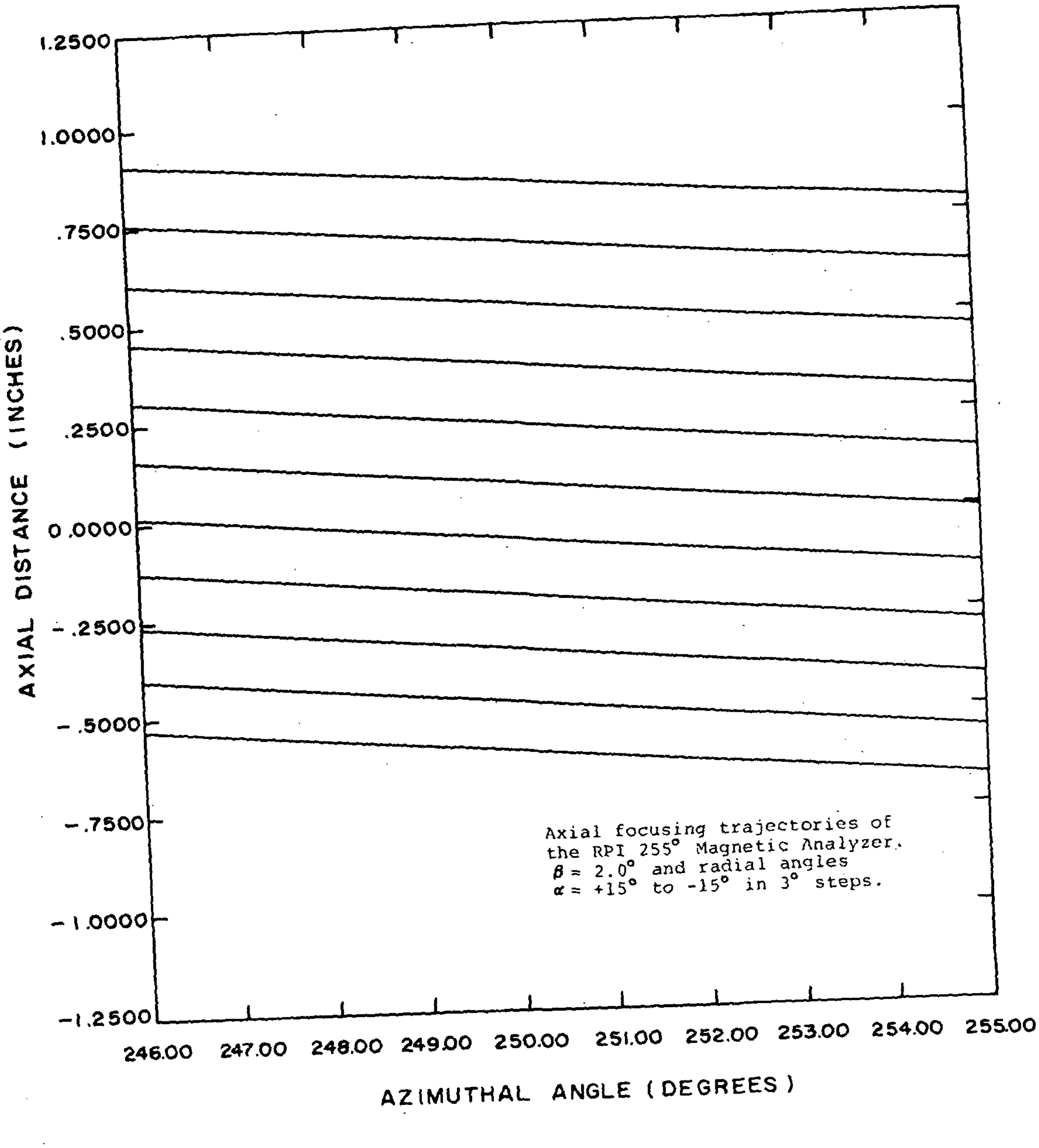
1.2500
1.0000
.7500
.5000
.2500
0.0000
-.2500
-.5000
-.7500
-1.0000
-1.2500
AXIAL DISTANCE (INCHES)
246.00
247.00
248.00
249.00
250.00
251.00
252.00
253.00
254.00
255.00
AZIMUTHAL ANGLE (DEGREES)
Axial focusing trajectories of the RPI 255° Magnetic Analyzer. β = 2.0° and radial angles α = +15° to -15° in 3° steps.

Figure 14

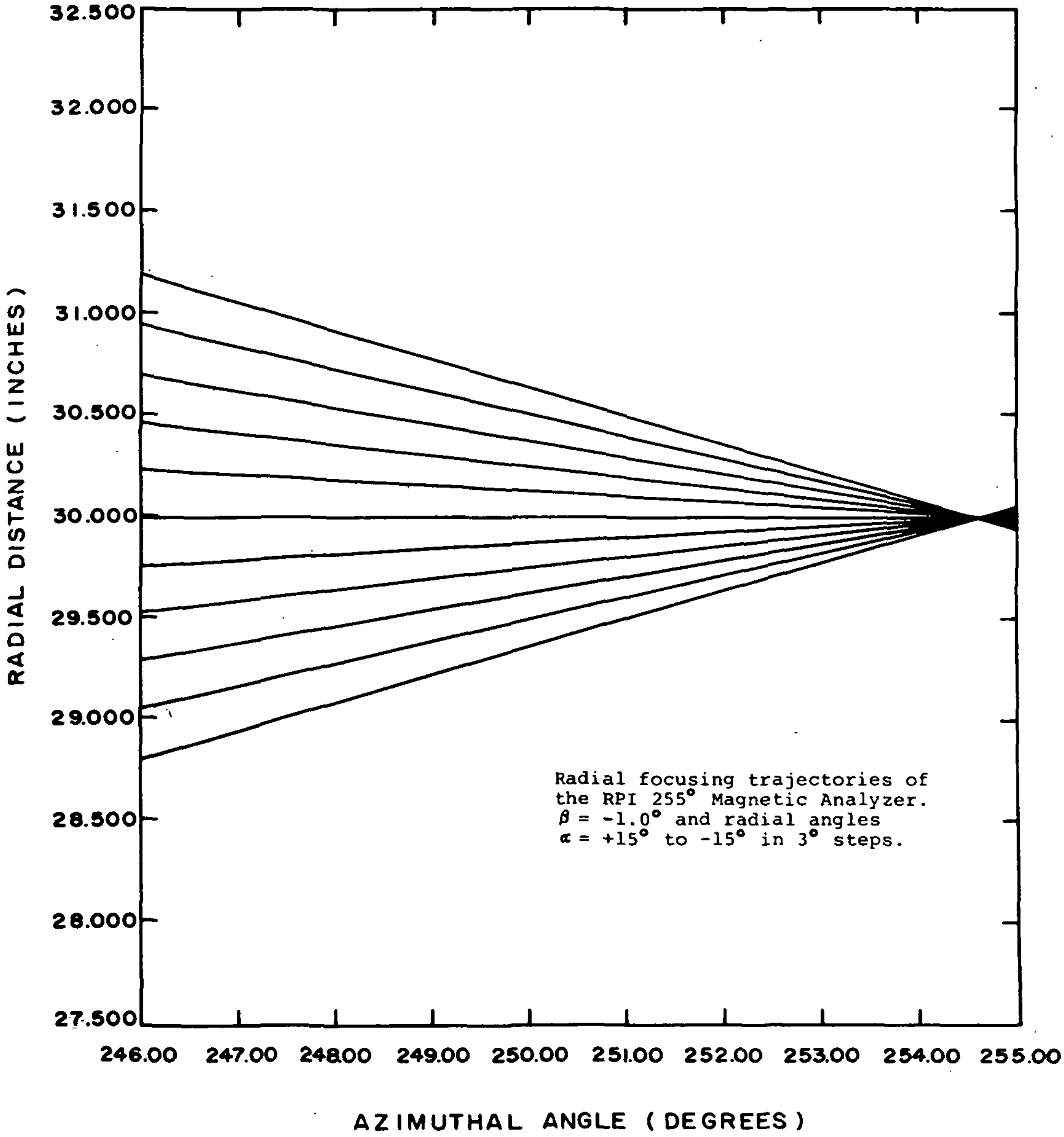

Radial focusing trajectories of the RPI 255° Magnetic Analyzer. $\beta = -1.0°$ and radial angles $\alpha = +15°$ to $-15°$ in 3° steps.

Figure 15

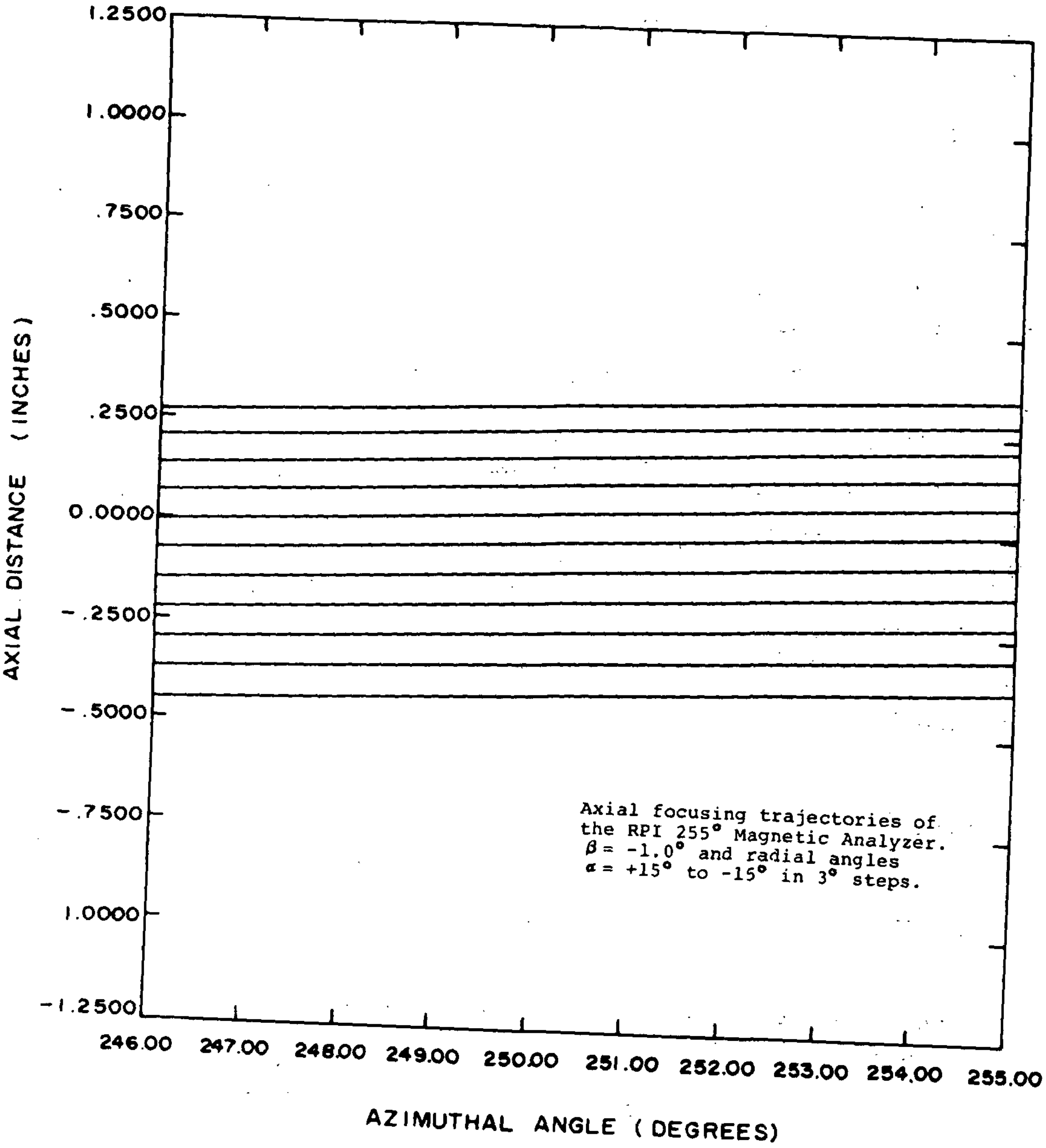

Axial focusing trajectories of the RPI 255° Magnetic Analyzer. $\beta = -1.0°$ and radial angles $\alpha = +15°$ to $-15°$ in 3° steps.

Figure 16

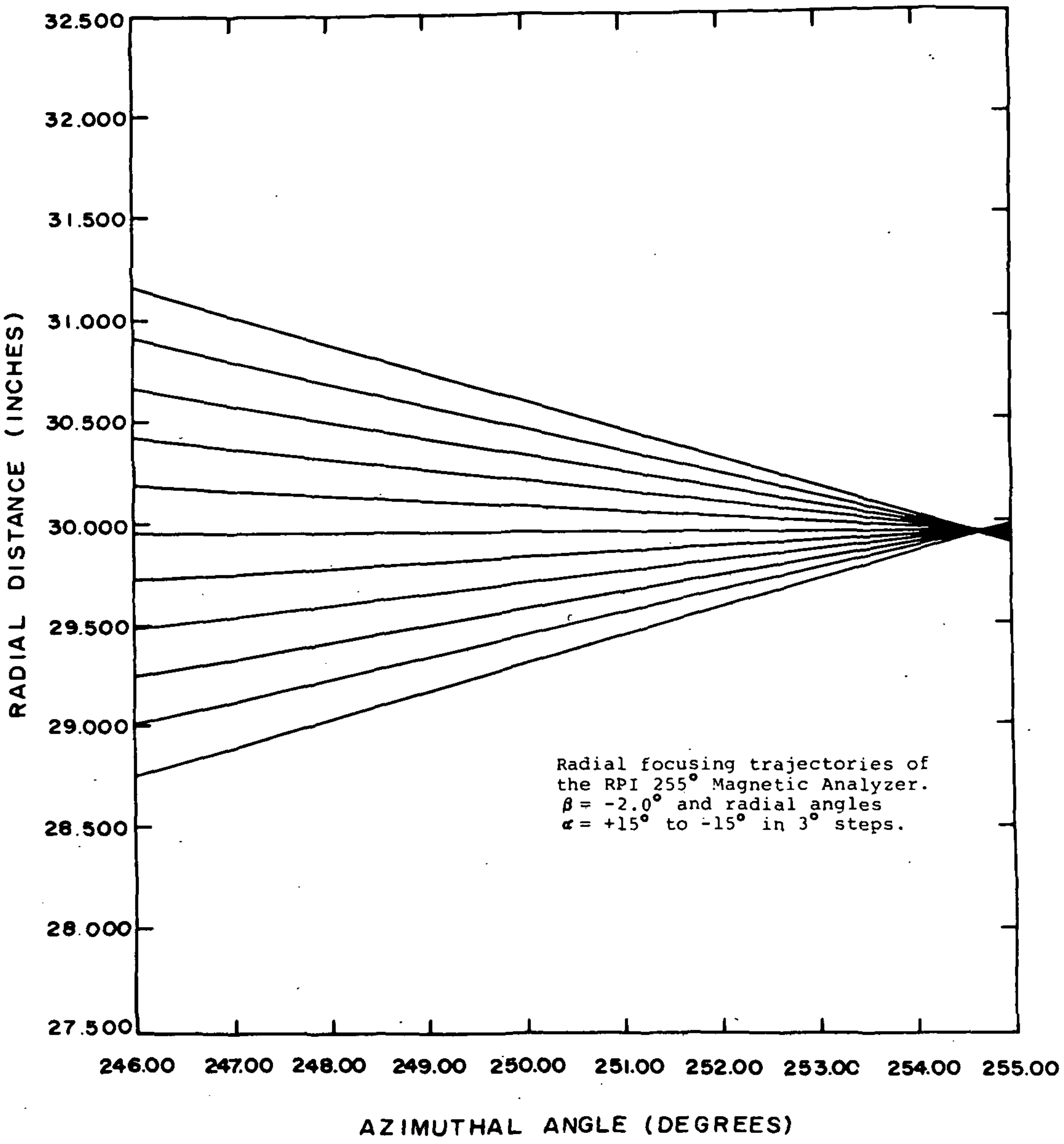
32.500
32.000
31.500
31.000
30.500
30.000
29.500
29.000
28.500
28.000
27.500
RADIAL DISTANCE (INCHES)
246.00
247.00
248.00
249.00
250.00
251.00
252.00
253.00
254.00
255.00
AZIMUTHAL ANGLE (DEGREES)
Radial focusing trajectories of
the RPI 255° Magnetic Analyzer.
β = -2.0° and radial angles
α = +15° to -15° in 3° steps.

Figure 17

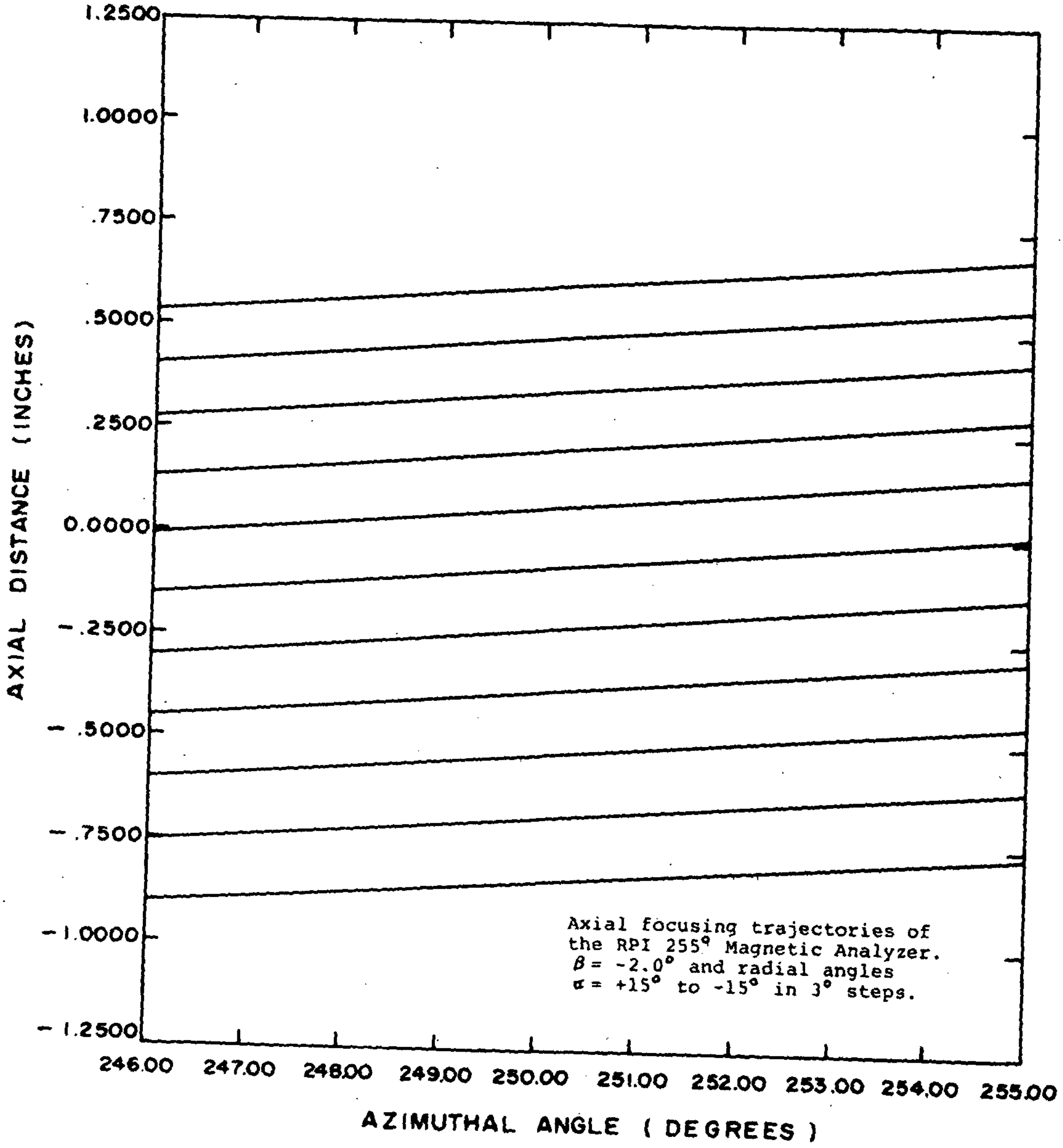
1.2500
1.0000
.7500
.5000
.2500
0.0000
-.2500
-.5000
-.7500
-1.0000
-1.2500
AXIAL DISTANCE (INCHES)
246.00
247.00
248.00
249.00
250.00
251.00
252.00
253.00
254.00
255.00
AZIMUTHAL ANGLE (DEGREES)
Axial focusing trajectories of
the RPI 255° Magnetic Analyzer.
β = -2.0° and radial angles
α = +15° to -15° in 3° steps.

Figure 18

Table B

Ion Trajectory Calculation Parameters

Parameter	Values applied to the 255° system	Final Design Parameters
Mean Radius (R_o)	25.0 - 30.0 inches	27.8 inches
Source (R,Z,θ)	Point Source 30.0,0.0,0.0	Point Source 27.8,0.0,0.0
Particle Mass (α - particle)	4.0	4.0
Particle Energy	5.0 ± 0.5 MeV	5.0 ± 0.5 MeV
Sector Angle	255°	255°
Radial Acceptance angle (α)	-15.0° to + 15.0° (3° steps)	-15.0° to ± 15.0° (3° steps)
Axial Acceptance Angle (β)	-2.0° to + 2.0° (1° steps)	-2.0° to + 2.0° (1° steps)
Magnetic Field Parameters		
b_1	-0.5	-0.5
b_2	0.125	0.125
b_3	0.0625	0.0625
b_4	-0.10 to -0.15	-0.125
b_5	0.75 to 0.125	0.095
Extent of Radial Field	16 to 44 inches	16 to 44 inches
Gap width	3 - 5 inches tapered	4.0 inches at R = 27.8 inches

determined by the radial and axial acceptance angles. Resolution may be determined by the formula

$$\frac{\Delta E}{E}\Big|_T = \frac{W}{d}$$

where

ΔE = the expected energy deviation of the particle due to focusing properties

E = the particle's energy

W = focusing image width

d = the diameter of the magnetic analyzer

T = a given transmission value.

The maximum radial acceptance angle is determined by the extent of the usable magnetic field. For this system, the radial acceptance angle is limited to 15 degrees. As the figures indicate, the radial focal point diverges as radial angular acceptance is increased. From Fig. 13 it can be seen that for the maximum transmission value of 0.3% of 4π steradians, the corresponding energy resolution is

$$\frac{\Delta E}{E}\Big|_{0.3\%} = \frac{1}{1500}$$

By limiting the azimuthal acceptance angle to ± 1.0 degree, the energy resolution is from figure 11,

$$\frac{\Delta E}{E}\Big|_{0.15\%} = \frac{1}{6000}$$

while the calculated maximum resolution for midplane focusing in Fig. 10 is

$$\frac{\Delta E}{E}\Big|_{\text{midplane}} = \frac{1}{12000}$$

Thus it can be seen that the selected values of field coefficients result in satisfactory optical characteristics of the system. The azimuthal calculations indicate that the image of a point source (at maximum acceptance) will be a line. This is as expected since, in a double focusing device, optimum radial focusing criteria will not produce the optimum axial focal pattern. This design is based, of course, on optimizing the radial focusing properties.

Focal Pattern Computation

The optimum field expansion coefficients have been selected for focusing 5 MeV alpha particles; the transmission and focal properties of alpha particles with varying energies may be investigated. By employing the same method and programs used in the 5 MeV case, the focal patterns for alpha particles with energies varying from 4.5 to 5.5 MeV in 0.1 MeV increments can be calculated. The plane in which these images formed made a 42° angle with the mean radius orbit at an azimuthal angle of 255°.

While examining the particle paths from source to focal point during this energy sweep calculation, it was found that the maximum radial deviations from the mean radius were not symmetric. The maximum radial extent of the 5.5 MeV alpha particles fell beyond the pole piece outside edge, while the 4.5 MeV inner trajectories were well within the inside pole piece edge as shown in Fig. 19. In order to optically center the particle paths, it was apparently necessary to reduce the mean radius and thus equalize the maximum inside and outside radial deviations from the mean radius. By varying the mean radius down to a minimum value of 25.0 inches, an optimum value of 27.8 inches produced the centered pattern indicated in Fig. 19. The maximum axial extent of all calculated trajectories must be less than pole piece gap at any given radius, otherwise the maximum vertical acceptance angle will be reduced.

The optical mean radius was therefore changed from 30.0 inches to 27.8 inches. A reinvestigation of the focal pattern indicated that it remains approximately valid for the reduced radius design. Only a scale factor on the order of 0.927 is required to convert the previously calculated 30 inch axial and radial plots over to equivalent 27.8 inch plots. Table B lists the final field parameters which completely determine the theoretical optical properties of the RPI 255° analyzer. It is now necessary to calcu-

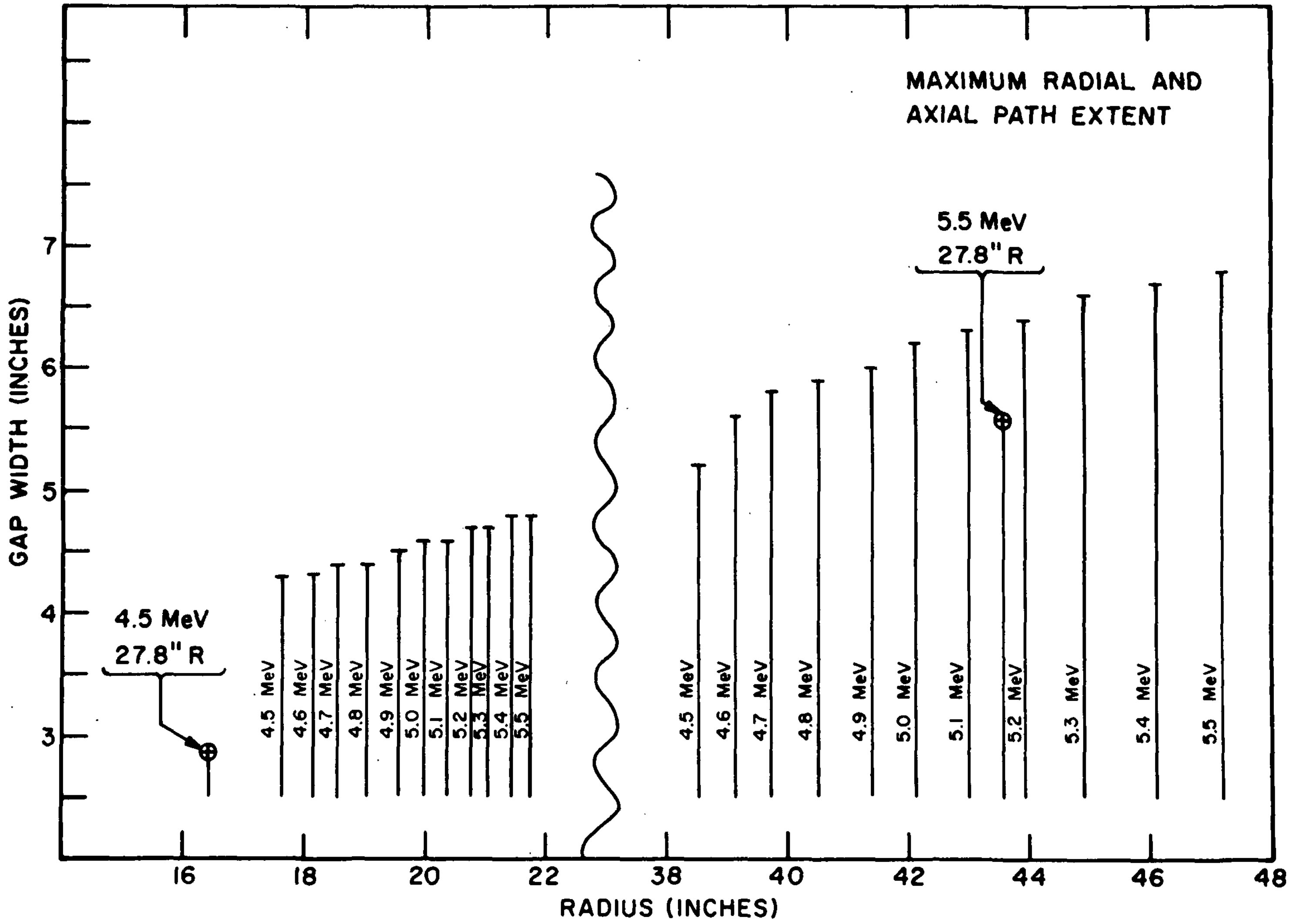
MAXIMUM RADIAL AND AXIAL PATH EXTENT
GAP WIDTH (INCHES)
RADIUS (INCHES)
3
4
5
6
7
16
18
20
22
38
40
42
44
46
48
4.5 MeV 27.8" R
5.5 MeV 27.8" R
4.5 MeV
4.6 MeV
4.7 MeV
4.8 MeV
4.9 MeV
5.0 MeV
5.1 MeV
5.2 MeV
5.3 MeV
5.4 MeV
5.5 MeV
4.5 MeV
4.6 MeV
4.7 MeV
4.8 MeV
4.9 MeV
5.0 MeV
5.1 MeV
5.2 MeV
5.3 MeV
5.4 MeV
5.5 MeV

Figure 19

late a pole piece contour which will reproduce these physical properties with a high degree of accuracy.

Shim Contour Calculation

It is by no means a simple task to construct a magnetic system which will reproduce a given theoretical field. Practical problems such as material impurities, fringing field distortions, magnetic saturation, and construction dimension tolerances have always plagued the experimentalist. In this work, only the two major design problems of saturation and fringing fields are considered, with considerable emphasis on the latter.

If one is willing to give up the outer portions of a magnetic analyzer which are distorted by fringing fields, the pole piece design is greatly simplified. Since the magnetic lines of force enter and exit the pole pieces normal to their surfaces, the pole piece contour may be considered to be an equipotential surface. It would only be necessary to shape the contour according to an appropriate equipotential contour line from the theoretical field in order to produce an acceptable magnetic field. If this approach were taken for the RPI 255^{o} analyzer, the maximum transmission value would be reduced.

The large yoke system was designed to maintain the maximum magnetic induction within the iron components to values well below saturation. In addition, sharp points and edges were eliminated from the pole piece design since the magnetic flux could easily saturate such areas. In particular, the inside and outside edges were rounded in order to prevent saturation effects from distorting the fringing field regions.

One of the basic goals of this project is to maximize the actual transmission characteristics of the device. Therefore, a method must be developed to adjust the inside and outside edges of a truncated equipotential contour in order to compensate for the radial fringing fields. A relaxation type calculation appeared well suited for this situation. By superimposing a radial cross-section of the analyzer over a 0.2 by 0.2 inch grid as depicted in Fig. 20, it is possible to solve Laplace's equation numerically in order to determine the magnetic field strength at each mesh point. The shim contour may then be varied until the fringing field effect is eliminated and the required magnetic field shape obtained.

Boundary conditions were specified as Vm = 10 at the shim surface and Vm = 0 at the magnetic midplane. The potential at any given point is calculated from the potential at its four nearest neighboring points. This type of calculation is straightforward, except within the gap of the pole pieces. Here, the net spacing is modified by adjusting the grid potential values since the actual shim contour

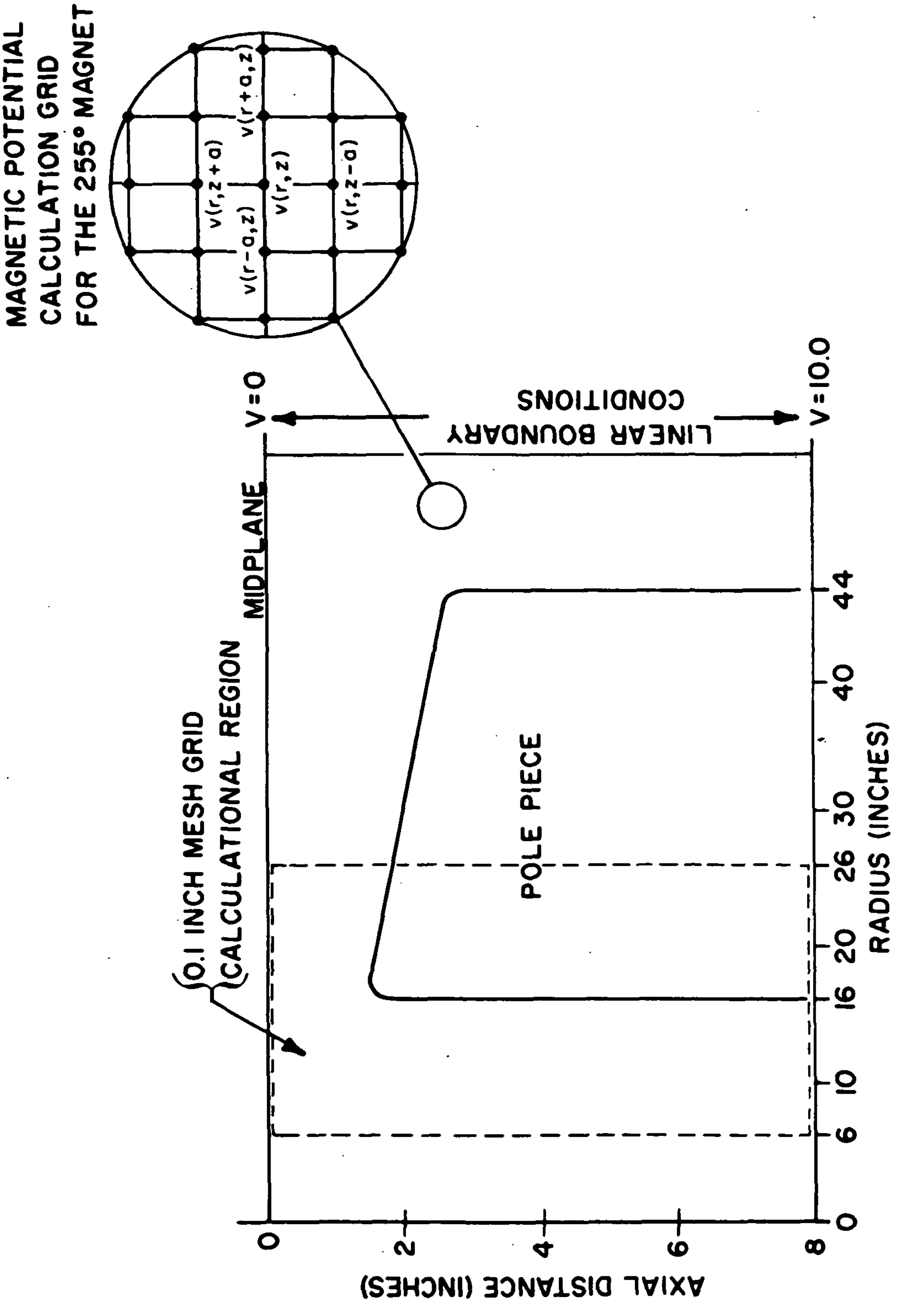
MAGNETIC POTENTIAL CALCULATION GRID FOR THE 255° MAGNET
v(r,z+a)
v(r+a,z)
v(r-a,z)
v(r,z)
v(r,z-a)
V=0
LINEAR BOUNDARY CONDITIONS
V=10.0
MIDPLANE
0.1 INCH MESH GRID
CALCULATIONAL REGION
POLE PIECE
0
6
10
16
20
26
30
40
44
RADIUS (INCHES)
0
2
4
6
8
AXIAL DISTANCE (INCHES)

Figure 20

does not coincide with normal net spacing. Table C lists the infinite field contour coordinates while Table D presents the results of comparing the ideal (infinite contour extent) field shape and the actual potential relaxation calculation for a mean radius system of 30 inches. Agreement is relatively good except at the radial fringing field, which is as expected.

In general, a negative field error at a specific radius indicates that the gap width is too large and should be reduced. Conversely, a positive error may be reduced by increasing the gap width. Therefore, it is a simple matter to eliminate the field error at a single point by experimentally adjusting the gap width at that point. However, there is a strong interaction among neighboring points and minimizing the error at all points simultaneously is a formidable task. Three approaches were taken in order to solve the problem and produce an acceptable contour.

1. Linear Correction Method. The first method applied was a process where each shim point was linearly corrected relative to the calculated error at the point, or

$$D'(a) = D(a) + K \cdot E(a)$$

where,

$D(a)$ = gap width at radius a

$D'(a)$ = adjusted gap width at radius a

K = linear adjusting constant

$E(a)$ = the magnetic field error at radius a.

After applying this equation to each point across the extent of the pole piece, the corrected contour shape was coded back into the relaxation program. This iteration process was repeated several times in an attempt to minimize the calculated errors. Upon completing approximately twenty cycles, it became apparent that this method was not producing the desired results. Two problems were encountered. First of all, several shim points were being overcorrected during the iteration process, resulting in wavelike oscillations (positive to negative) of the computed error shape. Reducing the value of K damped the oscillations, however, after several iterations the shim contour was being "broken up" by this process. Specifically, wherever the error curve switched from negative to positive, the corrective process generated a sharp step or discontinuity in the physical contour. Eventually the curve would have assumed a sawtooth form.

2. Contour Smoothing. Since the first method appeared to be adjusting the contour in the right direction, it seemed that only a mathematical

smoothing process was required. Recalling that the original magnetic field is the result of a fifth order Taylor expansion, it was felt that a high order polynominal fit of the corrected shim data would produce results close to the optimum shape. This conclusion is based on the assumption that the optimum shape is truly a mathematically well-behaved function. However, the application of polynomial fits up to twentieth order did not give satisfactory results. It appeared that the fitting process so distorted the existing shape that the linear correcting method could not bend the curve toward the optimum contour. Even partial fitting of the inside and outside edges to separate contours was unsucessful.

3. <u>Perturbation Technique</u>. Presently a point variation technique is being investigated. Essentially, this involves moving each shim point by a small amount and then calculating the effect at all other points. This results in a series of simultaneous linear equation of number and order equal to the number of shim points. This method should be exact, except for multipoint movement interactions. However, if the individual point correction is relatively small, this effect should be minimal. The major disadvantage of this method is the vast amount of computer time required for the calculation. The method is mathematically defined by:

$$\sum_i A_{ij} X_i = -E_j$$

A_{ij} = matrix of variable coefficients

$= \dfrac{E_j - E_\Delta}{\Delta}$

E_j = error at shim point j without shim variation

E_Δ = error at shim point j with a variation in shim point i equal to Δ

Δ = the distance increment of variation

X_i = the distance variation of point i which will reduce the total shim error to zero.

The solution of this system of linear equations is applied to the contour as follows:

$$D'(i) = D(i) + X_i$$

where X_i is the solution at point i. The corrected contour is then coded into the relaxation program.

The results of this approach are very promising, however, a major obstacle to be overcome is the size of X_i. Mathematically, the value of X_i is unlimited and varies over that range. However, the shim contour is limited by its physical dimensions and cannot accommodate point movements over several inches. A possible solution to this problem is to limit the range of values permitted X_i and then minimize the contour error instead of attempting to eliminate it.

The final shim contour coordinates given in Table E were determined by shifting only a few points at a time during the iteration process. While it was necessary to continuously readjust the interior field to compensate for the few point variations performed at the outer edges, the final field errors listed in table F for this contour are minimal. Further reduction was attempted, but calculations indicated the result of reducing the outermost field errors more would be an increased error in the inside field. Finally, as an overall check of the calculational technique, a 0.1 inch grid mesh model was developed to compare with the results obtained from the 0.2 inch model.

This fine mesh grid was introduced over the inside edge of the larger mesh model. It extended from 6 to 26 inches as shown in Fig. 19. Boundary values were taken from the large mesh program and linear interpolation used to generate the intermediate point values, except along the shim contour. Here, the intermediate values were determined by smoothing the contour shape or by taking values directly from a 0.1 inch infinite field calculation. The results of comparing the two models are given in table G. While the results are in good agreement, a need for a finer mesh calculation is indicated. The minimum mesh size is determined primarily by the amount of computer central processing time available for the calculation.

The alpha particle trajectory calculations discussed previously required approximately 0.5 seconds of central processing time on a CDC 6600 digital computer. Approximately 1000 trajectories were calculated and plotted for the optimum theoretical field calculation, or about 500 seconds total time. Each infinite field calculation required about 10 seconds to reach a convergence value of 1 x 10^{-6}. The 0.2 inch mesh model required 12 minutes per run or about 360 minutes total central processing time. The one 0.1 mesh program ran 45 minutes, and calculated only a 20 inch segment of the 0.2 by 0.2 inch calculation in a 0.1 by 0.1 inch mesh grid would require on the order of 100 hours of central processing time. Even transferring the program to the faster CDC 7600 machine would not bring the required calculation time to less than 10 hours. The choice of 0.2 inch mesh model was therefore consistent with the resources available to complete this investigation.

Tables C through G are abbreviated summaries of data generated by the computer calculations. They include only values for integers, even though data is available for 0.2 and 0.1 inch mesh points.

TABLE C

RPI 255° ANALYZER SHIM CONTOUR
INFINITE EQUIPOTENTIAL CALCULATION
(30.0 inch radius)

Radial Distance (inches)	Midplane to Shim Surface (inches)	Radial Distances (inches)	Midplane to Shim Surface (inches)
14.0	1.563705	31.0	2.033614
15.0	1.583408	32.0	2.067785
16.0	1.604401	33.0	2.102459
17.0	1.626607	34.0	2.137618
18.0	1.649965	35.0	2.173236
19.0	1.674407	36.0	2.209303
20.0	1.699878	37.0	2.245795
21.0	1.726318	38.0	2.282699
22.0	1.753677	39.0	2.319996
23.0	1.781903	40.0	2.357667
24.0	1.810947	41.0	2.395686
25.0	1.840763	42.0	2.434030
26.0	1.871311	42.8	2.464913
27.0	1.902546	44.0	2.511533
28.0	1.934436	45.0	2.550593
29.0	1.966940	46.0	2.589765
30.0	2.000000		

TABLE D

COMPARISON OF POTENTIAL RELAXATION CALCULATION WITH OPTIMUM FIELD SHAPE
(30.0 inch radius)

Radial Distance (inches)	Percentage Difference	Radial Distance (inches)	Percentage Difference
16.0	-14.873687	31.0	0.000929
17.0	-3.010685	32.0	0.001311
18.0	-0.475847	33.0	0.001438
19.0	-0.074085	34.0	0.001513
20.0	-0.012983	35.0	0.001565
21.0	-0.003465	36.0	0.001368
22.0	-0.001887	37.0	-0.000080
23.0	-0.001569	38.0	-0.006712
24.0	-0.001452	39.0	-0.033373
25.0	-0.001389	40.0	-0.134371
26.0	-0.001372	41.0	-0.501079
27.0	-0.001355	42.0	-1.760605
28.0	-0.001273	43.0	-5.610616
29.0	-0.000920	44.0	-14.625993
30.0	0.000000		

TABLE E

RPI 255° ANALYZER SHIM CONTOUR
FINAL SHIM CONTOUR CALCULATION
(27.8 INCH RADIUS)

Radial Distance (inches)	Midplane to Shim Surface (inches)	Radial Distance (inches)	Midplane to Shim Surface (inches)
16.0	2.0000	31.0	2.1183
17.0	1.5550	32.0	2.1565
18.0	1.6400	33.0	2.1952
19.0	1.7160	34.0	2.2344
20.0	1.7420	35.0	2.2742
21.0	1.7720	36.0	2.3143
22.0	1.8033	37.0	2.3549
23.0	1.8353	38.0	2.3960
24.0	1.8681	39.0	2.4374
25.0	1.9018	40.0	2.4810
26.0	1.9362	41.0	2.5040
27.0	1.9714	42.0	2.7350
28.0	2.0071	43.0	2.6000
29.0	2.0436	44.0	2.7500
30.0	2.0807		

TABLE F

COMPARISON OF FINAL CONTOUR FIELD CALCULATION WITH OPTIMUM FIELD SHAPE

Radial Distance (inches)	Percentage Difference
16.0	-13.961974
17.0	-0.441270
18.0	-0.009863
19.0	-0.006222
20.0	-0.001510
21.0	0.003880
22.0	0.000490
23.0	-0.000922
24.0	-0.001203
25.0	-0.001223
26.0	-0.001130
27.0	-0.000782
28.0	0.000207
29.0	0.000969
30.0	0.001253
31.0	0.001388
32.0	0.001555
33.0	0.001830
34.0	0.002244
35.0	0.002718
36.0	0.003236
37.0	0.002795
38.0	-0.000361
39.0	-0.004464
40.0	0.005789
41.0	-0.000689
42.0	0.021716
43.0	-0.797557
44.0	-8.317033

Table G

0.1 Inch Mesh Check Calculation

Radial Distance (inches)	Midplane to Shim Surface (inches)	Percentage Difference
16.0	2.000000	-12.660316
16.5	1.500000	-3.790008
17.0	1.555000	-0.064198
17.5	1.870000	0.344968
18.0	1.640000	0.162830
18.5	1.696000	0.092107
19.0	1.716000	0.039396
19.5	1.727000	0.011949
20.0	1.742000	0.007244
20.5	1.756500	0.007198
21.0	1.772000	0.005498
21.5	1.787644	0.002993
22.0	1.803307	0.001149
22.5	1.819198	0.000199
23.0	1.835313	-0.000108
23.5	1.851640	0.000079
24.0	1.868174	0.000903
24.5	1.884913	0.002996
25.0	1.901846	0.008011
25.5	1.918969	0.019460
26.0	1.936275	0.042748

II. THE DETECTION OF SINGLE IONS BY REVERSE BIAS P-N JUNCTIONS

In experiments as early as 1961(12)the principal investigator reported on the potential advantages of using solid state devices for detecting a beam of ions. At that time, however, it was not possible to detect single charged particles. Subsequently(13,14), additional efforts were undertaken to improve circuitry, detectors, and minimize corona with the result that a one-to-one correspondence has been established between the arrival of single ions and output pulses that can be registered in a scaler.

The basic theory of a solid state detector shows that a "depletion layer" can be made to function as an ionization region for electron-hole pairs.(15)

The distance to which the depletion layer penetrates into each region of the crystal will be determined by a solution of the current continuity equation together with Poisson's equation. For the p-type region this gives

$$\frac{\partial^2 V}{\partial x^2} = \frac{4\pi e}{x} (N_A + n - p)$$

where N_A is the acceptor impurity concentration, n and p are again the local electron and hole densities and z is the dielectric constant of the crystal.

An exact solution of these equations is difficult but it is possible to learn a great deal about the junction using a rather drastic approximation, namely that throughout the depletion layer n and p are small compared with N_A. Poisson's equation then reduces to

$$\frac{\partial^2 V}{\partial x^2} = \frac{4\pi e}{x} N_A$$

Successive integrations give

$$\frac{\partial V}{\partial x} = \frac{4\pi e N_A}{x} (x - x_p)$$

and
$$V = \frac{4\pi e N_A}{x} (x^2 - 2xx_p) + V_o$$

x_p being the end of the depletion layer where $N_A + n - p = 0$ (on this model the depletion layer ends abruptly) and V_o is the potential at the junction interface, $x = 0$.

When $x = x_p, V - V_o = V_p$, the potential difference across the p-type region,

$$\therefore \quad x_p^{\,2} = \frac{V_p \varkappa}{2\pi N_A e}$$

also the extension into the n-type region is

$$x_n^{\,2} = \frac{V_n \varkappa}{2\pi N_D e}$$

The excess charge in the n-type region is equal and opposite to that in the p-type region, for the field is confined to the depletion layer in this approximation. Hence,

$$x_p N_A = x_n N_D$$

The depletion layer penetrates the two regions in the inverse ratio of their ionized inpurity concentrations, or alternatively in the direct ratio of their resistivities measured away from the influence of the junction. The depletion layer exists almost entirely in the high-resistivity material and for p-type material the depletion layer width is approximately

$$x^2 = \frac{\kappa V}{2\pi e N_A}$$

and if all the acceptors are ionized, the resistivity of the material is

$$p = \frac{1}{N_A e \mu_p}$$

so that $x = \left(\frac{x\mu_p}{2\pi} \rho V\right)^{\frac{1}{2}}$

Similarly, for n-type material

$$x = \left(\frac{x\mu_n}{2\pi} \rho V\right)^{\frac{1}{2}}$$

In p-type silicon this gives approximately

$$x = 3.2 \times 10^{-5} (\rho V)^{\frac{1}{2}} \text{cm}$$

and for n-type

$$x = 5.3 \times 10^{-5} (\rho V)^{\frac{1}{2}} \text{cm}$$

where ρ is expressed in Ω cm and V in volts.

Basically, the depletion region of a junction acts as a solid state ionization chamber with one electron-hole pair produced for every 3.6 electron volts of energy deposited in the active region of the device. However, a major difficulty in the application of p-n junctions to direct heavy ion detection is the very short range of ions in solids (see Figure 21). As a result, the ion loses most of its energy in the dead layer or window of the detector and deposits very little in the active region. There are other disadvantages of using solid state detectors to monitor ion beams directly. First, for low energy heavy ions, much of the energy loss is due to non-ionizing, elastic or "nuclear" collisions. Secondly, high ion beam currents striking the detector cause degradation due to damage of the crystal structure, and unwanted impurity introduction.

Since a p-n junction is not efficient in detecting ions directly, an alternate method may be employed. In this technique, the ions strike a dynode ejecting one or more secondary electrons. Ion to electron conversion is commonly used for ion detection. A conversion electrode offers a good combination of high sensitivity and rapid response. For example, ion-electron converting surfaces, together with an electron multiplier, are routinely used in mass spectrometry at count rates of 10^6 counts per second. To increase the sensitivity of ion detection systems, a combination of ion energy and converter surface preparation are chosen to give an average electron yield

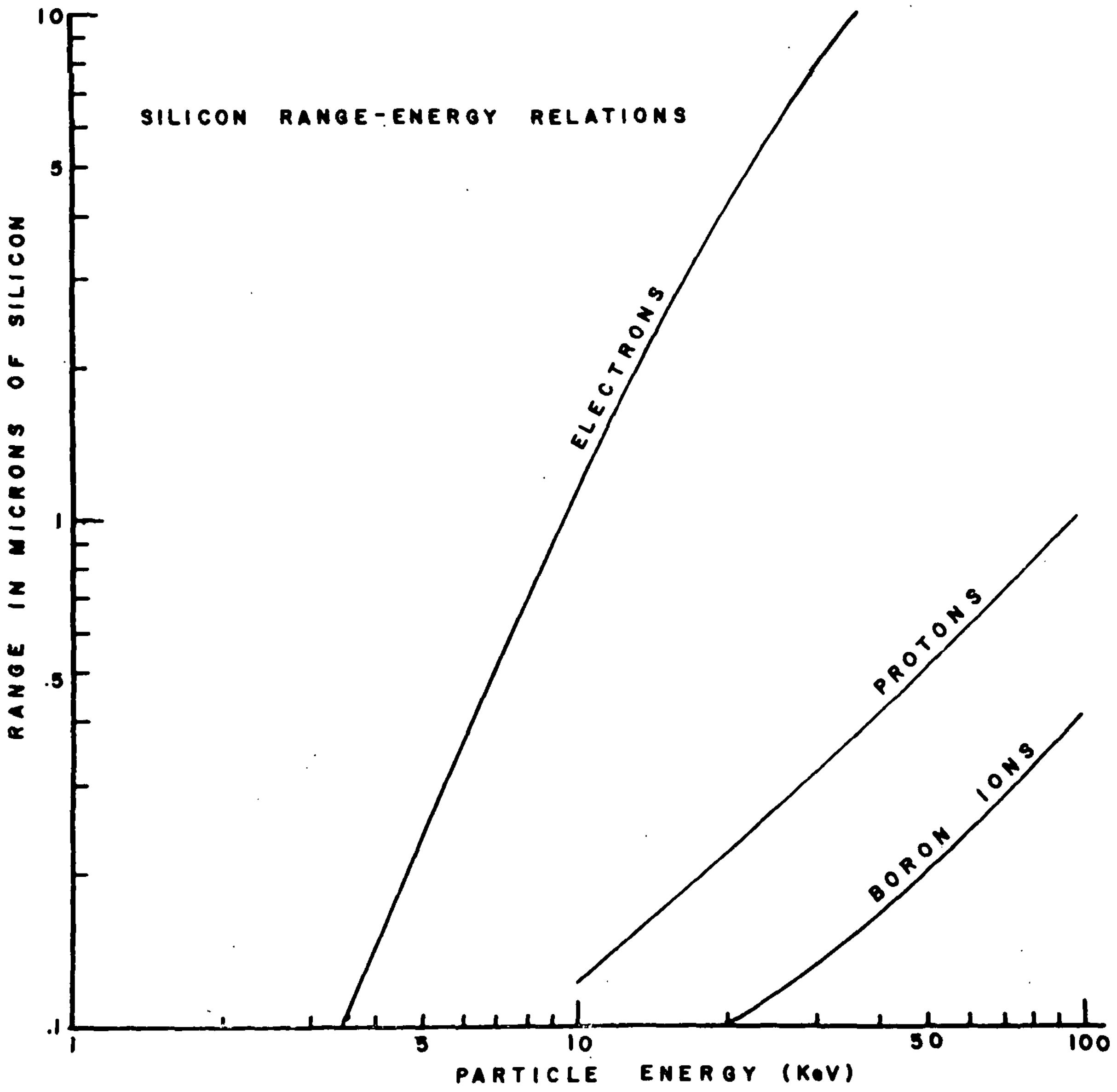
SILICON RANGE-ENERGY RELATIONS
RANGE IN MICRONS OF SILICON
10
5
1
.5
.1
1
5
10
50
100
PARTICLE ENERGY (KeV)
ELECTRONS
PROTONS
BORON IONS

Figure 21

of from 2 to 10 electrons per incident ion.

In combination with an ion to electron conversion surface or dynode, a single p-n junction has a number of attractive features as an ion detector for mass spectrometric applications. These are:

1. compactness
2. ease of mass fabrication
3. insensitivity to magnetic fields
4. high speed (10^7 to 10^9 pulses per second)*
5. extremely high efficiency in detection of electrons, with a good signal to noise ratio
6. ease of interfacing to data processing equipment (as opposed to photographic plates)
7. insensitivity to exposure to air or high vacuum
8. compatability with high vacuum systems
9. insensitivity to shock or vibration.

The most important characteristic of p-n junctions in this application are their compactness, allowing a large number of individual detectors to be used, and also the ability of the junctions to operate in the magnet's fringing field, in contrast to electron multipliers.

In present commercial instruments which focus a number of masses simultaneously in a plane, the

---

*Note: At present a limitation exists with respect to output circuitry.

most common readout is by means of photographic emulsions. It is informative to compare the advantages of p-n junctions to photographic plates in detail.

First, p-n junctions can provide a single output pulse for every ion that strikes the converter and produces secondary electrons. For a high yield surface, the discriminator can be set high enough to give both high efficiency and a high signal-to-noise ratio. In contrast, the best photographic emulsions require a minimum 10^4 ions at 10 KeV to produce a detectable line image. This fact makes it difficult to detect impurities at low levels as in analyzing semiconductor impurities.

Second, with present p-n junctions, it is possible to operate, with suitable electronics, at count rates from 1 count per second to 10^6 counts per second without an appreciable dead time correction although the energy resolution does suffer. Photographic plates, on the other hand, are inherently non-linear and require a great amount of precalibration. Multiple exposures are also generally required.

Third, while p-n junctions produce pulses which may be easily counted or readout for computer analysis, a photographic film produces data as an array of lines of varying capacity on strips of film or glass. These strips must be protected from exposure to light and developed, entailing a considerable time lag. The strip is then placed in a photodensitometer which transforms the data into graphic or digital form. Extensive corrections must also be applied for isotopic mass effects and film characteristics before qualitative results may be obtained. In contrast, a p-n junction system in conjunction with a high speed computer offers a possibility of real time display of the data being collected. (See Fig. 22).

Finally, a photographic detector requires a vacuum interlock to insert and remove the plates; also, after insertion the plates must outgas at high vacuum, thus increasing the time required for analysis. In contrast, the junction array, if properly fabricated, should not necessitate opening the vacuum chamber for long periods of time.

For a system employing p-n junctions to be efficient and practical, an important requirement is the fabrication of a stable, high yield secondary electron emitting surface that provides a high yield for <u>all</u> ion species. A single detector was used to examine a number of high yield surfaces as reported in the following section.

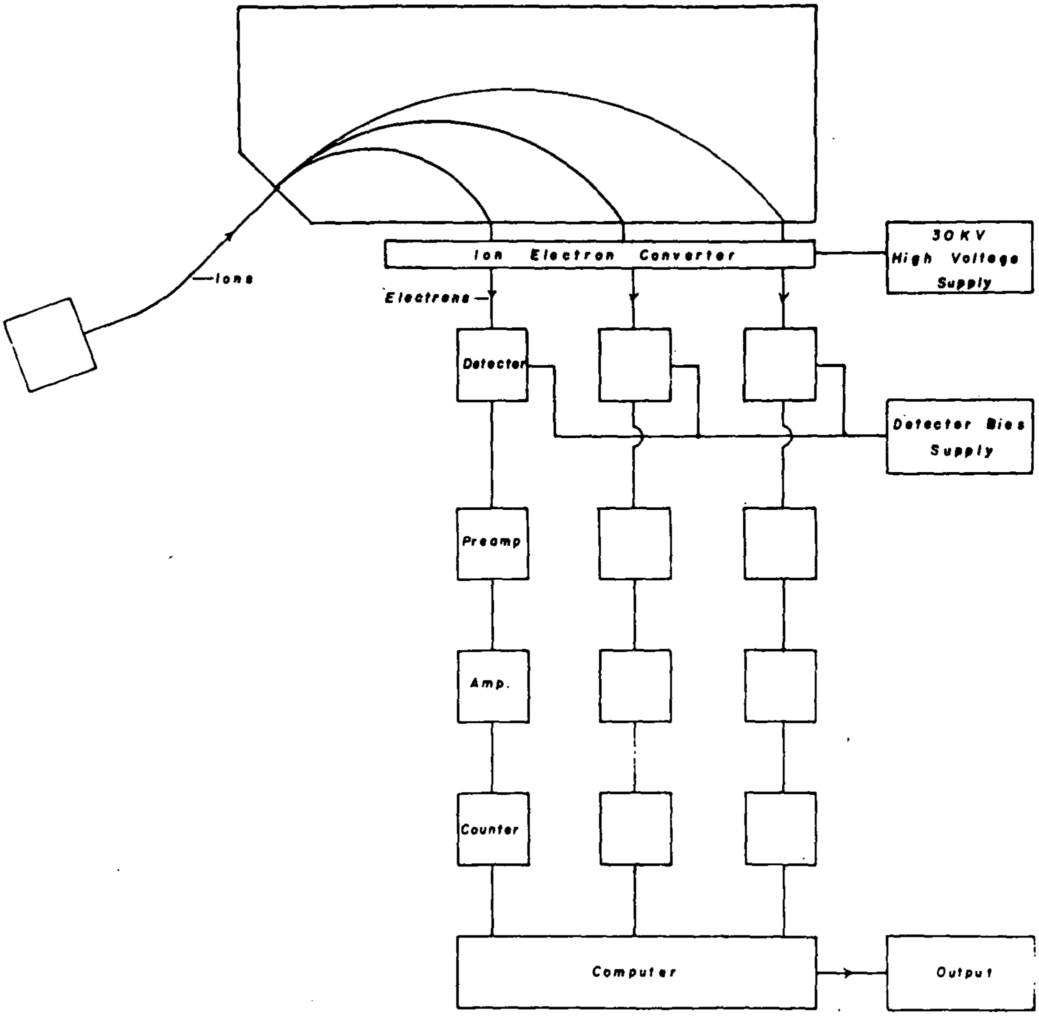

Figure 22
Schematic Diagram of
Real Time Display.

The p-n junction system was tested on the Cascade Ion Beam Analyzer which has been reported in the literature(16). Figure 23 is a schematic of the device and Fig. 24 is a photograph. Specific details of the manner in which the junctions were used in this mass spectrometer are outlined in the next section.

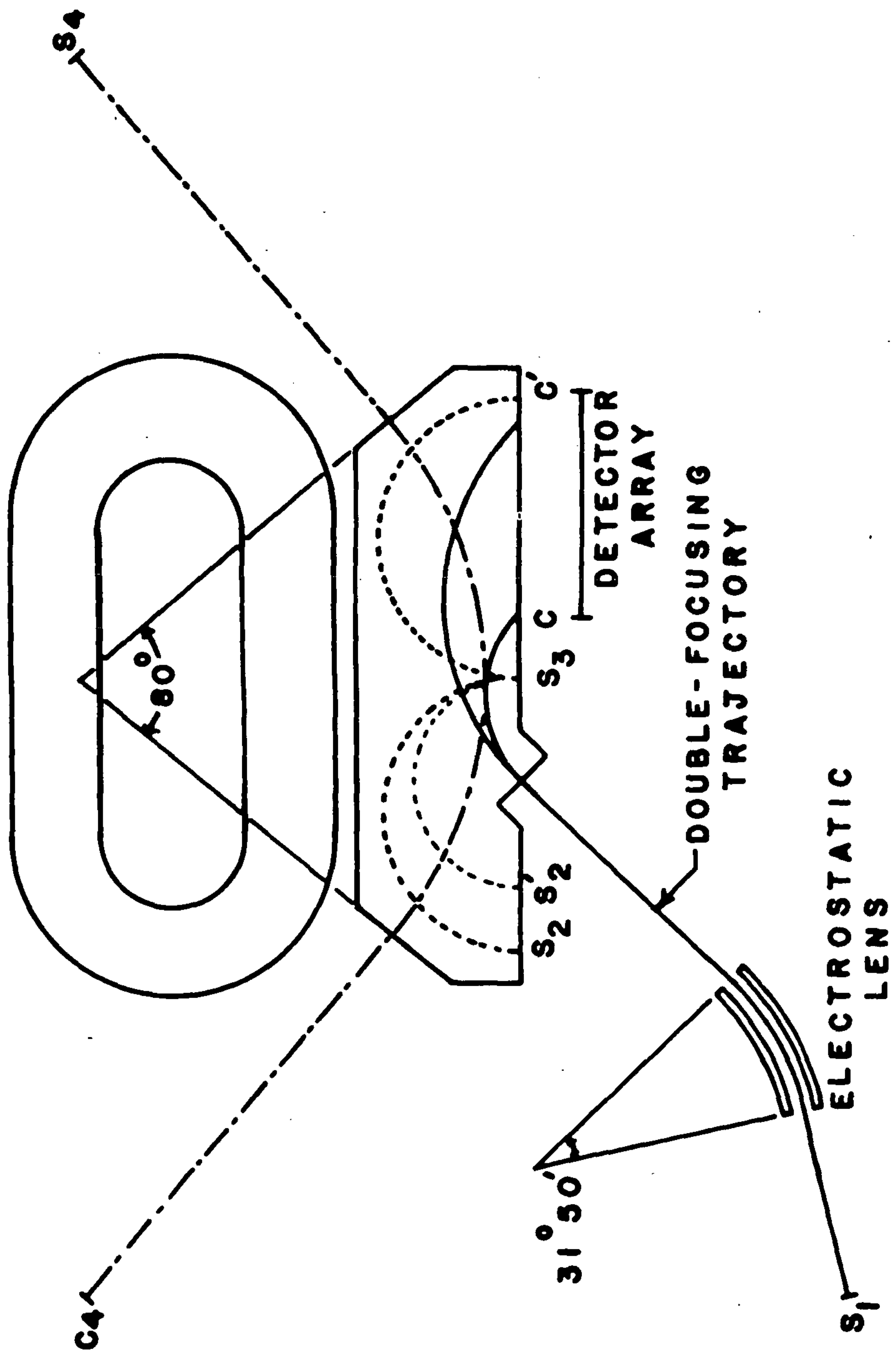

S_4
C_4
80°
C
C
S_3
S_2
S_2
DETECTOR ARRAY
DOUBLE-FOCUSING TRAJECTORY
ELECTROSTATIC LENS
31°50'
S_1

Figure 23

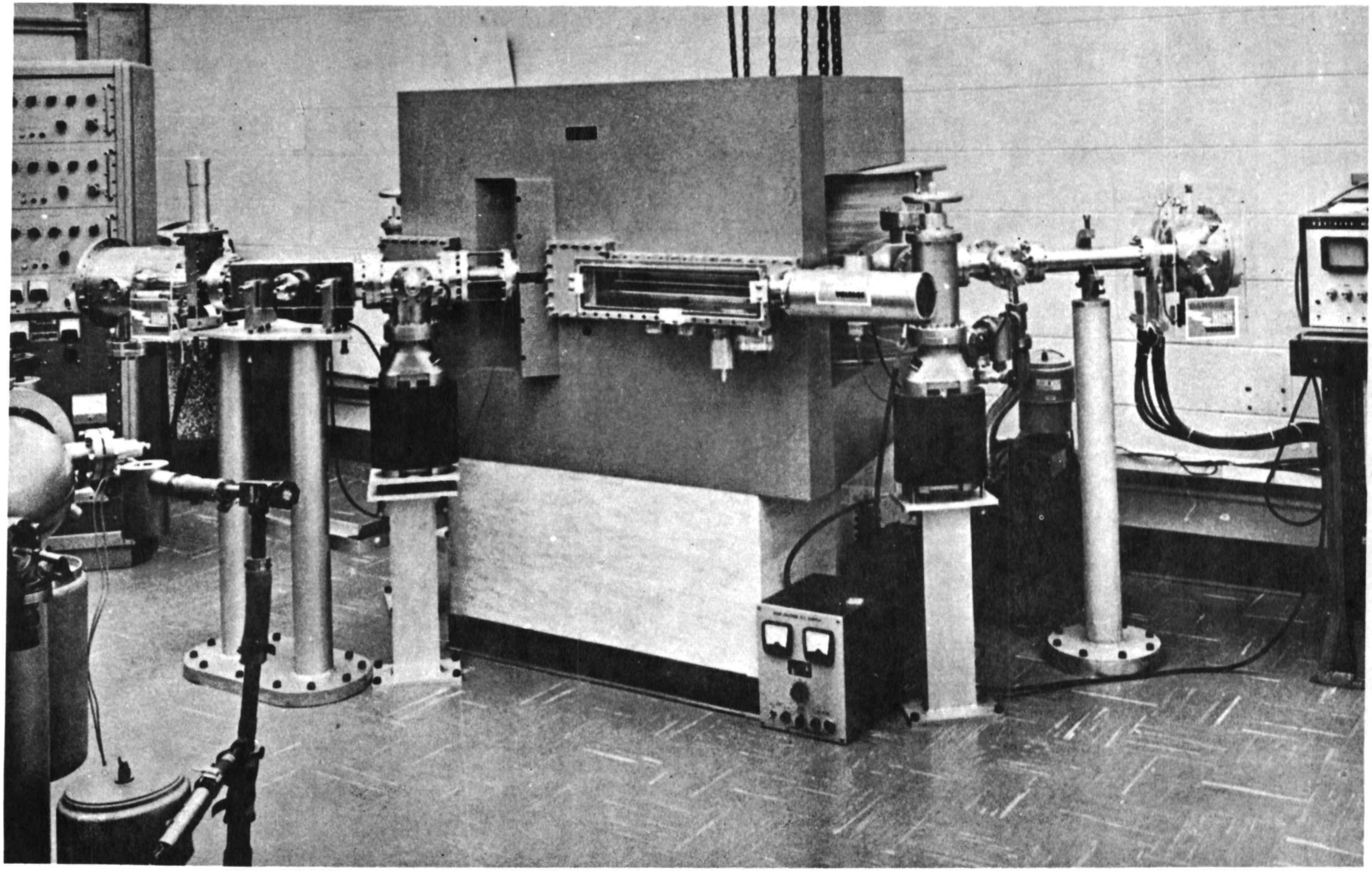

Figure 24 Cascade Mass Spectrometer

III. Secondary Electron Yield Measurements for Metallic Oxides.

As an integral part of the p-n junction detector effort, it was deemed appropriate to make definitive studies of several surfaces which might be sufficiently stable to act as a "converter" of ions to electrons. It is obvious that a high secondary electron yield is essential if a high signal-to-noise ratio is to be achieved in any solid state detector scheme. The following paragraphs (substantially following the dissertation by John D. Stein) suggest that our research effort has indeed been successful, and that future work is needed only to complete a practical system utilizing a large array of solid state detectors. All experiments were carried out using the Cascade Ion Beam Analyzer,(16) shown in the previous section.

In the detector region, the mass analyzed ions strike the target which is held at a negative potential of 10 to 30 kv (see Fig. 25). The voltage feedthrough and plate spacing, however, are designed to allow the use of accelerating voltages up to 50 kv.

The electron detectors used for the measurements reported are commercial reverse biased silicon surface barrier junctions with areas of 25 to 100 mm^2. The dead layer of these detectors were reported by the

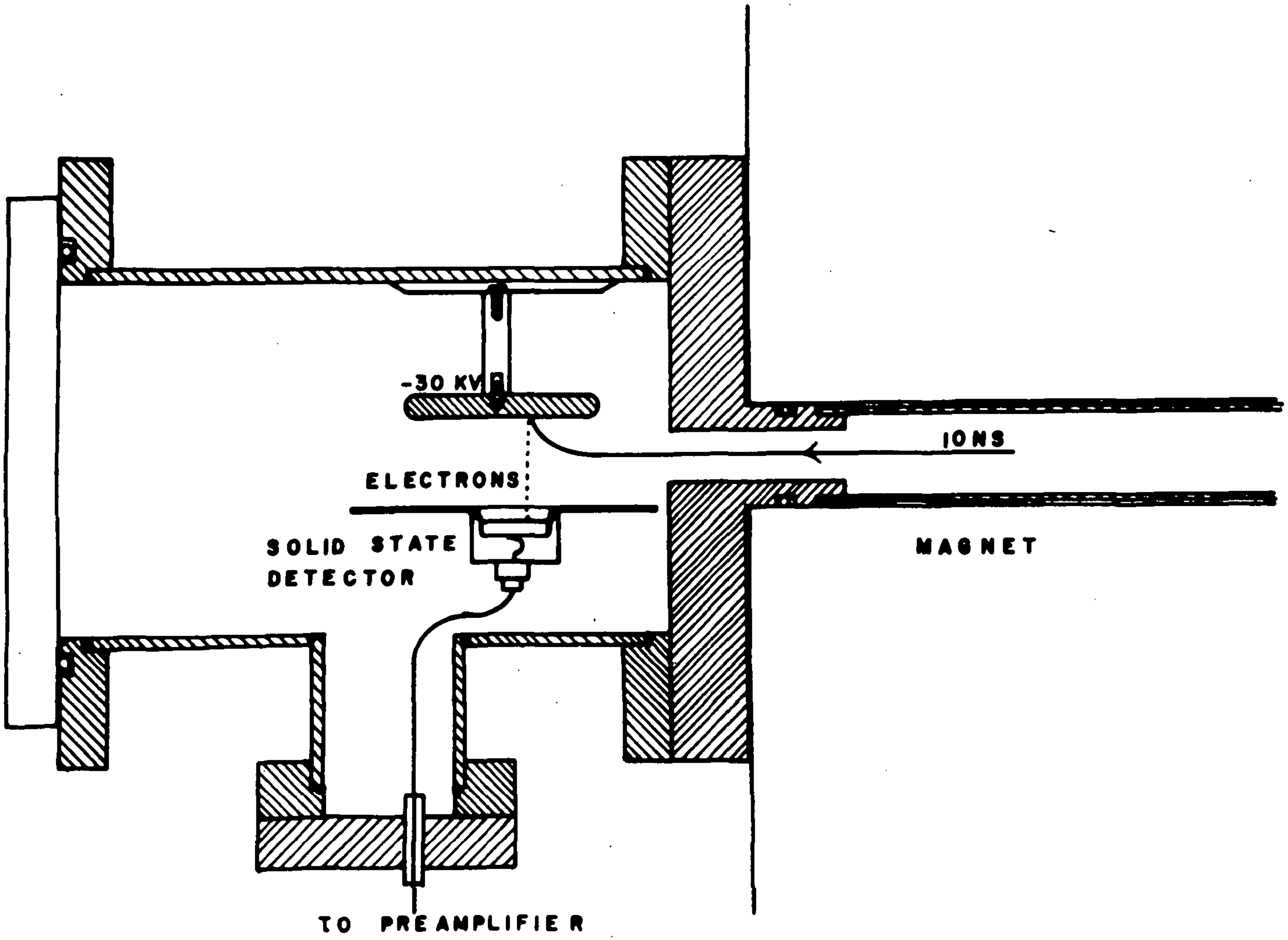
-30 KV
IONS
ELECTRONS
SOLID STATE
DETECTOR
MAGNET
TO PREAMPLIFIER

Figure 25

manufacturer to be equivalent to 40 mg/cm^2 of gold which is equivalent to approximately 200 angstroms. The output of the detector is fed into a low noise, charge-sensitive, field effect transistor preamplifier, and then into a main amplifier with pulse shaping, integration, and differentiation time constants of one microsecond. The output is then pulse height analyzed and displayed by a 1024 channel pulse height analyzer. A block diagram of the detector electronics is shown in Fig. 26. With the need for detecting low energy, one of the most important considerations is high energy resolution and low noise.

The surfaces investigated were prepared by a variety of techniques and were chosen because they were presumed to have a high electron yield and possible usefulness as an ion electron converter for ion beam detection.

The aluminum oxide surface was prepared by the anodic oxidation technique. First, the sample was polished to a mirror finish and then washed in alcohol and distilled water. The aluminum was anodized in a 3% by weight solution of ammonium citrate. With anodizing coefficient of 13.7 angstroms per volt, an oxide layer thickness of approximately 800 Å was produced with an applied voltage of 60 volts. After anodization the sample was again rinsed in distilled water.

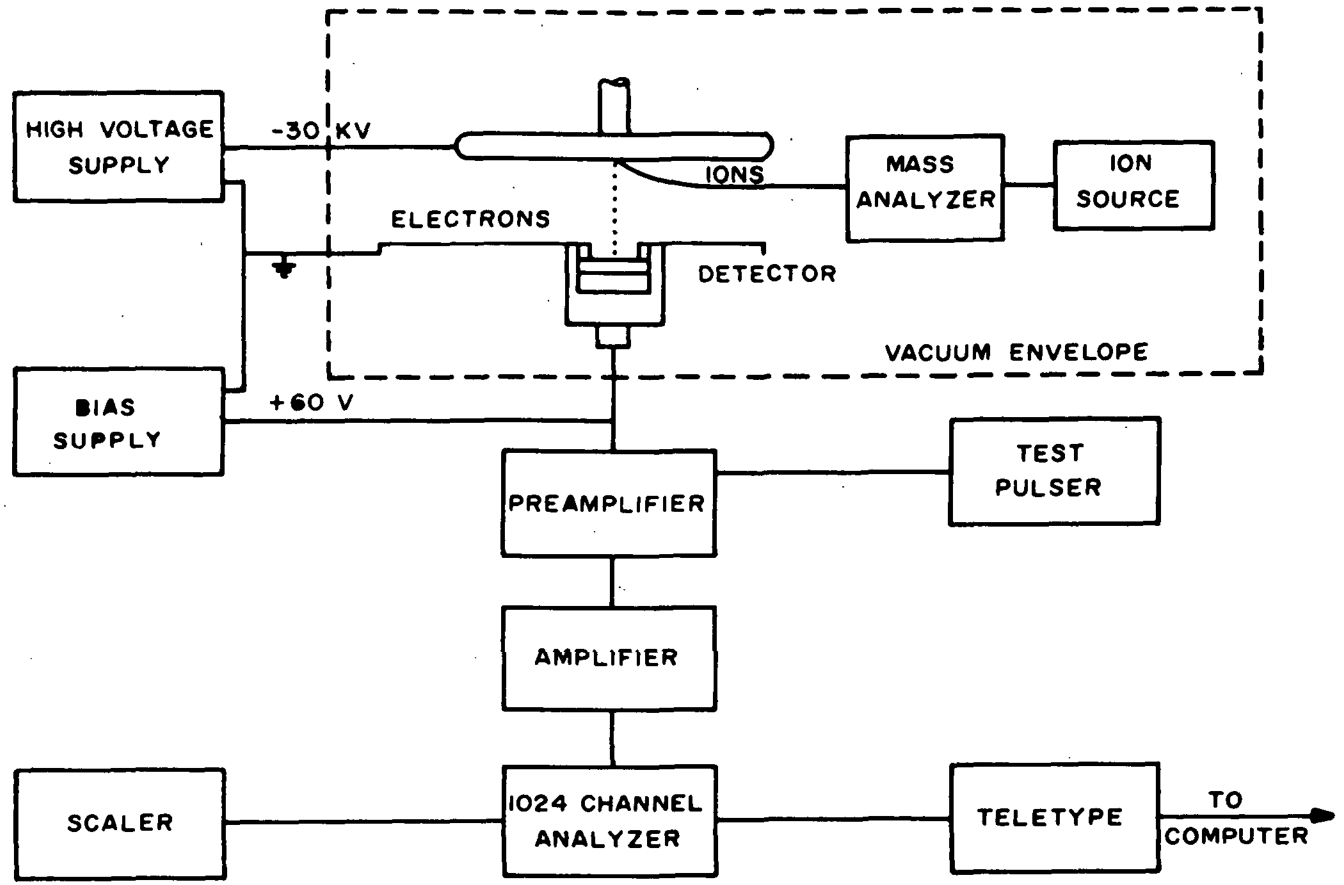

BLOCK DIAGRAM OF THE DETECTOR ELECTRONICS

Figure 26

The beryllium oxide surface was prepared using a 4% weight beryllium copper alloy treated according to a process developed by Michijima.(17) The process was as follows: The sample was first heated to 400°C in atmosphere for one hour and then slowly allowed to cool to room temperature. This treatment results in the formation of small inclusions of α phase alloy which contains 10 to 15% by weight beryllium. Electropolishing is then carried out in an 0.5 normal phosphoric acid solution. This polishing is carried out at room temperature with a current density of 0.1 ampere-per-square centimeter at an applied voltage of from 2 to 3 volts. The sample was then washed in deionized water and placed in the vacuum chamber.

For the titanium oxide, cold rolled 99% pure titanium foil was used with the naturally occurring oxide layer. The sample was merely washed in alcohol and then rinsed in deionized water and then placed in the vacuum.

A typical sample of the spectrum produced by the multichannel analyzer is shown in Fig. 27. This is a complete pulse height spectrum of the secondary electrons produced by a singly charged barium ions, with a total kinetic energy of 32.8 KeV, striking an aluminum oxide surface. This spectrum was taken with a 100 mm^2 Ortec surface barrier detector operated at a bias voltage of 105 volts and main amplifier single

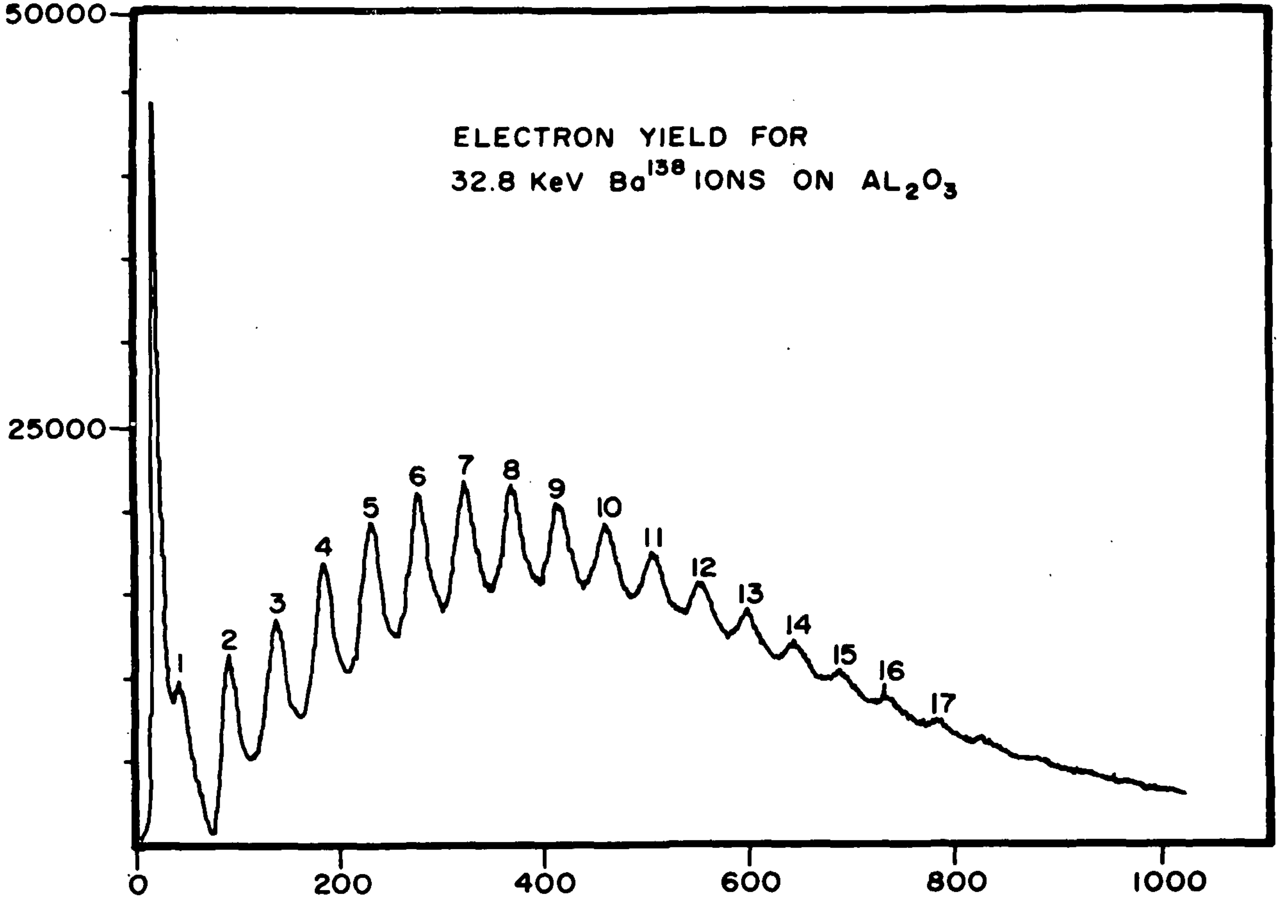

SECONDARY ELECTRON YIELD STATISTICS FOR ALUMINUM OXIDE BOMBARDED BY 32.8 KeV BARIUM IONS

Figure 27

integration and differentiation time constants of 1 microsecond. The electron accelerating voltage was -30 kv and the individual peaks correspond to groups containing one to seventeen electrons. From this spectrum, a number of important observations can be made.

The data, which is also available in digital form on punched tape, allows one to use computer plotting routines and computation techniques to determine the statistical distribution, as well as the mean yield, of the surface as a function of ion energy, mass, or charge state. This distribution is of particular importance in the design of electron and photo-multipliers which up to the present has only been determined indirectly by the study of pulse height spectra.

It should also be noted that while the separation of individual peaks can be clearly noted, it is poorer than would be expected from measurement of the system resolution, which was 10 - 12 KeV. Also, as the group of numbers increase, the resolution of the peaks become smaller. A possible explanation for this is the fact that there is a probability that an electron might be backscattered out of the detector before depositing all of its energy, thus, the more electrons scattered out of the detector, substantially poorer peak separation at higher groups will result.

The most probable secondary electron yield was measured for two surfaces. It should be emphasized that the yield reported corresponds to the peak of the electron distribution. The more commonly measured yield corresponds to the mean of the distribution and has been found in this investigation to be from 10 to 15% higher in value than the most probable yield.

The ion beam was produced by evaporating a solution containing nitrates and oxides of barium, strontium, lithium, and cesium, onto a rhenium filament. This filament was then placed in the Mattauch-Herzog trajectory where the material was ionized by resistance heating of the filament. The ions produced were then accelerated and then mass energy analyzed by a combination of magnetic and electrical fields and then focused on the target.

1. Secondary Electron Yield for Aluminum Oxide

The first surface analyzed was aluminum oxide, since this surface has been reported to have a high secondary yield under ion impact.(18) The results obtained for lithium 7, strontium 87, and barium 138, are shown in Fig.28. The results for cesium are shown in Fig. 29. These results are shown for an energy range of approximately 12 KeV to 40 KeV. The energy range was limited at the lower end by the resolution of the solid state detector for single

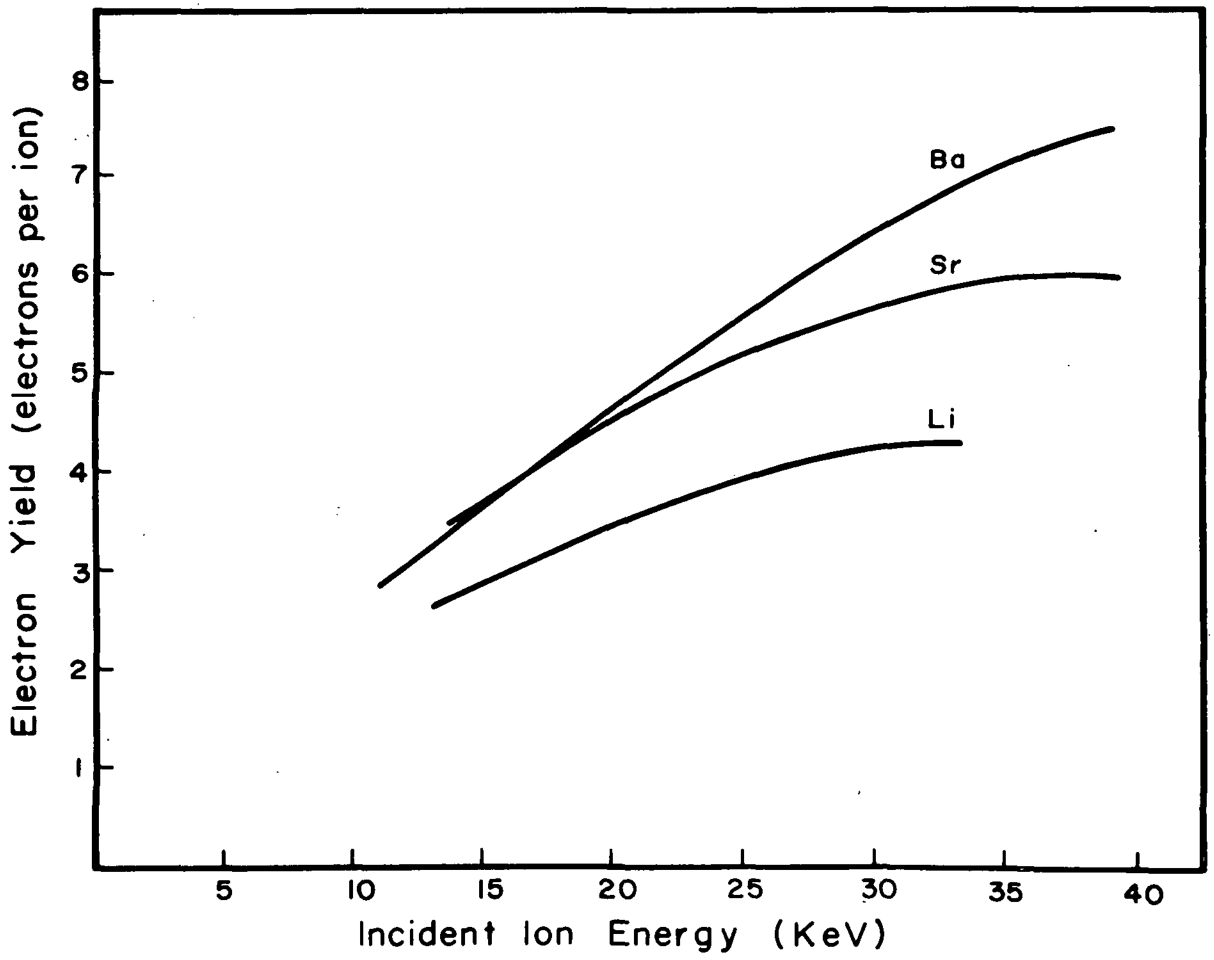
Electron Yield (electrons per ion)
8
7
6
5
4
3
2
1
Ba
Sr
Li
5
10
15
20
25
30
35
40
Incident Ion Energy (KeV)

Figure 28

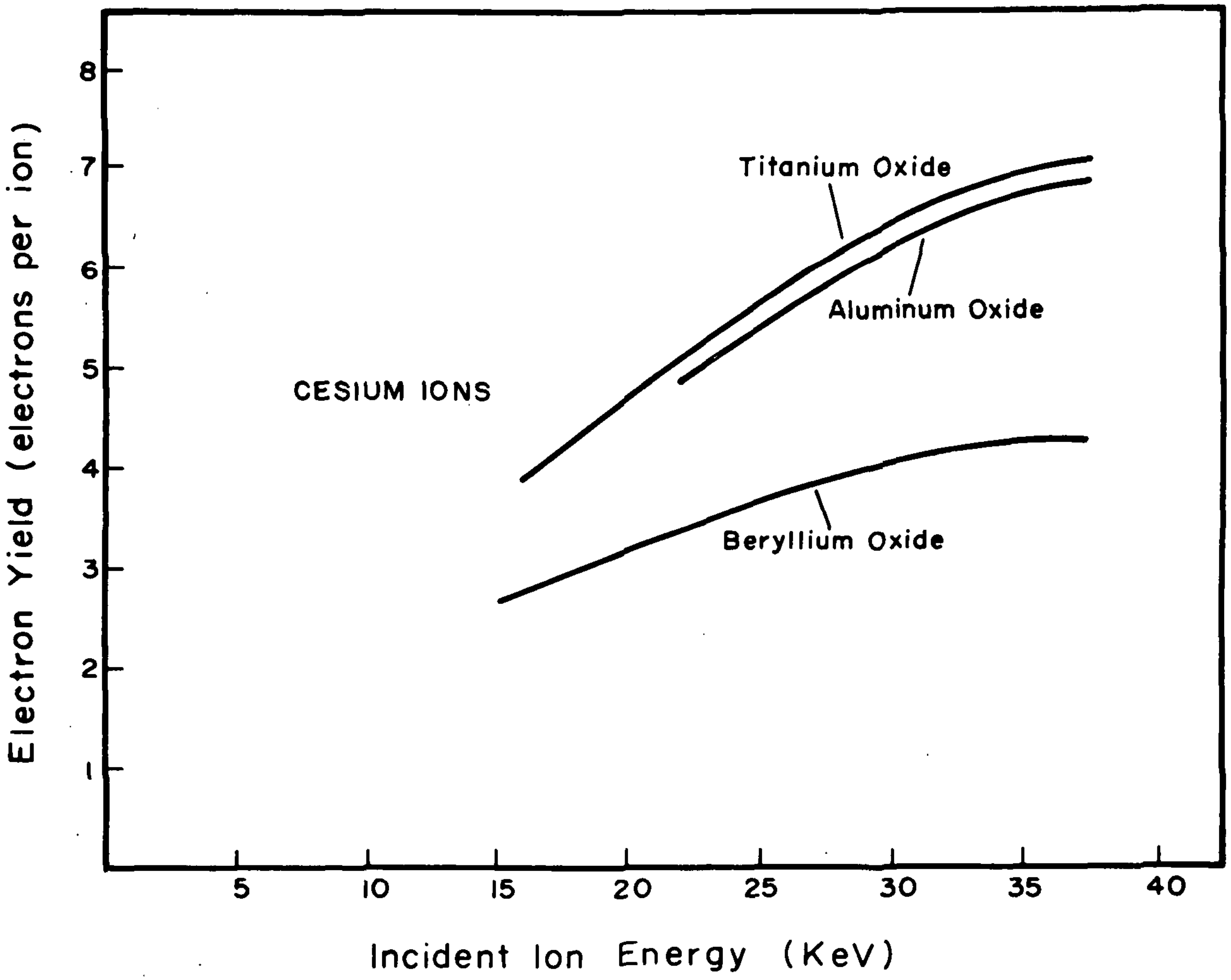
CESIUM IONS
Titanium Oxide
Aluminum Oxide
Beryllium Oxide
Electron Yield (electrons per ion)
8
7
6
5
4
3
2
1
5
10
15
20
25
30
35
40
Incident Ion Energy (KeV)

Figure 29

electrons. The upper energy limit corresponds to the maximum output voltage of the power supplies used.

2. Secondary Electron Yield for Titanium Oxide and Beryllium Oxide

A second surface studied was titanium oxide. The yield for cesium ions is compared with that obtained for the aluminum oxide surface and a beryllium oxide surface in Fig. 29. The reason that the beryllium oxide surface was not investigated further was that the yield was so low for cesium that it was not deemed suitable for use as an ion to electron converter.

Theoretical considerations which relate to this experimental work have been published elsewhere.(19) However, it is interesting to compare an experimental secondary electron yield with a Poissonian distribution. In comparing the distribution shown in Fig. 30, to a Poissonian distribution with the same mean, normalized to have the same area as under the experimental curve (see Fig. 27) it was noted that the experimental curve was much broader than a Poissonian distribution. Haussler(20) has reported a similar result for secondary electron produced by 300 eV electrons on a copper-beryllium alloy. A possible explanation is offered in a paper by Baldwin and Friedman.(21) In this paper it is theorized that a dynode surface may consist of small regions with varying secondary

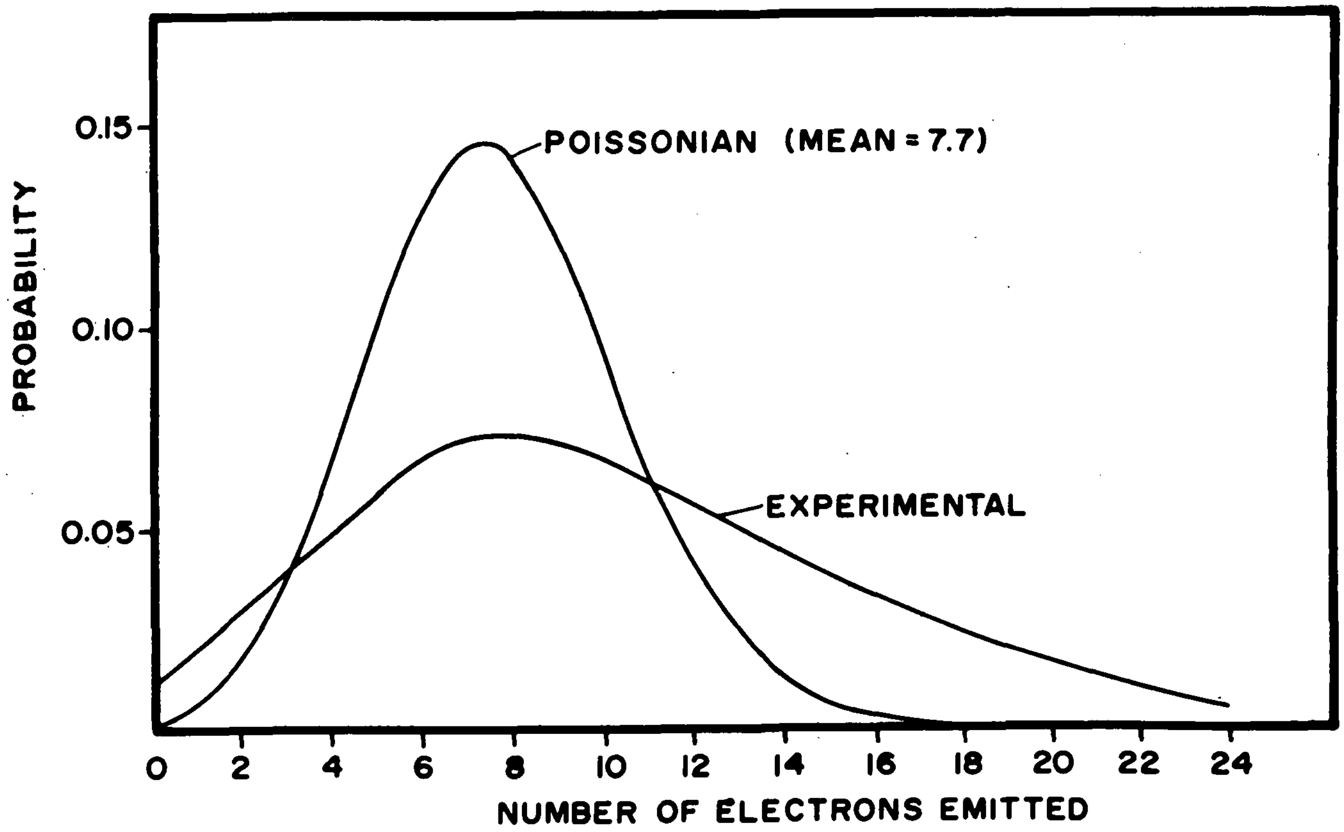

A COMPARISON OF THE EXPERIMENTAL SECONDARY YIELD
STATISTICS WITH A POISSONIAN DISTRIBUTION

Figure 30

emission coefficients. This inhomogeneous surface might lead to an output spectrum consisting of a superimposition of Poissonian distributions with varying means. An interesting test of this theory would be the investigation of a hgihly uniform surface such as a vacuum cleaved single crystal.

IV. ION SOURCES

A new technique was conceived and developed at this laboratory for thermally ionizing small quantities of the chemical elements on single-filaments, and for minimizing the production of spurious ions that give rise to errors in isotopic ratio measurements. The concept of this new (22) single-filament source is to utilize a diffusion mechanism in addition to thermal surface ionization, in order to obtain a higher ionization efficiency and a mass spectrum which is not obscured by impurities or superimposed molecular spectra. The sample, together with its isotopic spike, is encapsulated within an appropriate filament that is made of a refractory metal of high work function. The filament is then operated at a high temperature, which causes the sample atoms to diffuse to the exterior surface where a fraction becomes ionized by thermal ionization. This approach has proven to provide a number of advantages over conventional single-filament sources. The results and applications of this type of ion source have been published by W. G. Myers and F. A. White (Analytical Chemistry 41, 1861-1864 (1969).

Work at this laboratory on ion source development has also resulted in an additional technique for improving thermal ionization efficiencies. Although the method employed is primarily electrochemical in nature, it supplements the procedures used to obtain the desired characteristics of the diffusion-thermal ionization source. By establishing a thermal ionization filament as the cathode (-) in a slightly acidic solution, metallic elements in solution can be electro-deposited onto its surface. This concept is not original in itself, however the choice and order of anode (+) electrode material employed does provide desirable results.

The Analytical Mass Spectrometry Section of the National Bureau of Standards has established a procedure using a platinum - platinum cell to purify copper for subsequent mass spectrometric isotopic analysis. At this laboratory we have discovered that if a rhenium anode is used instead, the anode will dissociate quite rapidly when a potential ($>$10 volts) is applied, placing rhenium into the solution. Then if a platinum anode is employed, both the metallic sample and rhenium ions are attracted to and deposited on the filament cathode.

This technique has two important properties relating to the further development of thermal ionization filaments; e.g. (1) most metallic elements under analyses can be attracted to the ion source and trapped beneath a film of rhenium metal, thereby preventing prompt evaporation of atoms when the filament is heated, and (2) under certain conditions, the surface produced by this process can be made very porous and rough, with a large surface area. The resulting filament properties thus enhance the probability that neutral atoms will become ionized upon reaching the surface. The method also provides means of concentrating specific metallic elements from solution, without producing large deposits of unwanted material (i.e., Cl^-, NO_3^-,$SO_4^=$, etc.) on the filament surface.

This procedure has been applied to the analysis of a number of metallic elements at this laboratory. It is routinely used on samples which contain submicrogram quantities of the metal to be analyzed. To date, improved ion beams of copper, zinc, iron, silver, lead, nickel, uranium, potassium, cesium, rubidium and lithium have been observed on our mass spectrometers. For example, using an Li Cl solution containing a total quantity of 0.2 μg Li, the ionization efficiency was observed to improve by a factor of 20.

An alternative thermal-diffusion ionization concept is presented in Fig. 31. Here, the primary ion

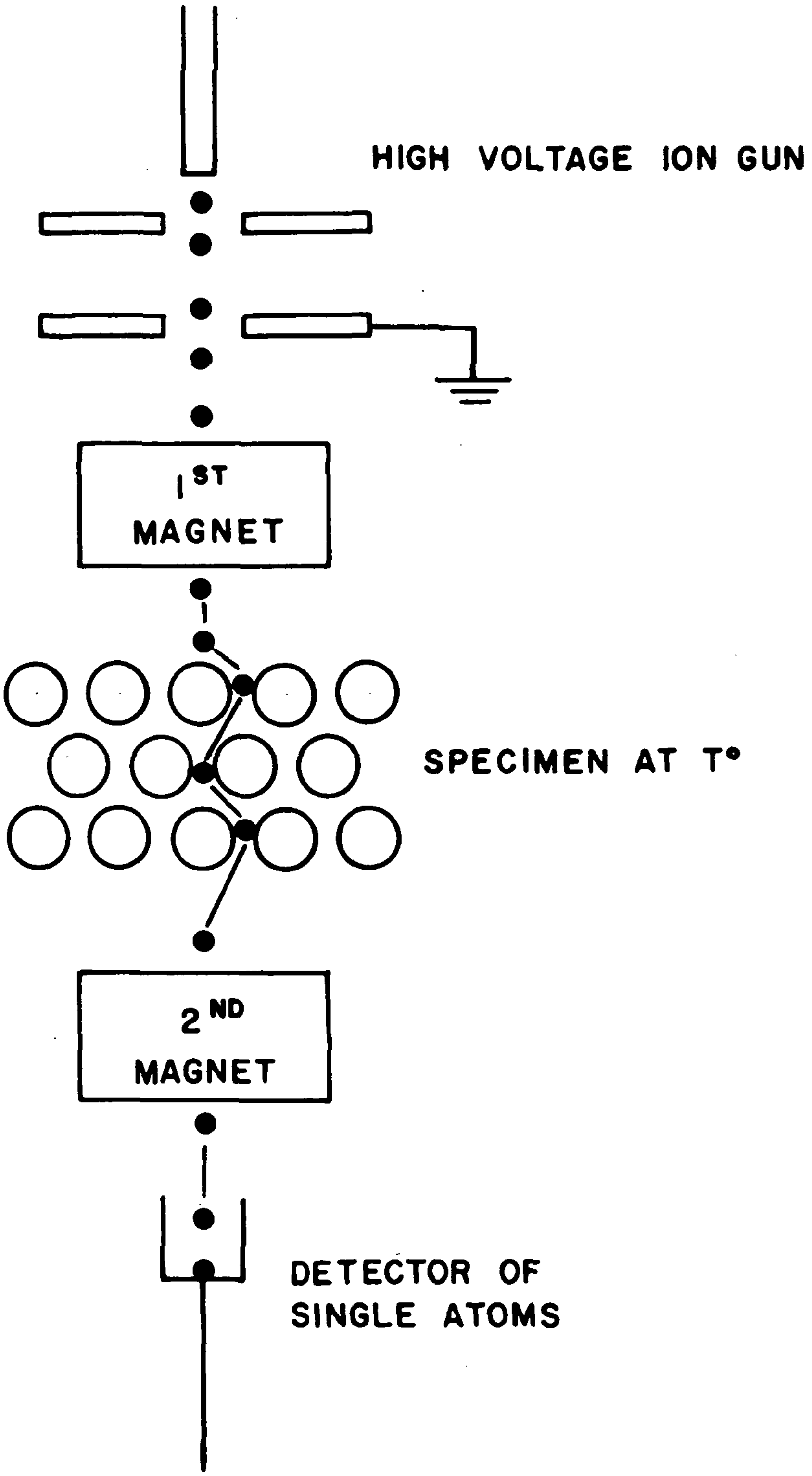
HIGH VOLTAGE ION GUN
1ST MAGNET
SPECIMEN AT T°
2ND MAGNET
DETECTOR OF SINGLE ATOMS

Figure 31

beam impinges upon a thin foil maintained at an elevated temperature. Ions are implanted and subsequently diffuse and become re-ionized, accelerated and pass through a second analyzing magnet. The scheme would greatly reduce ion beam intensity, but a pure atomic spectrum should be obtained.

An ion source has also been developed which has been very successful in supplying alkali metal atoms over extended periods of time. This source has been used to investigate the energy loss of ions traversing thin foils (see Fig. 47).

V ENVIRONMENTAL APPLICATIONS OF MASS SPECTROMETRY AND THERMAL IONIZATION SOURCES

We are including the results of two recent measurements because of nationwide interests in identifying the chemical composition of atmospheric particulates. Although such measurements were not specified as a technical obligation under this grant, we are pleased to present them as they demonstrate the very high sensitivity of mass spectrometry, and they point up the desirability of such future studies on a greatly expanded scale.

ASSAY OF COPPER IN RAINFALL

The primary sources of metallic pollutants and their rate of introduction into the atmosphere is generally known. The natural forces and meteorological processes regulating their removal, however, are not as well defined, receiving comparatively little attention to date. The high sensitivity of thermal ionization, mass spectrometry to metal analysis was applied at this laboratory to observe the dynamic "washout" of copper from the atmosphere.

Figure 32 shows the copper content of fractionally collected rain samples taken during a shower in the Troy, New York area, June 1968. The samples were collected in plastic containers and spiked with an

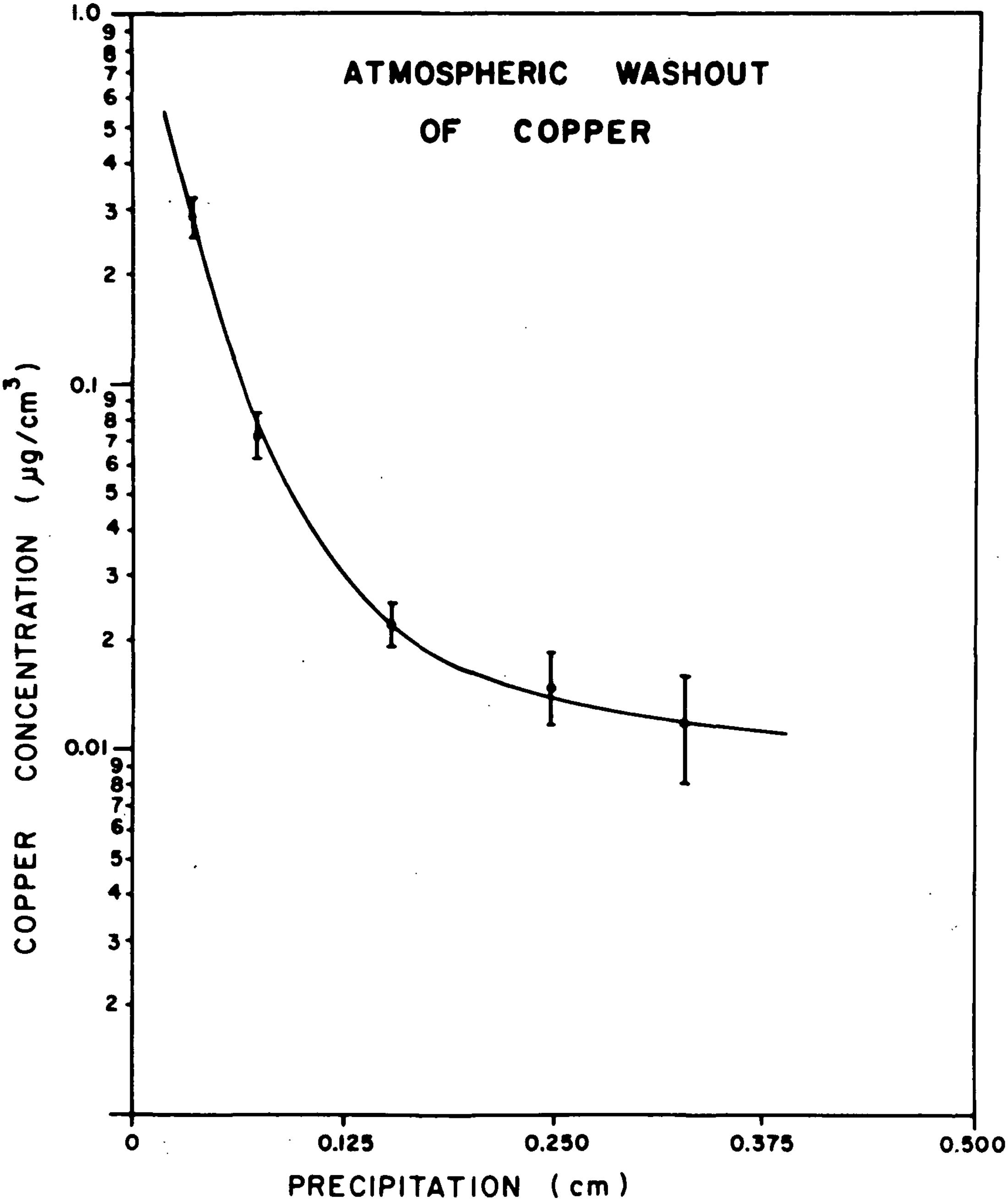
ATMOSPHERIC WASHOUT
OF COPPER
COPPER CONCENTRATION (µg/cm^3)
1.0
0.1
0.01
PRECIPITATION (cm)
0
0.125
0.250
0.375
0.500

Figure 32

isotopically enriched nitric acid mixture. The analysis was performed on dropsized (10 μl) portions of the precipitation whose total copper content amounted to only 1×10^{-10} gm in some cases. The results shown in Fig. 32 were found to agree with theoretical models describing contaminant washout mechanisms. Graphical analysis of this data indicated the copper concentration in the precipitation follows the expression:

$$C(\mu g\ Cu/cm^3) = \frac{0.00275}{h}(1 - e^{-36.6h}) + \frac{0.0044}{h}(1-e^{-1.66h})$$

where h is in terms of centimeters of rainfall. By estimating other parameters of each storm, one can calculate the approximate copper content in ambient air both prior to and during the period of precipitation. Such information, along with direct air sample analyses allows the determination of atmospheric self-cleansing rates, and provides a better understanding of the complex mechanisms which establish contaminant concentration levels.

ENVIRONMENTAL MONITORING OF URANIUM

Also of current interest at this laboratory is the analysis of trace elements in urban air environments. Although the National Air Surveillance Network is monitoring urban atmospheres for some 15 odd metals, the instrumental methods of analysis presently applied to these samples are not sensitive enough to detect those metals which exist in trace concentrations. One example of the sensitivity and value of mass spectrometric analysis to environmental surveillance has been demonstrated on air samples taken in June 1969 from downtown Albany, New York. These samples were analyzed for their uranium content by employing the isotopic dilution procedure, using thermal ionization source techniques(22) developed by the authors. The results of this particular analysis are listed in Table 1 along with the concentrations of a few other metals present in the atmospheres of U. S. cities as a means of comparison.

IMPORTANCE OF ISOTOPIC ASSAYS IN FUTURE STUDIES

We believe that within the near future, not only will the elemental "finger-print" of environmental systems be recorded and monitored, but also their isotopic composition. In addition to being ideal for biological and environmental tracer studies, stable isotopic analyses offers a very sensitive means of observing human induced changes to natural environmental systems. A change in the isotopic abundance of an element will not only provide a measure of the amount of contamination introduced, but possibly its source. This technique has already been demonstrated

METAL CONCENTRATIONS IN THE ATMOSPHERES OF U. S. CITIES, 1960 - 1965[a]

POLLUTANT	CONCENTRATIONS $\mu g/m^3$	
	AVERAGE	MAXIMUM
IRON	1.58	22.00
LEAD	0.79	8.60
ZINC	0.67	58.00
COPPER	0.09	10.00
TIN	0.04	1.10
URANIUM	0.000018[b]	—

[a] U. S. Dept. Health, Education & Welfare

[b] This laboratory, sample site - Albany, N. Y., 1969

Table 1.

with the element lead(23,24)

Those interested in monitoring the impact of the nuclear industry on the environment will find the rare earth elements particularly useful for such purposes. The rare earth elements are attractive here because of their relatively low abundance in nature and rather high yield from nuclear fission. Based upon a predicted power output of 10^6 MW (T) in the year 1990 from nuclear plants, the yearly production of stable fission product elements therefrom would be 110,000, 58,000, 28,000 and 24,000 pounds of neodynium, cerium, lanthanum and samarium, respectively. The introduction of a small portion of this material into the environment would be detectable due both to the low levels (i.e., 5×10^{-10} g Sm/l in seawater) presently existing there and the characteristic isotopic abundance difference between natural and fission product elements. As an example, the isotopic ratio of Ce^{140}/Ce^{142} in nature is 7.98, whereas that from the fission of uranium 235 is about 0.015. Given a body of water containing 12×10^{-10} g Ce/l (seawater), the input of only a small quantity of fission product cerium will produce a noticeable change in the natural isotopic ratio. In the case of a river with a flow rate of 26,000 ft^3/sec (Hudson River at Albany), a nuclear power plant leaking only

6×10^{-6} g/sec into the river would produce an isotopic ratio change from 7.98 to 7.5 downstream even after complete mixing.

The need for establishing background concentrations and isotopic analyses of these and other ecosystems is apparent. It is here that mass spectrometry can provide a unique contribution to environmental studies.

VI. "STATIC" MASS SPECTROMETRY

One spectrometer project that was quite distinct from other technical studies relates to a "static" mass spectrometer. This work would appear to have special relevance to NASA programs relating to (1) the absolute calibration of the partial pressures of Xenon and Krypton (2) the use of "static" mass spectrometry generally for assaying gases at pressures of 10^{-10} Torr and (3) the "burn-up" measurement of nuclear fuel. With respect to this latter item, it will be recalled that for many years "fission track analysis" has been useful in determining trace amounts of uranium in geological and other samples. In this new spectrometric method one relates fissioned atoms to partial pressures of the noble gases, Xe and Kr, and by an examination of the isotopic spectra.

The distinction between a "dynamic" and a "static" mass spectrometer system is described briefly. In conventional gas analysis, the gaseous sample is typically allowed to enter the ionizing region of the mass spectrometer source from a suitable gas handling system through a variable leak valve. The ionizing volume of the electron bombardment source is made as small as possible to maximize the ionization of the sample compared to the residual gases in the spectrometer. Usually the pressure in this region is fairly high (10^{-5}-10^{-4} torr), consistent with space charge limiting effects, the sample size, and the vacuum required.

in the analyzer section of the spectrometer. For hydrocarbons or other gases where dissociation is a problem, the inlet lines and source region are usually temperature controlled to provide reproducible spectra. Due to isotopic fractionation effects through the variable leak, isotopic ratios for a given sample may need to be corrected in time, as preferential effusion of the lighter species depletes it in the sample reservoir. Once the gas enters the mass spectrometer, it is pumped away by the system's vacuum pumps. There is a continuous flow of gas sample.

Static mass spectrometry, on the other hand, requires the admission of one discrete sample of gas to the spectrometer enclosure with no pumping on the system thereafter. An ordinary electron bombardment source may be used; but it is customary to open the ionizing region to the spectrometer, as the sample is now one of the residual gases in the spectrometer enclosure.

The RPI Static Mass Spectrometer is shown in Fig.33. Figure 34 is the overall schematic diagram, and Fig.35 is the ion source for producing ionized atoms of the noble gases. The spectrometer consists of (1) a 6" radius of curvature magnetic analyzer (2) a bakeable analyzer tube with an electron bombardment type source (3) a special gas sample inlet system and (4) an electron multiplier detector that operates in the pulse-counting mode. A severe restriction for the multiplier is that it must be able to withstand the high temperature bake-out prerequisite to achieving an initial analyzer tube pressure of 10^{-10} torr.

The salient features of the burn-up experiment and the sub-

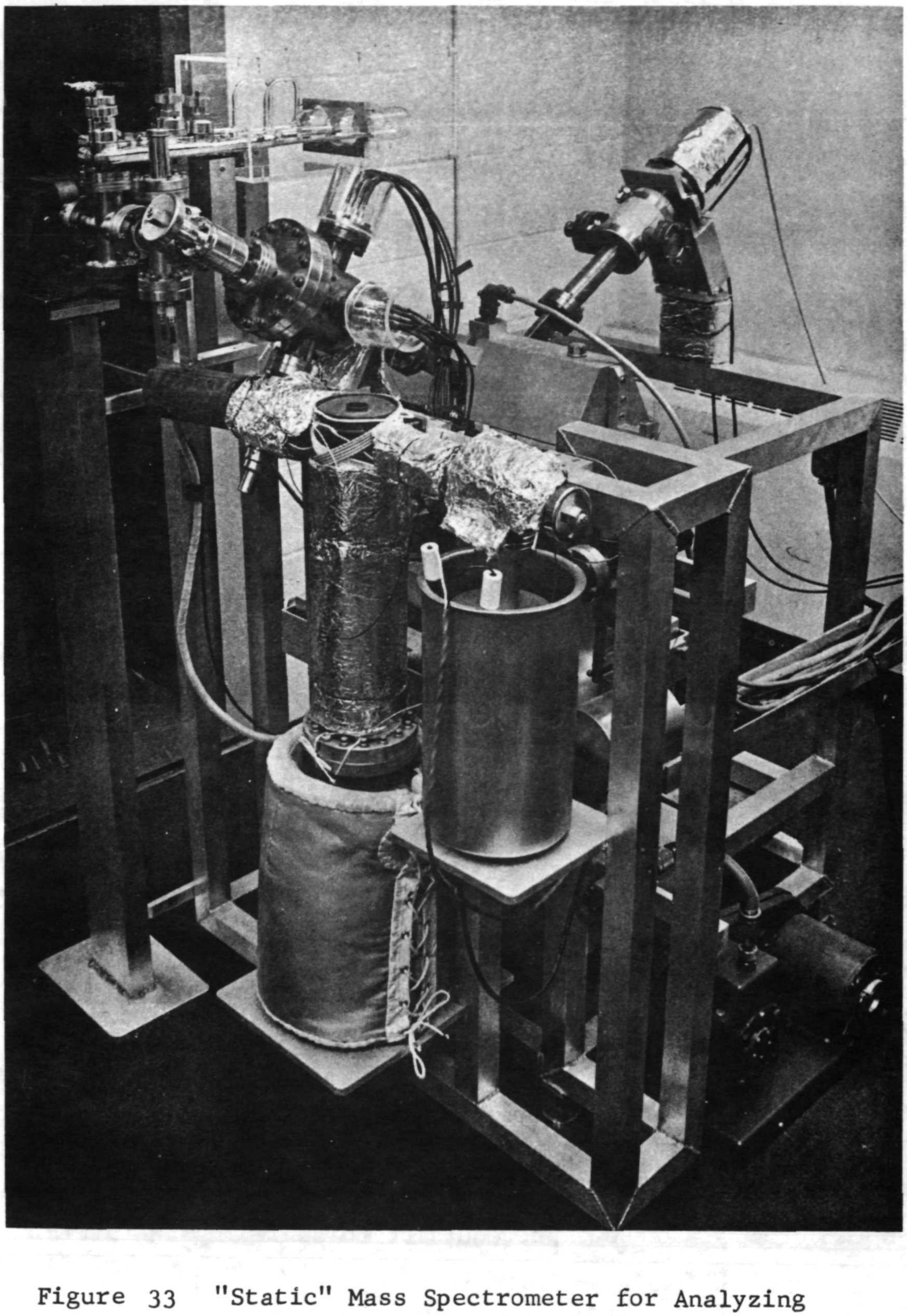

Figure 33 "Static" Mass Spectrometer for Analyzing Fission Product Gases

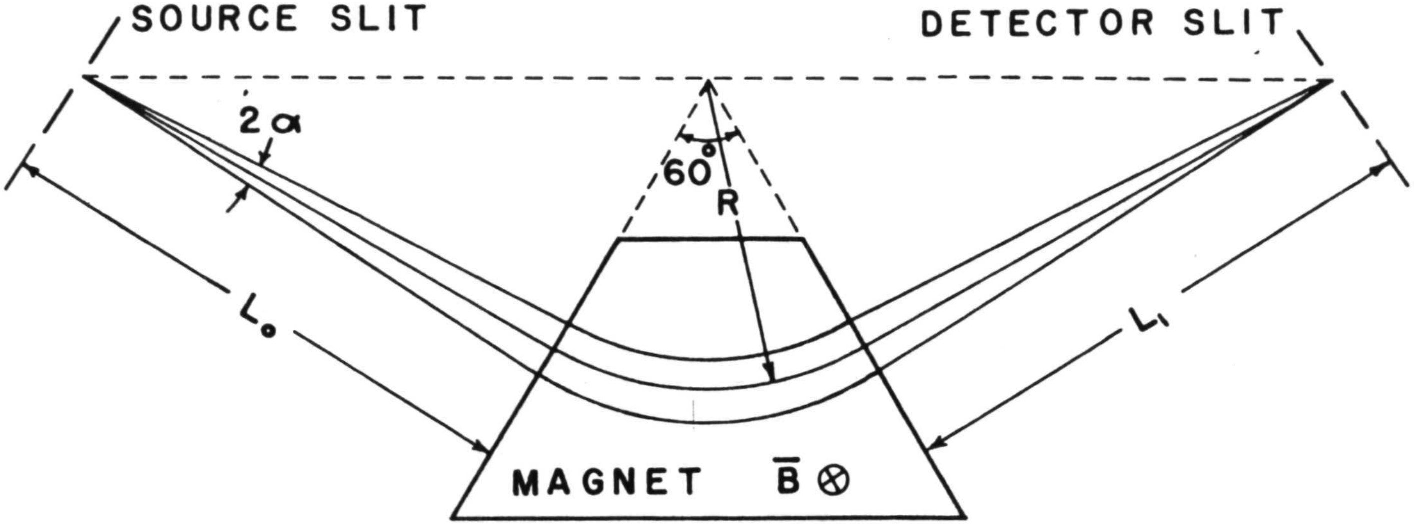

R = 6 INCHES

$L_0 = L_1 = R\sqrt{3}$

FIGURE 34 60° SECTOR MAGNET

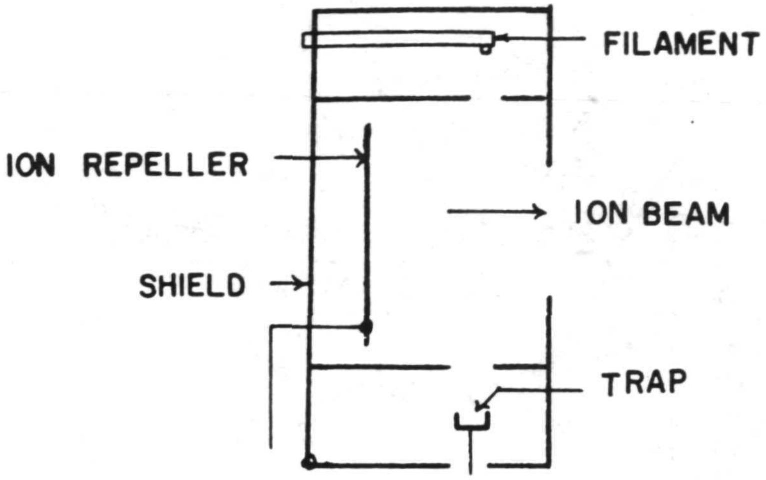

DETAILS OF IONIZATION VOLUME

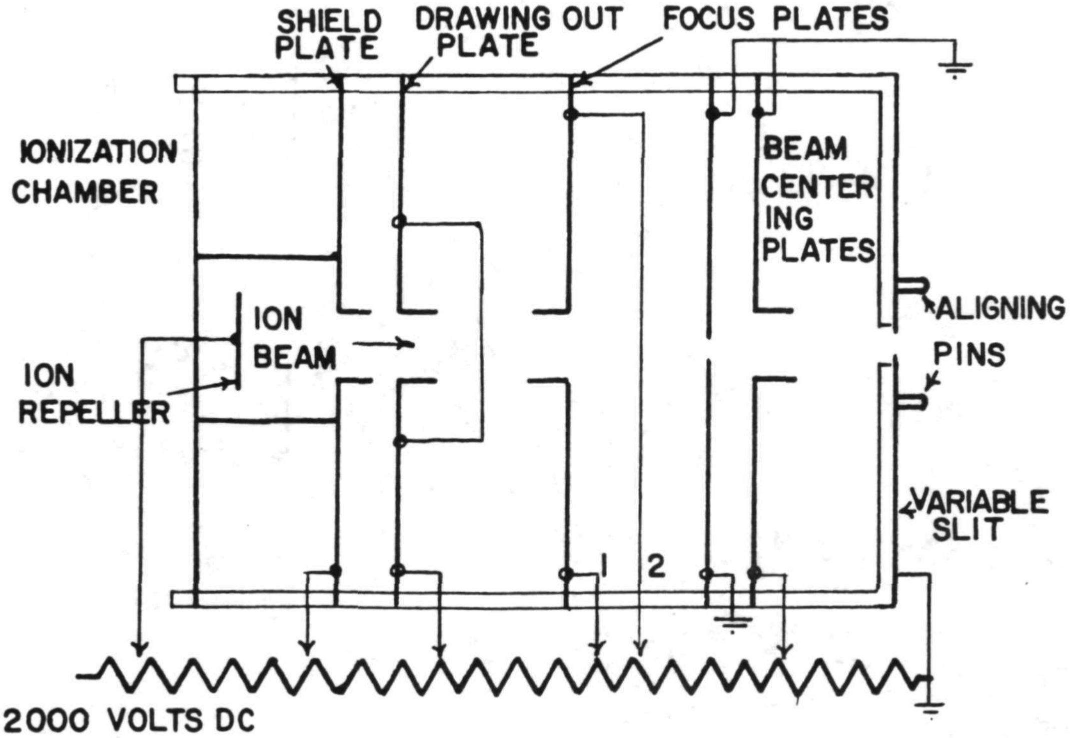

FIGUIRE 35 ION SOURCE SCHEMATIC

sequent assay of fission product gases will now be summarized:

1. Small samples (~1 μg) of U-235 were deposited on thin strips of high purity Al.
2. These strips were then "folded" so as to stop the fission products produced by neutron-induced fission. (The mean range for gross fission products has been measured in Al to be about 1.4×10^{-3} cm. (0.00055 in)
3. The foils were then irradiated in a well known and highly "thermal" neutron flux at an nvt of 4×10^{17} n/cm^2 or 0.02% U-235 fission burnup.
4. Upon irradiation, the fission products are assumed to be totally retained with the foils.
5. Subsequent to this irradiation, these foils were totally evaporated by a tungsten filament under static conditions <u>within</u> the mass spectrometer, thereby releasing all fission products including the noble gases Xe and Kr.
6. Ions were then produced by the electron bombardment source and isotopic spectra were obtained from the electron multiplier/data acquisition system.

The Xenon and Krypton isotopic ratios were monitored for periods up to 8 hours on total amounts of any Xe or Kr isotope of approximately 10^{10} atoms. Observed ion counting ratio were in the range of several thousand ions/sec for the major isotopes.

The nomograph of Fig. 36 gives the order of magnitude of the number of fissions to be expected from an initial sample of U-235 as a function of integral neutron flux (thermal). Table I gives

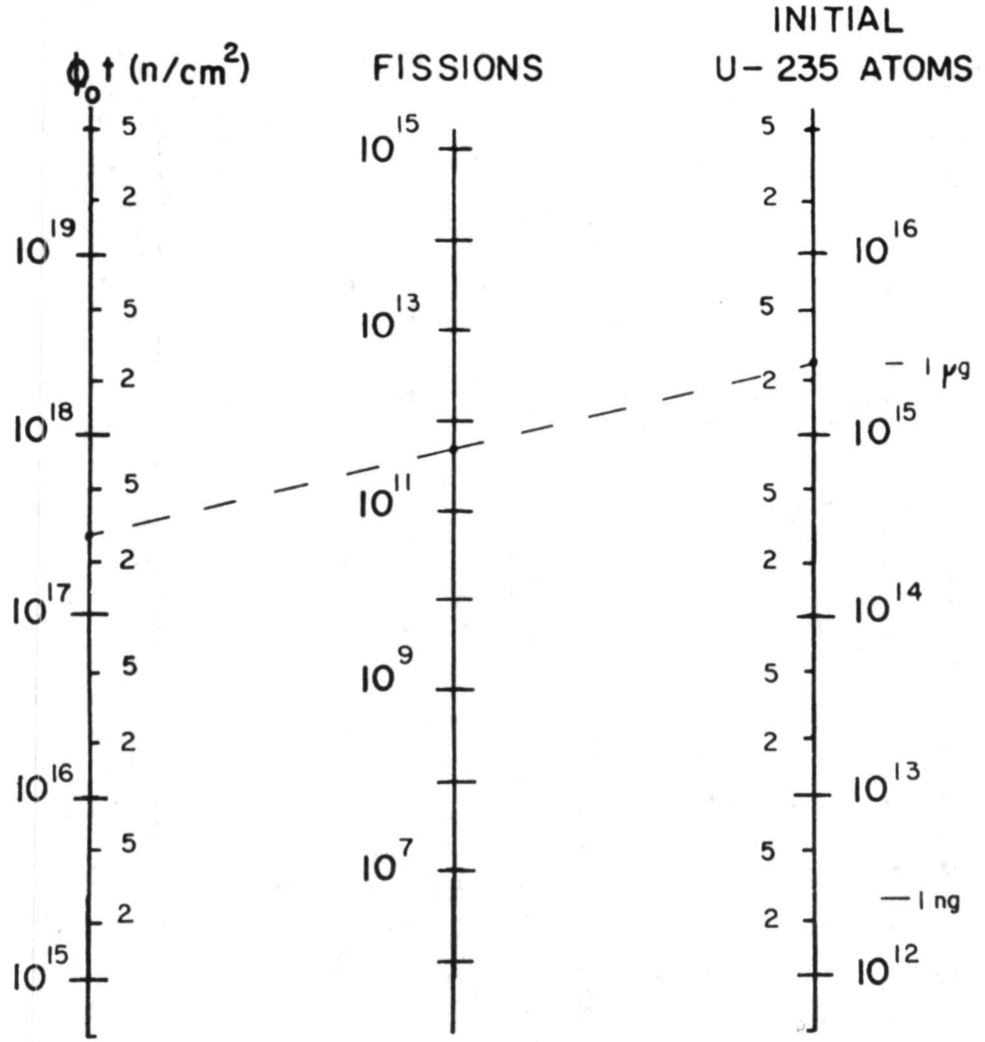

STABLE ISOTOPE PRODUCTION:

$FP_i = Y_i \times$ FISSIONS

Y_i = FISSION YIELD

+(AT 20 ° C. FOR WELL-THERMALIZED SPECTRA)

FIGURE 36 NOMOGRAPH+ OF BURNUP VERSUS INTEGRATED FLUX FOR U-235 a computed Krypton and Xenon production for approximately 4.95 x 10^{11} total fissions, in terms of atoms-isotopic a partial pressure in the mass spectrometer.

Table I

ISOTOPE	F.P. (atoms)	P(torr)
Kr-83	2.574×10^{9}	3.309×10^{-11}
Kr-84	4.801×10^{9}	6.171×10^{-11}
Kr-85	1.386×10^{9}	1.782×10^{-11}
Kr-86	9.553×10^{9}	1.227×10^{-10}
Xe-131	1.440×10^{10}	1.851×10^{-10}
Xe-132	2.144×10^{10}	2.754×10^{-10}
Xe-134	3.920×10^{10}	5.039×10^{-10}
Xe-136	3.197×10^{10}	4.110×10^{-10}

Figures 37 and 38 show the isotopic spectra produced for one sample, promptly after evaporation and after a 7 hour period of operation.

Mr. George Wood of NASA-Langley kindly arranged for the important ionization gauge calibration for this work. Krypton and xenon calibration gases in pyrex bottles were attached to the system through graded glass to metal tubulation. The valves in the gas manifold were bakeable, 1/8 inch diaphragm type.

To pump the system to the ultra high vacuum range, an 80 liter per second sputter ion pump was selected. To suppress hydrocarbon and noble gas backstreaming, a liquid nitrogen trap was added above the pump. This also provides an additional pumping speed for condensable gases and serves to reduce the fringing

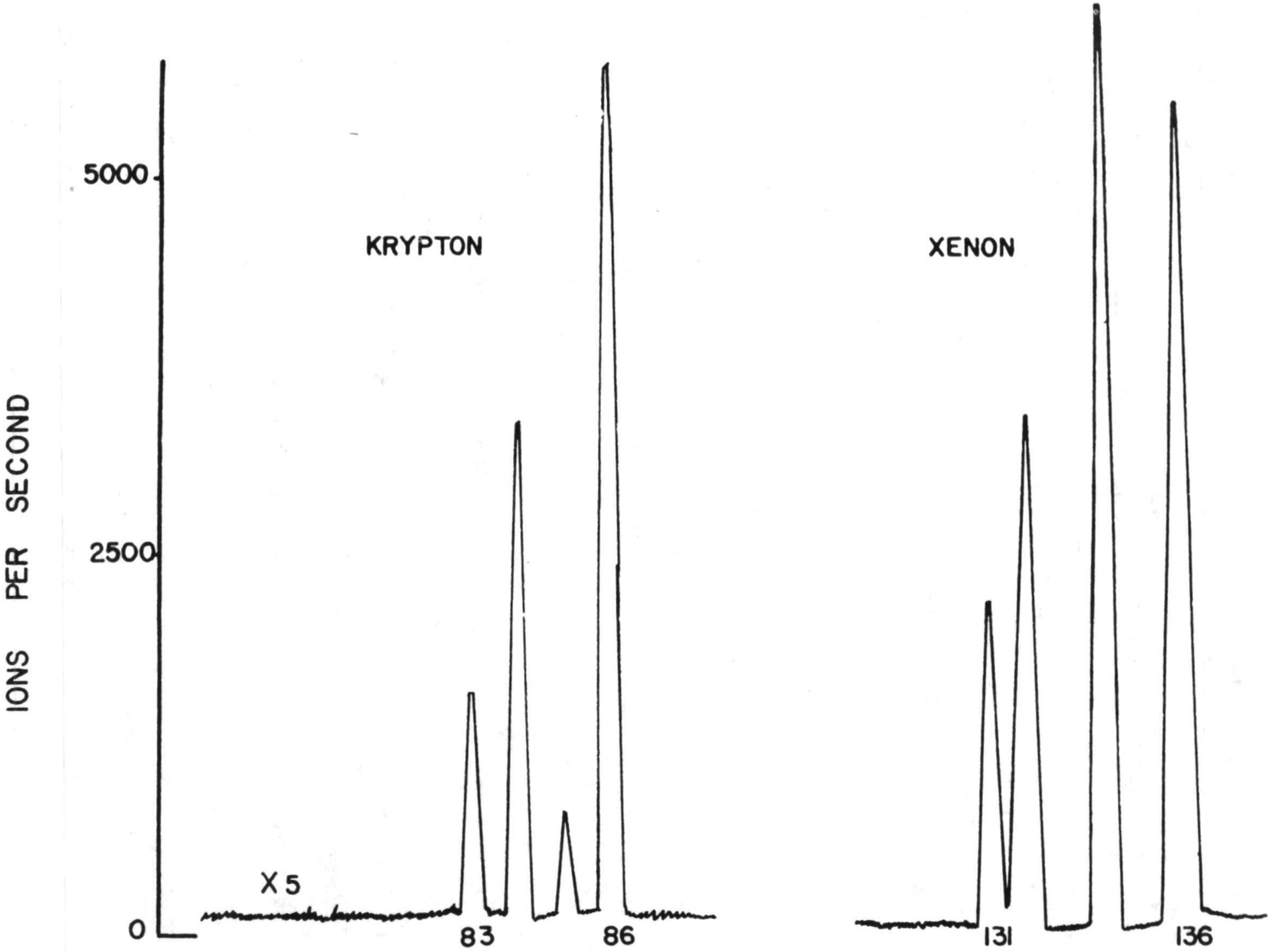

FIGURE 37 SAMPLE RC, XE AND KR FREE FROM INTERFERENCE

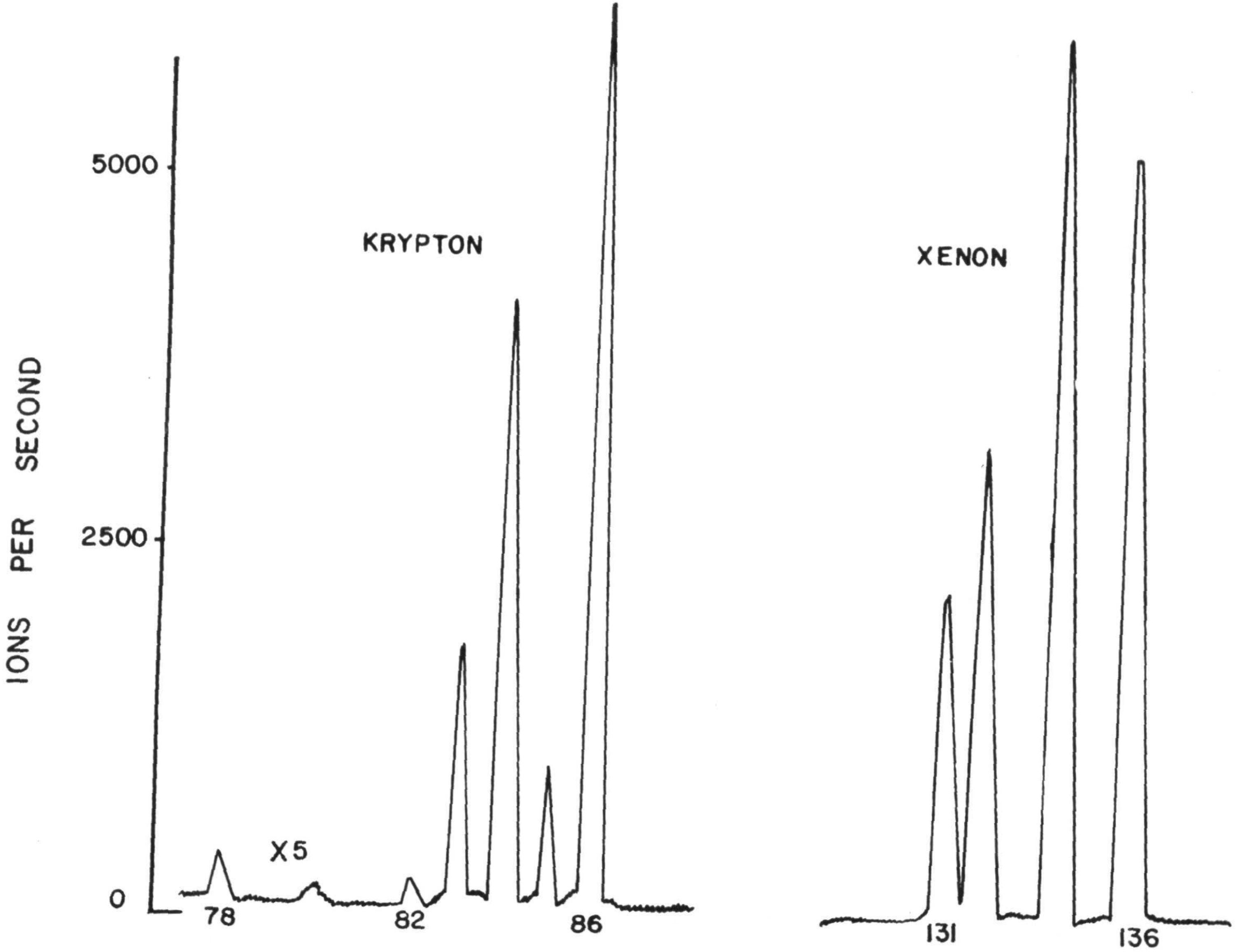

FIGURE 38 SAMPLE RC, XE AND KR AFTER 7 HOURS STATIC OPERATION

field effect from the magnet on the ion pump, by moving the pump further from the source - ion beam region. Figure 39 is a block diagram of the vacuum system, including the calibration gases.

Further details relating to this work are described in the doctoral dissertation of G. Merrill,(25) and the possible implications of this technique are being discussed with NASA-Langley.

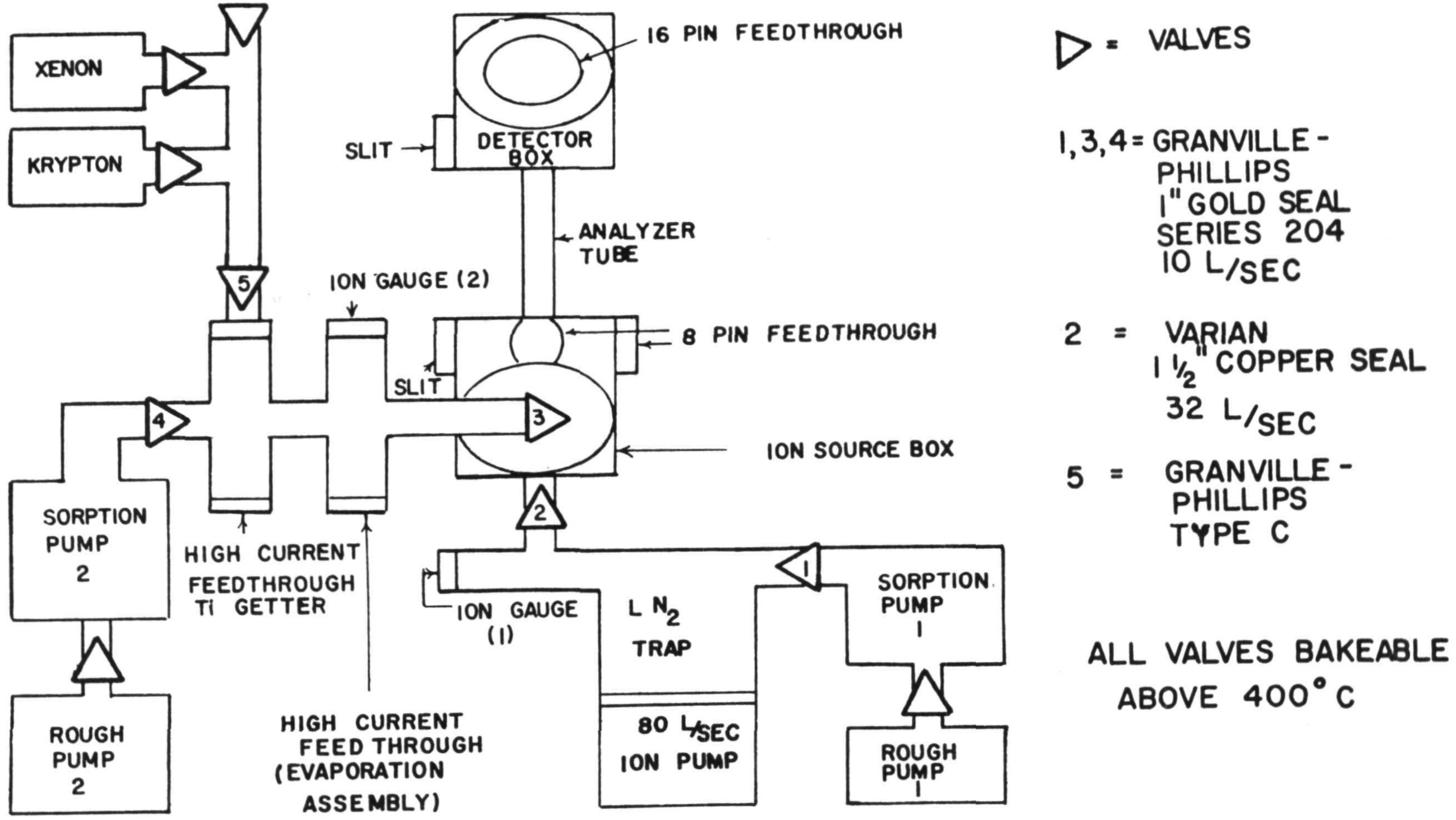

FIGURE 39 BLOCK DIAGRAM OF THE SPECTROMETER VACUUM SYSTEM

VII NEW DEVICES AND TECHNIQUES

A. Coincidence Scheme

A coincidence scheme was devised by the principal investigator (NASA Patent Case No. 7813) in which ions are detected. A special feature of the invention is that single ions can be detected in a radiation environment by causing secondary electrons to be sensed simultaneously in two electron multipliers (or p-n junctions). Figure 40 is a schematic of the basic concept.

B. Microphonic Detector for Neutral Beams

A new concept has been devised for detecting neutral particles by sensing the momentum transfer imparted to a microphone junctioning as a "target: for a mass spectrometer beam. The implications of this concept have been disclosed in a preliminary patent disclosure to G. M. Wood, July 14, 1971, (by F. White and H. Rasekhi). It is anticipated that further work on this project will be undertaken at the NASA-Langley Research Center.

C. New Fabrication Method for Electrostatic Lens

An improved method for constructing large electrostatic lenses was devised by J. Stein which re-

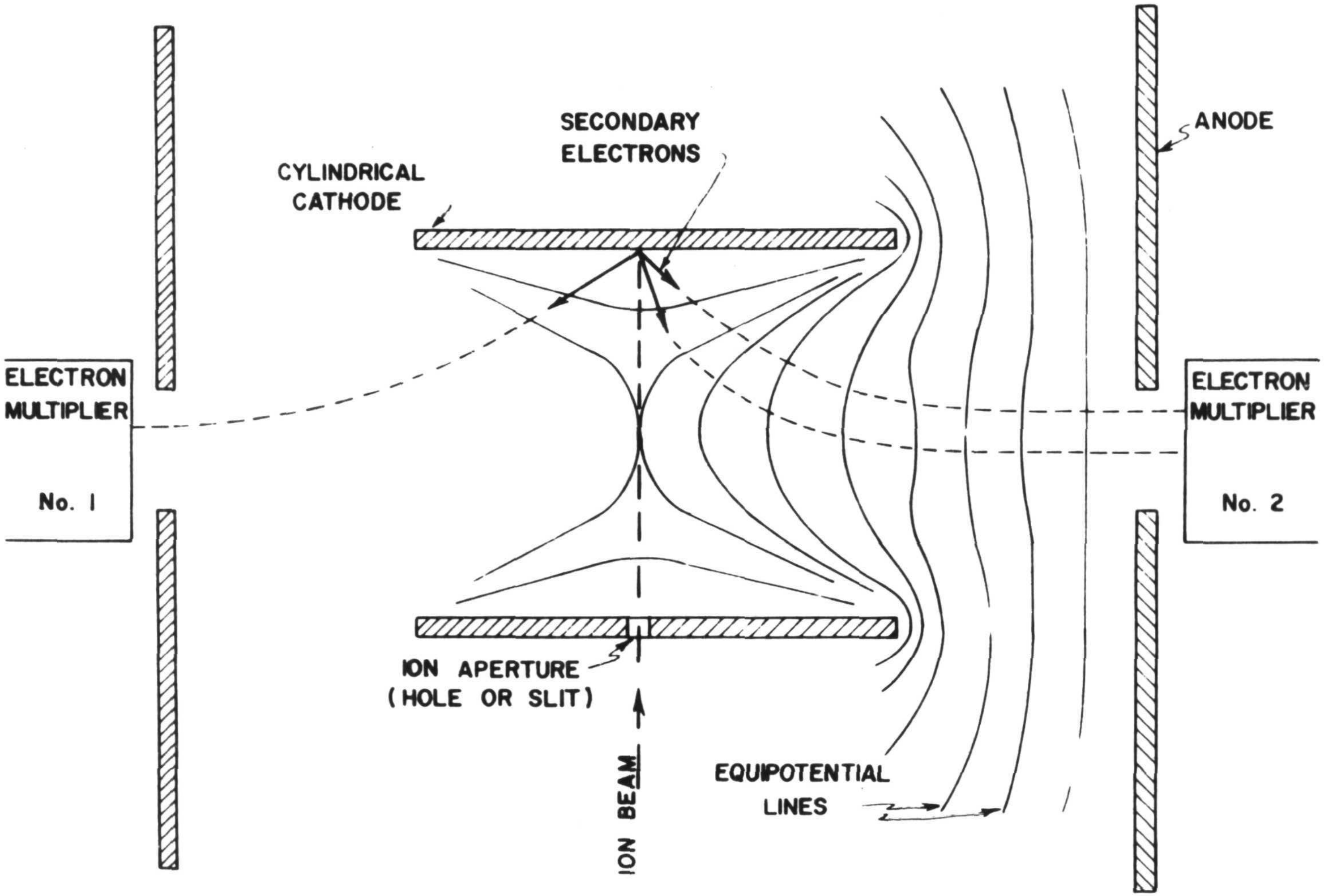

SCHEME FOR DETECTING SINGLE IONS BY COINCIDENT DETECTION OF SECONDARY ELECTRONS

Figure 40

sulted in a publication in the Review of Scientific Instruments. This method was used in the fabrication of the large electrostatic lenses made for the Cascade and Tandem Mass Spectrometer. (see Fig. 41)

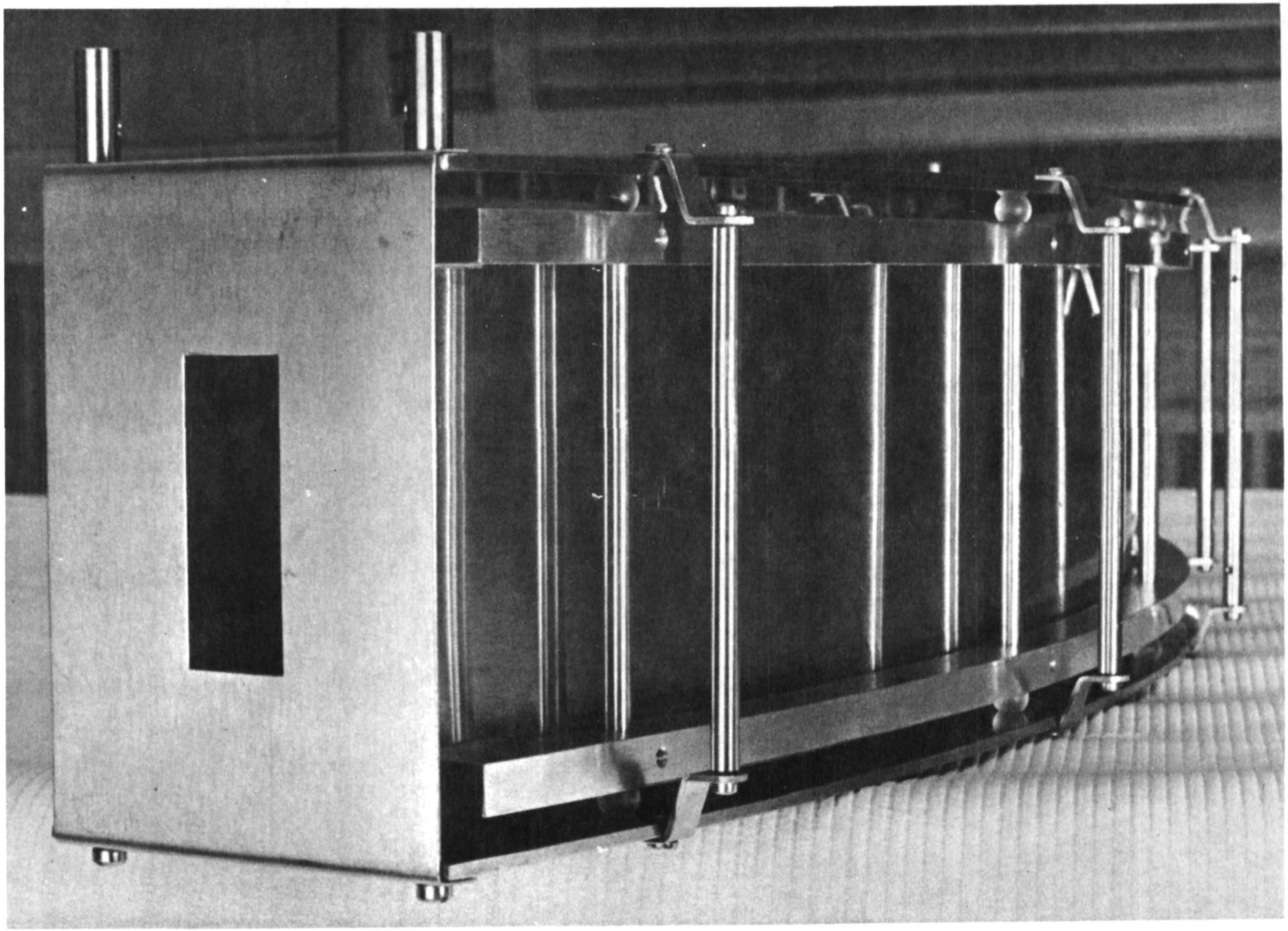

Figure 41

VIII INTERACTION OF IONS WITH SOLIDS

During the period of this grant some effort was expended in connection with a NASA program to explore an interaction phenomena. For this report a summary only of some instrumental aspects of this work is presented. Details are available in the doctoral dissertation of H. Rasekhi(26) and the article(27) titled "A Tandem Ion Analyzer of Large Radius" by Rasekhi and White (Int. Jl. of Mass Spectr. & Ion Physics, 8, 277-291 (1972).

The mass spectrometric facility that was designed and constructed comprised two electrostatic and two magnetic 90° lenses, each with a mean radius of curvature of 122 cm. Both the electrostatic and magnetic components can be operated independently or programmed in tandem, permitting mass and energy resolution of primary ions and secondary species produced in collision processes. A special ion-detector system provides "on line" monitoring of the primary ion beam and counting of secondary ions and neutral atoms at counting rates from 1/sec to 10^7/sec. Special features of the instrument make it useful in investigations of ion energy loss, charge exchange, sputtering, and ion implantation, as well as for isotopic abundance measurements.

The configuration of the apparatus is patterned after the four-stage mass spectrometer reported by White and Forman.(28) The size of the instrument, however, makes this present apparatus closer to the category of isotope separators than to mass spectrometers. The two electromagnets are represented schematically in Fig. 42. Each has a mean radius of curvature of 122 cm and an effective angle of 90°. The actual physical angular sector is approximately 86°; this reduction from 90° is to account for the fringing field which extends substantially beyond the edge of the pole pieces.

Figures 43 and 44 are photographs of the analyzing system. The electrostatic lenses were constructed with a mean radius of curvature of 122 cm, thus matching the radii of the electromagnets. The fabrication of these lenses was patterned after the manner previously described by Stein and White. The interelectrode spacing of the lenses is 10 cm. With this spacing 100 keV ions can be analyzed utilizing a commercially available power supply of 10 kV. A schematic of the electronics is shown in Fig. 45.

Ions are monitored in a pulse counting mode. The output pulses of the electron multipliers are amplified in the amplifier discriminator system

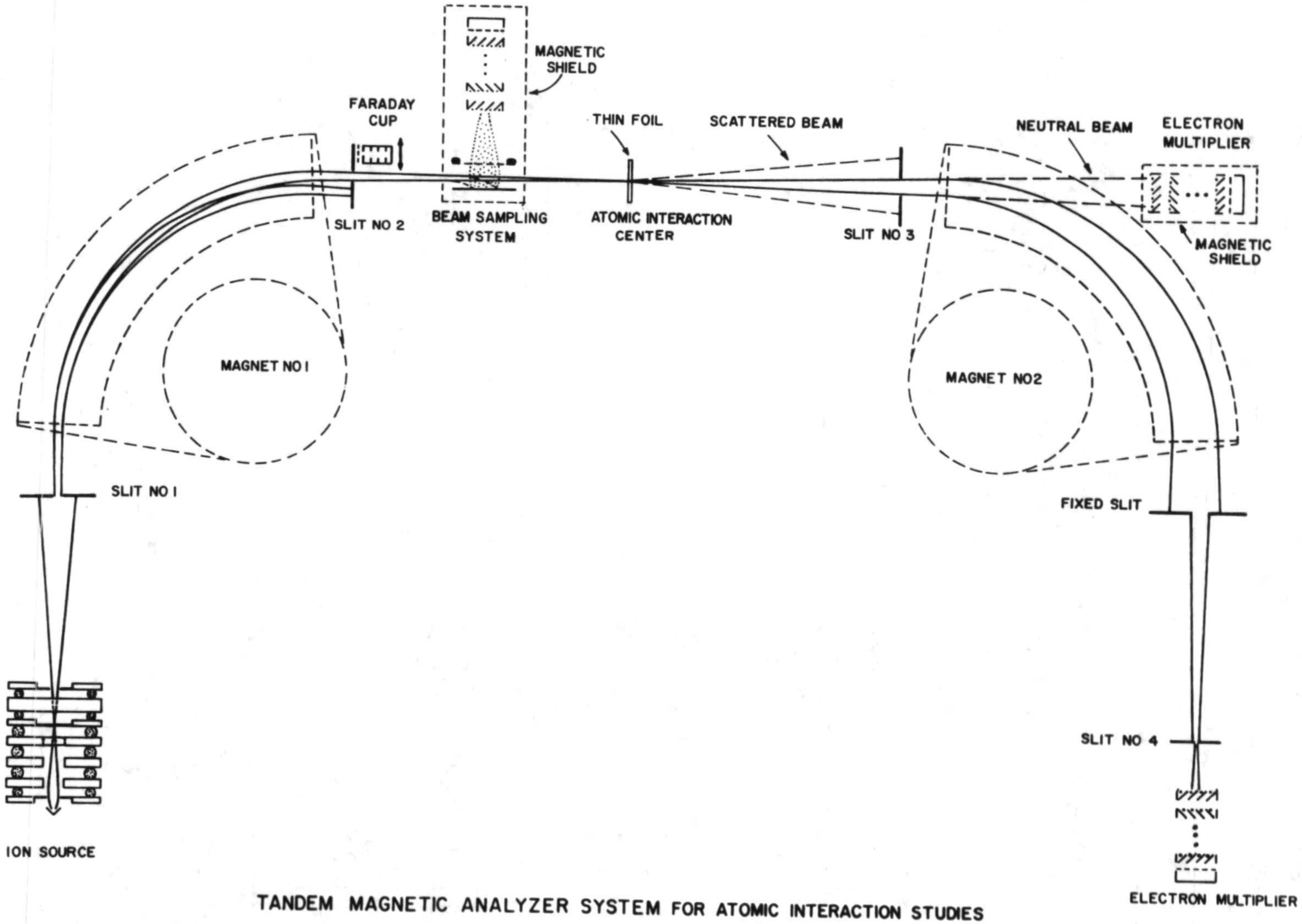

TANDEM MAGNETIC ANALYZER SYSTEM FOR ATOMIC INTERACTION STUDIES

Figure 42

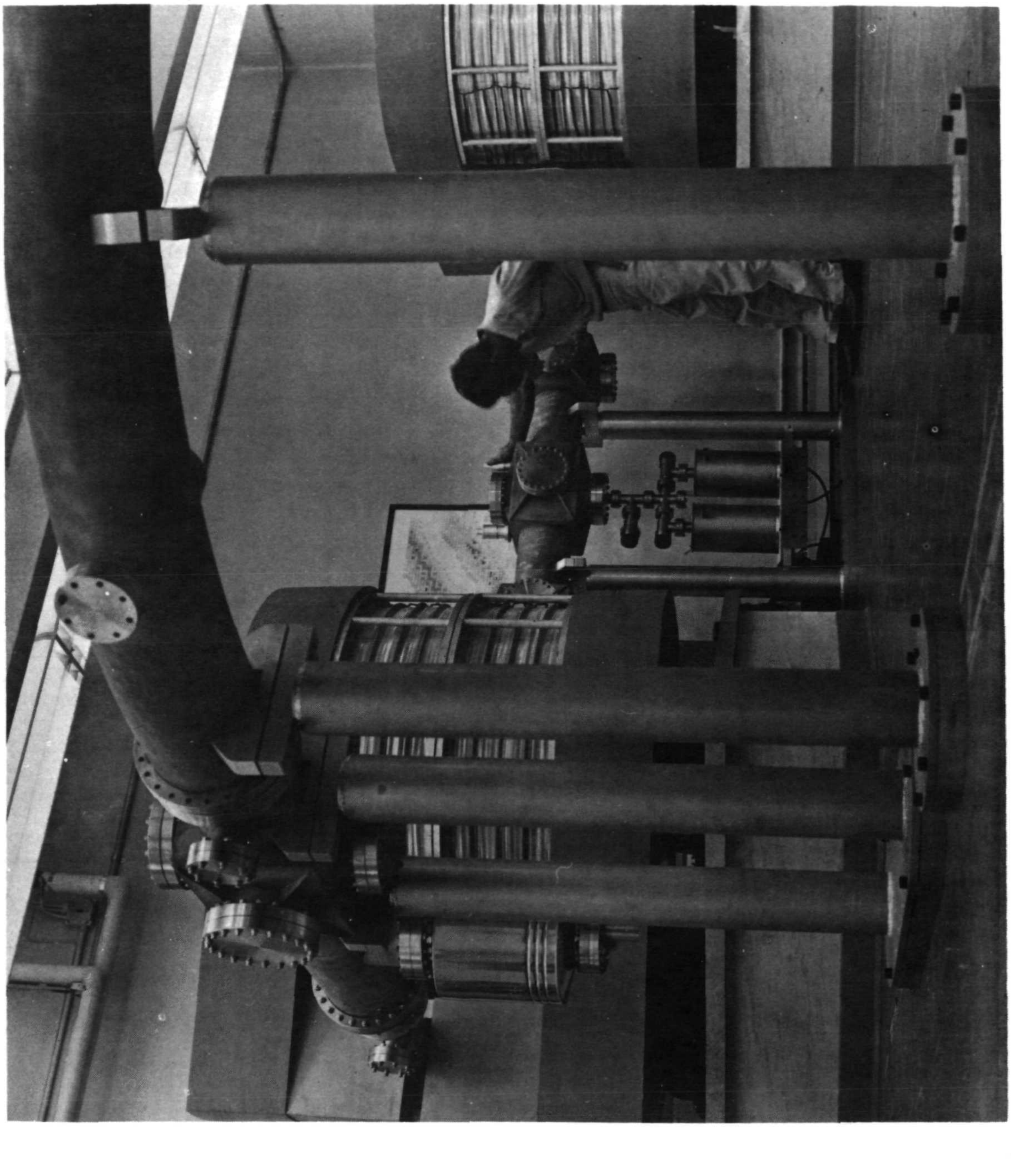

Figure 43

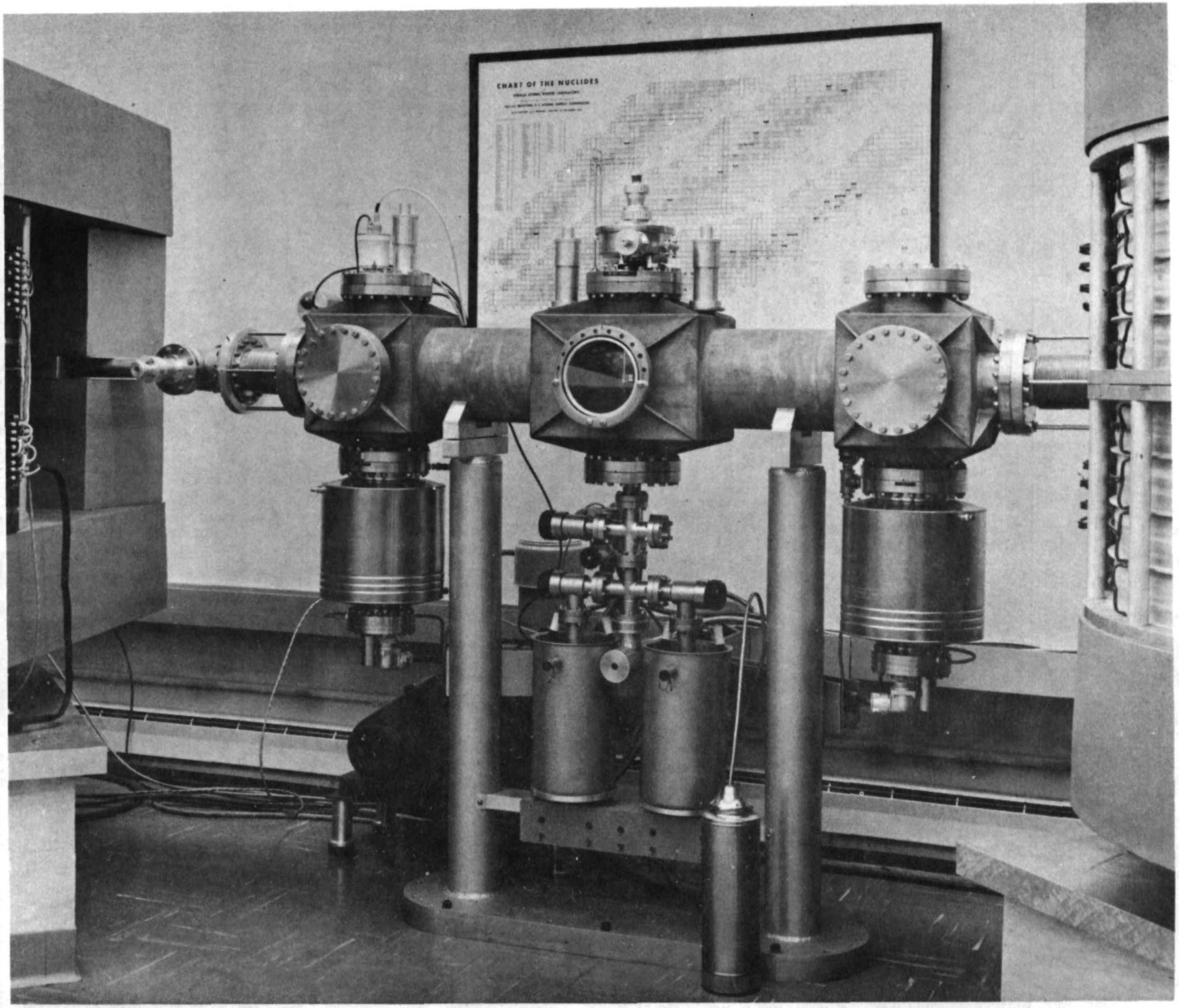

Figure 44

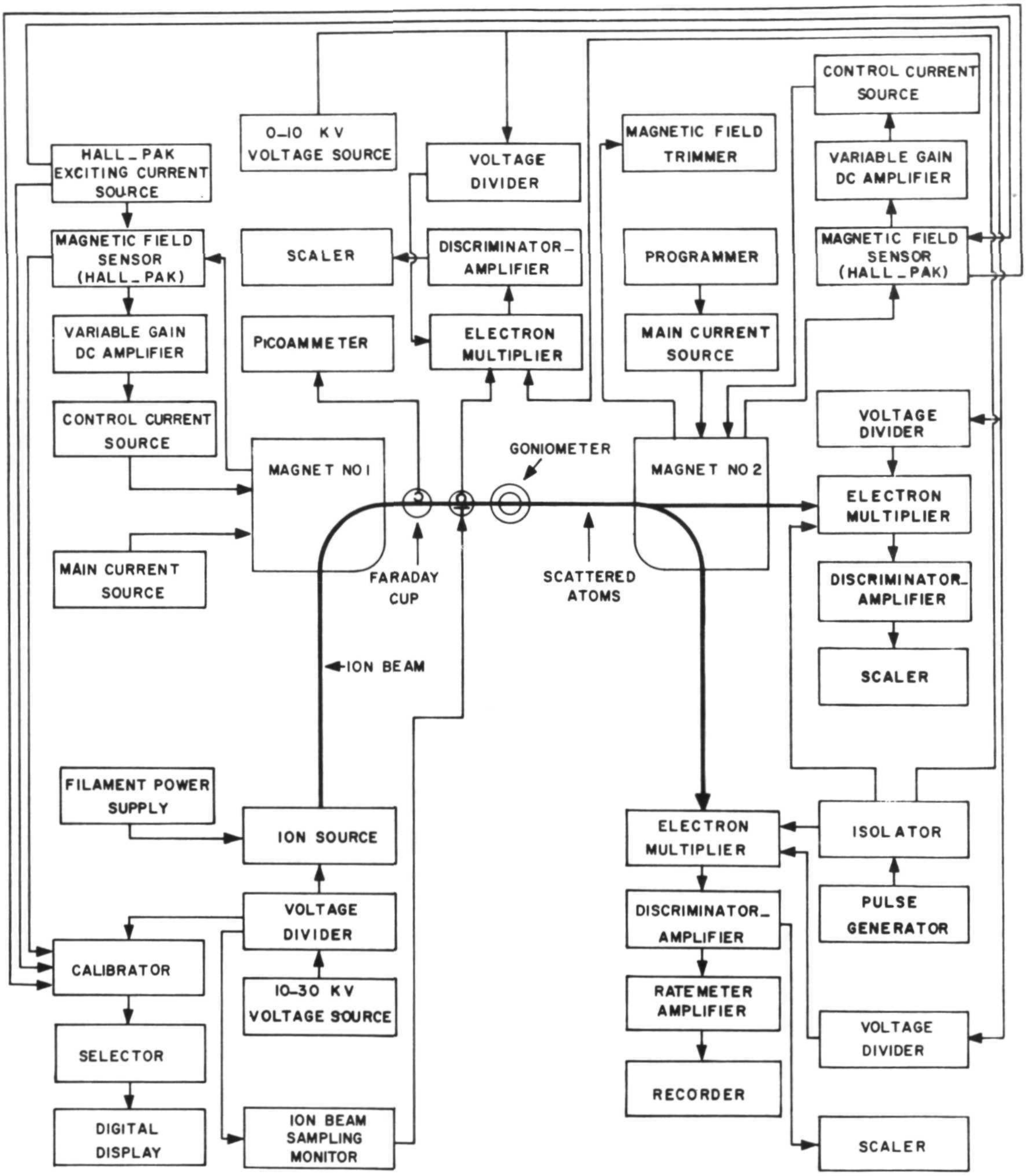

BLOCK DIAGRAM OF THE R.P.I. TANDEM MAGNETIC ION ANALYZER SCHEMATIC

Figure 45

which was originally developed by Sawada. Two major improvements have been made. The first substantially reduced the nonlinearity in the discriminator circuit. Secondly, an addition of one more amplification stage to the preamplifier and sections improved the input-output characteristics of this system. This improved system is now capable of sensing pulses with amplitudes as low as 3 mV and effective duration time of 8 nsec. The discriminator level can be adjusted between 3 mV to 150 mV. Its output is characterized by pulses with about 3.5 V in amplitude and 8 nsec in effective width.

It is appropriate to make special mention of the simultaneous counting capability for measuring neutral atoms and positive ions. As indicated in Fig. 42 ions becoming neutralized in a collision process will proceed through the magnetic field and be intercepted by the neutral beam multiplier. Positive ions undergoing energy degradation in a target (i.e. in a thin-foil) must be focussed onto the final detector by reducing the magnitude of the magnetic field of magnet No. 2 with respect to that of magnet No. 1. There is a distinct advantage in monitoring neutrals and ions simultaneously, inasmuch as the neutral beam monitor can be used to normalize variations in the primary ion beam. Specifically it has been possible to obtain consistent data at counting rates ranging from 10^7 atoms per second to 5 atoms per second.

The data acquisition system is a PDP 8/I computer. Output pulses of the discriminator multipliers of both neutral and ion detectors are fed into individual scalers which are then interfaced to the computer. The computer is then programmed to furnish ratios, perform other desired mathematical operations on the detecting channels, and provide a suitable print-out.

As indicated above the instrument is especially useful for investigating atomic collisions and molecular dissociation phenomena. As a single example, consider the measurement of atomic stopping power of ^{7}Li ions traversing a thin film of nickel. Reference is made to the schematic diagram of Fig. 42 . We should like to determine the energy loss incurred by these singly charged ions in traversing the foil. Lithium ions are generated in the thermal ionization source, accelerated to a kinetic energy of 5-30KeV and focused on a very thin (250 Å) foil. The actual shape of the energy loss curve is important inasmuch as it permits some analysis to be made with respect to the nuclear and the electronic component of atomic stopping, and transport phenomena generally[29,30]. The nuclear component is essentially Rutherford scattering, and the electronic component consists of atomic interactions that give rise to ionization and excited states of atoms within the solid.

The primary analyzing magnet was used to determine the kinetic energy of the lithium ions incident upon the foil. The second analyzer was then programmed (decreased in field strength) so as to focus those ions, which had traversed the foil, onto the electron multiplier. Further, lithium ions which had undergone charge exchange in the foil and emerged as neutral atoms were detected with the neutral beam electron multiplier. A ratio was then taken between the ion and neutral atom counting rates. This procedure eliminated substantially all errors associated with variable ion emission from the source, and it permitted the acquisition of reliable data at very low counting rates. Figure 46 is a single energy loss curve of ^{7}Li ions, obtained for a primary ion energy of 15.1 Kev. Figure 47 shows some of the construction details of the thermal ionization source used to provide the beam of primary lithium ions.

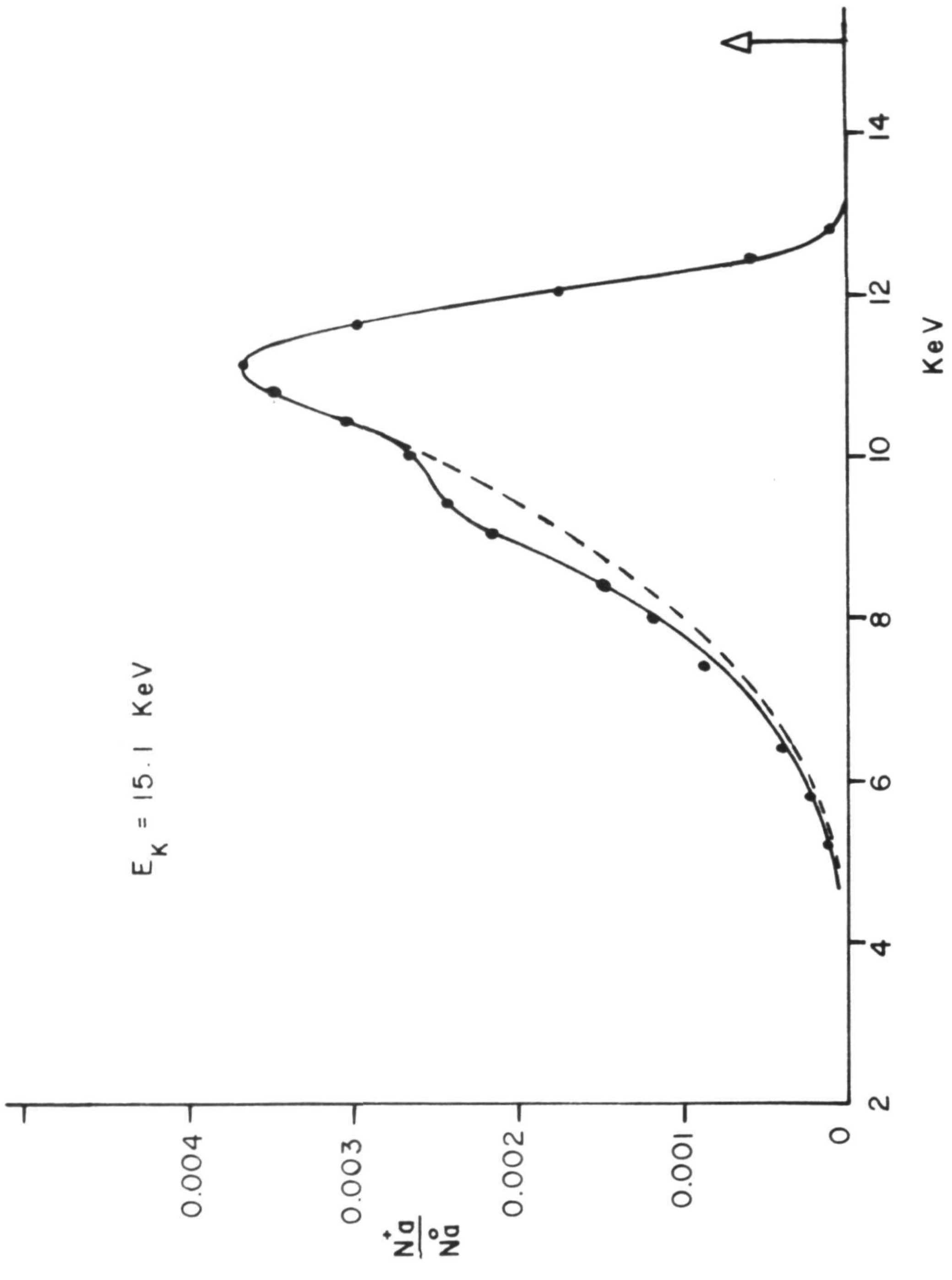

FIG.(5_19)

Figure 46

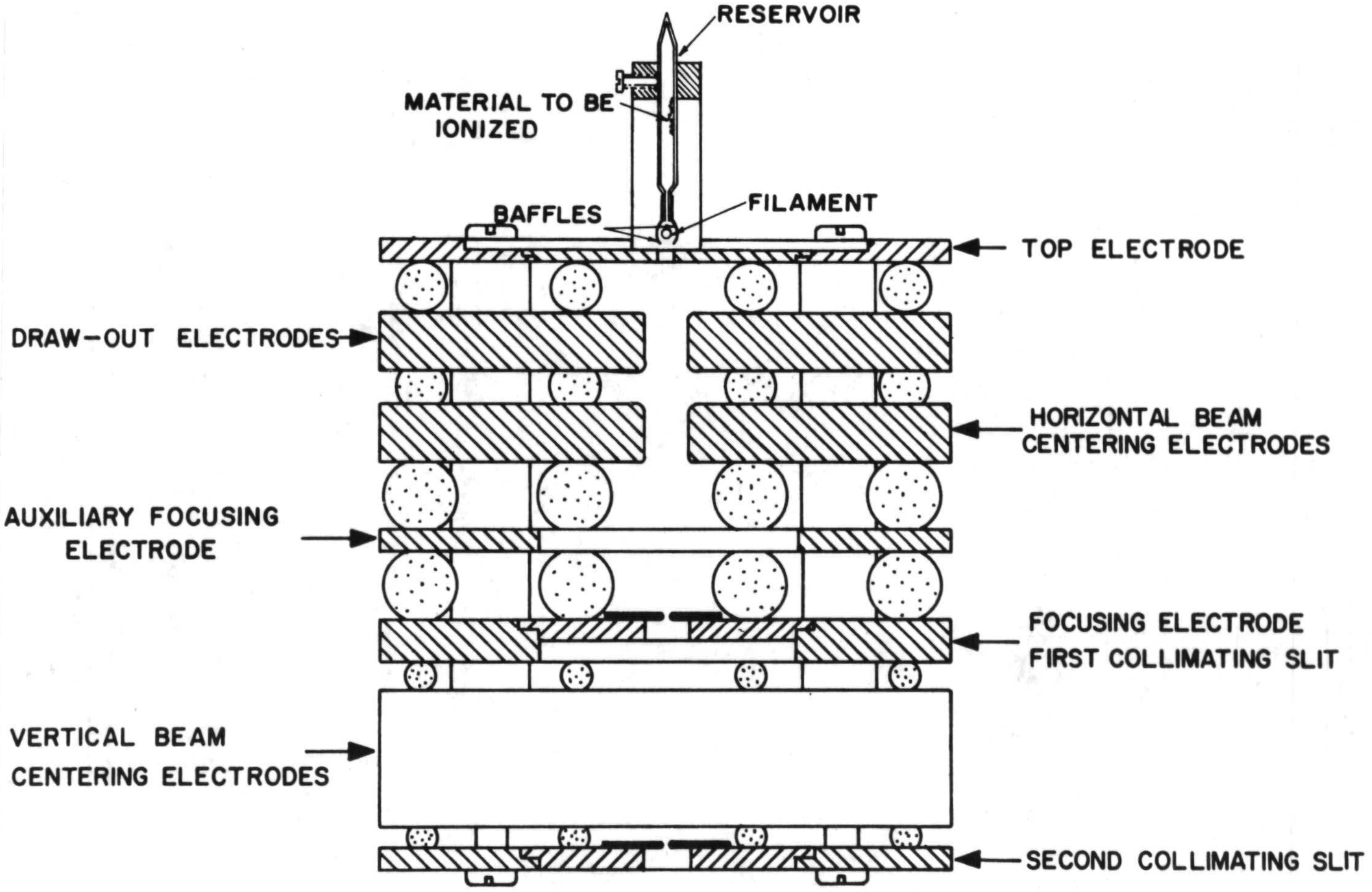

ION SOURCE

Figure 47

IX. CONCLUSION

This terminal report indicates a scope of mass spectrometric effort that encompasses several important areas, e.g., ion optics, the assay of trace metals, detectors, ion production, and the interaction of ions with matter. Actually, all of these topics are interrelated in the sense that each adds to a broader understanding of modern mass spectrometric instrumentation, and collectively they point up the ever increasing potential of spectrometry in science and engineering.

It is to be hoped that this effort will be resumed at a future date, with a somewhat greater degree of coupling than heretofore with the mass spectrometric program of the NASA-Langley Research Center. There are several specific projects that appear to merit an extended research program:

1. The application of inhomogeneous ion optics to an environmental assay field instrument.
2. The development of a microphonic neutral beam detector.
3. Basic studies relating to photon spectra produced by ion impact.
4. An extension of device work on p-n junctions and associated circuitry.

5. A small spectrometer for monitoring particles in the ambient air.
6. The development of a film detector whereby single ions can be registered on an emulsion, in a fashion similar to that for recording fission tracks.
7. Basic studies of channeling at low ion energies, and
8. The utilization of "static" gas mass spectrometry in conjunction with ion implantation techniques.

References

1. Wapstra, A. H., "Recalibration of Alpha Particle Energies," Nuclear Physics, 57 (1964), 48-54.
2. White, F. A. et al., "Absolute Energy Measurement of Alpha Particles from Po^{210},", Physical Review, 109 (1958), 437-442.
3. Alba, F. et al., "Magnetic Spectrograph for the Absolute Measurement of Nuclear Energies," Revista Mexicana de Fisica, 17 (1968), 215-223.
4. Mewherter et al., "Plutonium 244 in Nature," Nature 234 (1971), 132-134.
5. Rasekhi, H., "Ion Transmission Measurements," International Journal of Mass Spectrometry and Ion Physics, 10 (1971).
6. Siegbahn, K. and Svartholm, N., Nature, 234 (1946), 872-874.
7. Dzhelepov, B. S. et al., "Magnetic Alpha-Spectrometer," Bulletin of Academy of Science-USSR, (1959), 780.
8. Holtebekk, T., "A Double Focusing Magnetic Spectrometer for Charged Particles from Nuclear Reactions," Physica Norvegica, 1 (1963), 177-178.
9. Judd, D. L., "The Focusing Properties of a Generalized Magnetic Spectrometer," The Review of Scientific Instruments, 21 (1950), 213, 216.
10. Shull, F. B., and Dennison, D. H., "The Double-Focusing Beta-Ray Spectrometer," The Physical Review, 72 (1947), 581-687.

11. Grove, W. E., Brief Numerical Methods, Prentice-Hall, 1966.

12. F. A. White, J. C. Sheffield and J. Mayer, "P-N Junctions on Mass Spectrometer Detectors," Electronics 34, No. 3, 74 (1961).

13. F. A. White, J. D. Walling, and A. J. Schwabenbauer, "P-N Junction Detectors and Coincidence Methods for Measuring Low Ion Beam Currents," Fifteenth Annual Conf. on Mass Spectr., Denver (1967).

14. F. A. White, Mass Spectrometry in Science and Technology, Wiley, N. Y. (1968), p. 105.

15. Dearnley, G. and Northrup, D. C., Semiconductor Converters for Nuclear Radiations, Wiley, N. Y. 1966, p. 126.

16. Stein, J. D. and White, F. A., "A Multiple Trajectory Ion Beam Analyzer," Int. Jl. of Mass Spectr. and Ion Physics, 5, 205 (1970).

17. Michijima, M., Japanese Jl. of Appl. Phys., 1, 2, p.110 (1962).

18. Dietz, L. A., Rev. of Sci. Instr. 36, p. 1763 (1965)

19. Stein, J. D., Ph.D Thesis, R.P.I. (1970), "An Investigation of Ion Induced Electron Emission from Metallic Oxides."

20. Haussler, B., Zeit, Fur Physik, 179, p. 276 (1964).

21. Baldwin, G. C. and Friedman, S. I., Rev. Sci. Instr., 36, p. 16 (1965).

22. Myers, W. G. and White, F. A., Anal. Chem. 41, 1861-1864 (1969).

23. Chow, T. J. and Johnston, M. S. Science 147, 502 (1965).

24. Ault, W. V., Senechal, R. G., Erlebach, W. E., Envir. Sci and Tech. 4, 4, 305 (1970).

25. Merrill, G. L., Jr., Ph.D. Thesis, R.P.I. (1972), "A Static Mass Spectrometric Assay of Xenon and Krypton Arising from the Low-Level Burnup of U-235."

26. Rasekhi, H., Ph.D. Thesis, R.P.I. (1971), "Atomic Stopping Power of Polycrystalline Nickel for Lithium and Sodium Ions (5-25 Kev).

27. Rasekhi, H. and White, F. A., Int. Jl. Mass Spectr. and Ion Physics, 8, 277-291 (1972).

28. Forman, L. and White, F. A., Rev. Sci. Instr. 38, 355-359 (1967).

29. Firsov, O. B., Soviet Phys. JE TP 5, 1192 (1957)

30. Firsov, O. B., Soviet Phys. JE TP 6, 534 (1958).

☆U.S. GOVERNMENT PRINTING OFFICE: 1973-739-155/69

> *"The aeronautical and space activities of the United States shall be conducted so as to contribute . . . to the expansion of human knowledge of phenomena in the atmosphere and space. The Administration shall provide for the widest practicable and appropriate dissemination of information concerning its activities and the results thereof."*
>
> —NATIONAL AERONAUTICS AND SPACE ACT OF 1958

NASA SCIENTIFIC AND TECHNICAL PUBLICATIONS

TECHNICAL REPORTS: Scientific and technical information considered important, complete, and a lasting contribution to existing knowledge.

TECHNICAL NOTES: Information less broad in scope but nevertheless of importance as a contribution to existing knowledge.

TECHNICAL MEMORANDUMS: Information receiving limited distribution because of preliminary data, security classification, or other reasons. Also includes conference proceedings with either limited or unlimited distribution.

CONTRACTOR REPORTS: Scientific and technical information generated under a NASA contract or grant and considered an important contribution to existing knowledge.

TECHNICAL TRANSLATIONS: Information published in a foreign language considered to merit NASA distribution in English.

SPECIAL PUBLICATIONS: Information derived from or of value to NASA activities. Publications include final reports of major projects, monographs, data compilations, handbooks, sourcebooks, and special bibliographies.

TECHNOLOGY UTILIZATION PUBLICATIONS: Information on technology used by NASA that may be of particular interest in commercial and other non-aerospace applications. Publications include Tech Briefs, Technology Utilization Reports and Technology Surveys.

Details on the availability of these publications may be obtained from:

SCIENTIFIC AND TECHNICAL INFORMATION OFFICE
NATIONAL AERONAUTICS AND SPACE ADMINISTRATION
Washington, D.C. 20546